Detector and System Developments for LHC Detector Upgrades

Beatrice Mandelli

January 29, 2015

Thesis submitted for the degree of Philosophiae Doctor
Department of Physics
Faculty of Mathematics and Natural Sciences
University of Oslo

Series of dissertations submitted to the
Faculty of Mathematics and Natural Sciences, University of Oslo
No. 1623

ISSN 1501-7710

Cover: Hanne Baadsgaard Utigard.
Printed in Norway: AIT Oslo AS.

Produced in co-operation with Akademika Publishing.
The thesis is produced by Akademika Publishing merely in connection with the thesis defence. Kindly direct all inquiries regarding the thesis to the copyright holder or the unit which grants the doctorate.

Contents

Introduction

The Large Hadron Collider (LHC) at the European Organization for Nuclear Research (CERN) has established a new Particle Physics program covering high precision measurements of the Standard Model as well as searches of new physics (Chapter 1). The objectives of this program demand thorough consolidation and upgrades of both the accelerator and the detectors systems. Chapter 2 presents the different detector upgrade strategies adopted by the four main LHC experiments.

This PhD thesis combines detailed gas studies of LHC gas detector systems with detector system development, construction and characterization of the Insertable B-layer (IBL), the ATLAS Pixel upgrade during LS1.

Within the LHC tracker upgrade programs, the ATLAS IBL is the first major upgrade of a silicon-pixel detector. IBL improves the overall Pixel Detector performance, which is expected to degrade with the increase of luminosity. Chapter 3 gives an overview of the IBL detector system and some of the new technologies that have been developed to fulfill the demanding requirements. This thesis work focuses on the IBL production phase, when it was necessary to define and elaborate a rigorous Quality Assurance (QA) protocol for testing and qualifying all detector components before the final integration and assembly stages. The IBL is the innermost sensing layer of the ATLAS experiment, detector efficiency and reliability are of crucial importance. The work here presented is devoted to the QA for the IBL staves. The staves, each holding 20 pixel modules, are the basic element for the assembly of the IBL detector. A total of 18 staves have been qualified in terms of signal performance, noise and overall functionality. Considering the amount of work, the importance of the task and the tight schedule, the activity has been accomplished by an expert team where each member was responsible of testing some of the staves. Chapter 4 is entirely dedicated to QA and the corresponding stave qualification as well as studies related to detector components reliability in the ATLAS experimental conditions. For the latter, a systematic study of wire bonds operated in ATLAS-like magnetic field has been conducted.

The gas detector systems installed at LHC, and those being considered for their upgrade, will be exposed to an unprecedented high radiation environment. Systematic studies are needed to identify the key processes and gas parameters that affect their operation, and ultimately to provide guidelines for the operation of gas systems and detectors at very high rates. Foreseen upgrades of muon systems concern their read-out systems and the addition of new muon stations. It is therefore of prime importance to maintain the existing detectors in good operating conditions. In this context, the gas systems play a crucial role as they provide the gas mixture, which can affect the detector operation in many ways. Chapter 5 reviews the different solutions adopted for gas systems and analyzers used to monitor the gas mixture. Starting from real issues

occurred at the LHC experiments, the present thesis describes the limits of the standard analysis techniques and proposes new applications of a complementary gas monitoring tool based on a single wire proportional chamber. Chapter 6 explores and proposes solutions to the key problems that large systems will phase in the near future. Cost arguments and the need of reducing the greenhouse emissions will force the use of gas recirculation systems, and some of the currently used greenhouse gases will be substituted with new environmentally friendly components. These two aspects are important for the current systems but also have to be validated for newly developed detector technologies. Studies of operating a GEM detector in a closed-loop is used as example of a new detector technology that is planned for future upgrades of the LHC experiments. Gas replacement is addressed considering the specific case of the Freon R134a for RPC detectors.

Chapter 1

High Energy Physics at LHC

The Standard Model (SM) theory has been successfully tested to an exceptional level of accuracy by several experiments in the last decades. Nevertheless the SM presents some critical shortcomings as the unification of all forces or the hierarchy problem of the Fermi scale. The experiments taking place at CERN have been conceived to investigate the unanswered questions in the field of high energy physics. A new Particle Physics program has started with the Large Hadron Collider (LHC) giving, as a main result, the discovery of the Higgs boson. This achievement is only the beginning of an intense LHC Physics program to better understand the SM and the physics beyond it.

1.1 Overview of Physics at the Large Hadron Collider

The SM combines special relativity and quantum mechanics providing a valid and detailed framework for the description of Electromagnetic and Weak forces. It is a gauge theory based on the symmetry group [1]:

$$G = SU_c\,(3) \otimes SU_L^{Weak}\,(2) \otimes U_Y^{Weak}\,(1) \tag{1.1}$$

where $SU_c\,(3)$ is associated to the color quantum, $SU_L^{Weak}\,(2)$ to the weak isospin and $U_Y^{Weak}\,(1)$ to the hypercharge. In the SM, the fundamental constituents of matter are spin-1/2 particles, called fermions. The fermions are divided into two groups, named quarks and leptons, which can be divided into three families. Each family consists of weak isospin doublets in additions to one or two weak isospin singlets:

$$\begin{array}{lccc} lepton & \begin{pmatrix} e \\ \nu_e \end{pmatrix}_L & \begin{pmatrix} \mu \\ \nu_\mu \end{pmatrix}_L & \begin{pmatrix} \tau \\ \nu_\tau \end{pmatrix}_L \\ & (e)_R & (\mu)_R & (\tau)_R \\ quarks & \begin{pmatrix} u \\ d \end{pmatrix}_L & \begin{pmatrix} c \\ s \end{pmatrix}_L & \begin{pmatrix} b \\ t \end{pmatrix}_L \\ & (u)_R,\ (d)_R & (c)_R,\ (s)_R & (b)_R,\ (t)_R \end{array} \tag{1.2}$$

The stable matter observed in the universe is made of the first generation of fermions. For each fermion, a corresponding anti-particle exists with exactly same coupling but with opposite quantum numbers. The fermions interact among them through the exchange of spin-1 particles, called gauge bosons, which arise from the invariance of the theory under gauge symmetries.

Four fundamental interactions are known: electromagnetic, weak, strong and gravitational. Each different interaction is shaped by an independent gauge group and is mediated by different bosons. The electromagnetic interaction, described by the Quantum Electro-Dynamics (QED) theory, is mediated by the massless boson called photon. The weak interactions are mediated by the massive $W^{\pm}$ and Z^0 gauge bosons while the strong interactions are carried by gluons. However in the ElectroWeak (EW) theory all particles are massless. In 1964 a mechanism, called Higgs mechanism, was introduced to generate the masses of bosons and fermions through the interaction with a scalar background field in the SM. As the $W^{\pm}$ and Z^0 bosons are massive and the photon is massless, the Higgs-mechanism must break the EW symmetry. This requires the existence of an additional massive boson with spin 0, the so-called Higgs boson, whose mass is an open parameter of the theory.

Even if nowadays the SM can be considered to give a self-consistent picture of the fundamental building blocks of matter and their interactions, it cannot be treated as the ultimate theory since several questions, both theoretical and phenomenological, do not find an explanation, as for example the CP violation theory, the Great Unification Theory and the dark matter existence as well as the unknown values of several SM parameters. Many efforts have been performed to accommodate these and other problems in a new theory that must contain the SM as a lower energy limit. Several theories have been proposed but they must be verified experimentally and nowadays there are not considerable confirmations. An example of an extension of the SM theory is the Super Symmetry (SUSY) theory, which proposes a symmetry between fermions and bosons linking the basic particles with the force-carrying particles. SUSY theory potentially offers an elegant solution to the hierarchy problem, providing an excellent dark matter candidate and unification of gauge couplings.

1.2 Physics highlights until first LHC long shutdown

The LHC [2] is a two rings superconducting hadron accelerator and collider installed in the existing 26.7 km Large Electron-Positron (LEP) tunnel about 100 m underground. It has been designed to provide enough statistics for its rich physics program, covering both high precision measurements of the SM as well as search of new physics. To achieve its goals, LHC nominally provides a center of mass energy of 14 TeV for proton-proton collisions created by 2808 bunches, consisting of 1.15×10^{11} protons each, with 25 ns bunch spacing at the design luminosity of $10^{34}\,\mathrm{cm}^{-2}\,\mathrm{s}^{-1}$. The LHC can supply also PbPb and Pbp collisions that reach a center of mass energy of 2.76 TeV and 5.02 TeV, respectively. Physics is exploited by four experiments located in four different LHC interaction points: ATLAS [3], CMS [4], ALICE [5] and LHCb [6]. The ATLAS and CMS experiments are general-purpose detectors, capable of exploring all aspects of the LHC program, from heavy-ion collisions and forward physics to Higgs boson physics and direct searches for new particles. The ALICE experiment is dedicated to heavy-ion physics while LHCb is designed to maximize the LHC potential in beauty and

charm physics.

In 2012, the LHC has been operated at 8 TeV centre of mass energy, compared to 7 TeV in 2010-2011. Several milestones have been achieved before the first technical long shutdown (started in 2012), mostly in terms of accelerator performance and physics analysis. At the end of the first three-year LHC running period (2010-2013), the LHC delivered about 20.8 fb^{-1}, reaching a peak luminosity of 7.7×10^{33} cm^{-2} s^{-1} for ATLAS and CMS experiments and smaller amounts to LHCb and ALICE experiments.

The major achievement of the ATLAS and CMS experiments is without any doubts the observation of a new boson with a mass of 126 GeV and Higgs-like properties in terms of signal strength (July 2012) [7], [8]. The Higgs boson channels with the strongest sensitivity at the LHC are the gluon-fusion and the vector-boson fusion channels, whereas the most promising decay processes are the di-photon, the ZZ to four leptons and the leptonic WW channels. Both experiments obtained the most significant deviations from the background-only hypotheses in the ZZ and di-photon channels, as it can be seen from the excess found in the invariant mass distributions of two photons (Figure 1.1(a)), as well as from the distribution of the local p-value as a function of the hypothetical Higgs mass (Figure 1.1(b)). The Higgs boson mass has

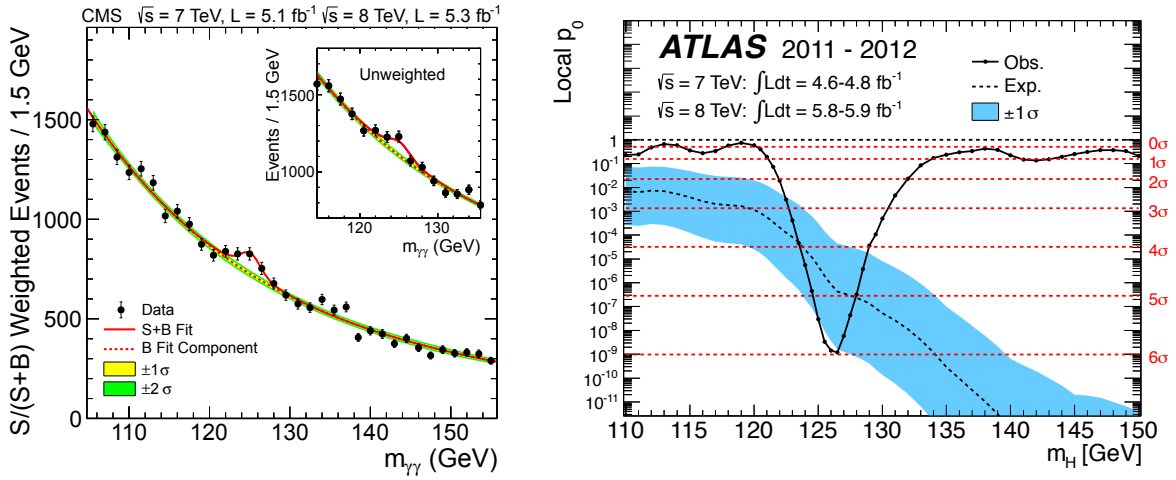

(a) (b)

Figure 1.1: (a) Invariant mass distribution in the di-photon channel of the CMS Higgs search [8]. (b) Local p-values in the ATLAS Higgs searches. The dashed curve shows the expected local p0 distribution for a Higgs boson at the corresponding mass while the horizontal dashed lines indicate the p-values corresponding to significances of 1 to 6 sigma [7].

been measured to a remarkable precision: 0.43% in ATLAS and 0.34% in CMS. Similarly, the production cross section relative to its SM prediction has been measured to about 15% precision by each experiment. The data strongly prefer the spin-parity for a new particle to be consistent with that of the vacuum ($J^{PC} = 0^{++}$), which is also the value predicted for the SM Higgs boson.

Besides the discovery of the Higgs Boson, the searches for physics Beyond-Standard Model (BSM) are going on at LHC even if they have revealed nothing new so far. These searches can be roughly divided into two large sectors: searches on SUSY particles and searches for other particles and interactions beyond the SM [9]. Generic searches for squarks and gluinos traditionally cast in a constrained version of the minimal supersymmetric standard model (MSSM)

however, up to now, results are not encouraging and different ways of casting searches for SUSY are going on, as via the simplified model space (SMS) [10]. Several attempts to investigate new physics are so numerous by now that a comprehensive summary is basically impossible.

Another important topic in the LHC researches is the flavor physics, which is lead by the dedicated LHCb experiment. Several flavor physics highlights have been accomplished during LHC Run 1 as, for example, the observation of new heavy beauty bound states ($\chi_b(3P)\,b\bar{b}$ meson and Ξ_b^* baryon), the first evidence for the $B_s^0 \to \mu\mu$ decay or the first observation of direct CP violation in B_s^0 decays [9], [11]. At the same time, very successful PbPb (2010, 2011) and pPb (2013) runs brought a wealth of data and allowed ALICE, ATLAS, and CMS to produce unprecedented and very exciting new results in heavy-ion physics as, for example, detailed studies of jet quenching in PbPb collisions and dijet production in pPb collisions and a number of other unique PbPb measurements (W and Z production, jet-photon correlations, etc) [12], [13].

1.3 Future Physics program at high luminosity

The current LHC program foresees a delivery of proton-proton collisions with an integrated luminosity of 3000 fb^{-1} at a center of mass energy of 14 TeV by around 2030 and PbPb collisions with an integrated luminosity of at least 10 nb^{-1} at $\sqrt{s_{NN}}$=5.5 TeV. Relative to current LHC plans, these numbers correspond to a tenfold increase in statistics. These much larger energies and integrated luminosities will open a huge unexplored phase for the search of new physics as well as amounts of data for precision studies of the Higgs boson. Four major experimental lines can be delineated [14]:

- precision tests of the role of the observed Higgs boson in the SM, including searches for additional Higgs bosons
- direct searches for other BSM Physics
- precision tests of the SM in Heavy Flavour Physics and Rare Decays
- heavy Ion Collisions and the Physics of the Quark-Gluon Plasma

A major focus of the physics program is surely dedicated to the Higgs boson since precision measurements of its properties will be possible thanks to the higher luminosity. In particular the primary goals are the measurements of its couplings to fermions and bosons, its rare decays and its self-couplings. The knowledge of these parameters will allow a better understanding of the SM [15], [16] and the possibility to prove BSM Physics models [17]. As an example, the measurement of the Higgs boson self-coupling and subsequent reconstruction of the Higgs potential is a fundamental test of the Higgs mechanism described in the SM. Thanks to the higher luminosity of the next years, also rare and invisible Higgs boson decay channels will be studied giving a deep knowledge on the Higgs coupling couplings to elementary fermions and bosons. The relative uncertainties on the total signal strength for some Higgs decay modes for accumulated integrated luminosities of 300 and 3000 fb^{-1} are reported in Figure 1.2(a).

The future CERN Physics program is not only focused on the Higgs boson and its properties as it has been demonstrated by the fact that LHC has already probed significant new regions of

BSM parameter space. Figure 1.2(b) shows an estimate of the scales that can be probed at $\sqrt{s}$=14 TeV with 300 and 3000 fb^{-1} as a function of the mass scales being probed in today's searches [14]: the center-of-mass energies that can be studied increase by about 1 TeV thanks to an extra factor of 10 in integrated luminosity. The relative gains are most significant for new physics objects where current searches exclude only low system masses. A significant problem arises with the low mass of the Higgs boson and its related hierarchy problem, which can be studied only at high energy as well as SUSY and BSM theory. BSM Physics is an open scenario with several theories being explored. The future LHC period at higher luminosity will be essential in this search and in case new physics will be found, extended run periods will be needed to measure the properties of new particles.

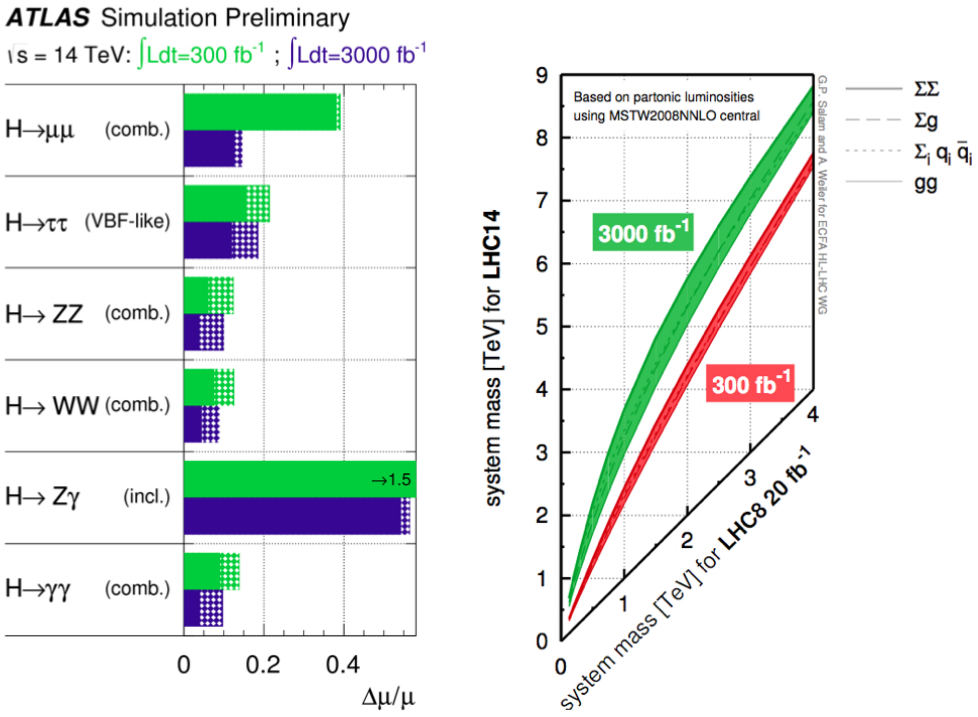

(a) (b)

Figure 1.2: (a) Relative uncertainty on the total signal strength for all Higgs final states in the different experimental categories used in the combination, assuming a SM Higgs Boson with a mass of 125 GeV. The hashed areas indicate the increase of the estimated error due to current theory systematic uncertainties [15]. (b) Estimate of the system mass that can be probed in BSM searches at the 14 TeV LHC with 300 or 3000 fb^{-1}, as a function of the system mass probed so far for a given search with 8 TeV collisions and 20fb^{-1} [14].

In parallel to Higgs studies and new physics searches, more precise SM measurements and calculations as well as flavour and heavy ions physics will be of fundamental importances [18]. For example, sensitivity studies demonstrate that LHCb will be the leading experiment for a wide range of important observables concerning rare decays and CP violation in charm and beauty hadrons while heavy-ion physics will allow the studies of heavy-flavour particles, quarkonium states, jets and their correlation with other probes, etc.

The future physics program implies upgrades on detectors, their electronics and DAQ as well as on trigger to maintain or improve the performance. The requirements are driven by the

basic need to remain operational despite the increasing accumulated radiation dose and to deal with higher occupancies from pile-up as well as by the need to trigger on and to measure the physics channels of interest. The accomplishment of these conditions can be reached only with a well-planned and systematic upgrade of the LHC detectors that has already start during the LS1 and it will continue for the next 10 years.

Chapter 2

The Detector Upgrade Program for the LHC Experiments

In 2006, the European Strategy for Particle Physics was agreed for the decades to come and an updated Strategy was adopted by the CERN Council in May 2013. The program sets the priorities for European Particle Physics taking into account the Higgs boson discovery at LHC in 2012 and the global energy frontier research landscape. It contains a key message towards the accomplishment of the High Luminosity LHC program:

> *Europe's top priority should be the exploitation of the full potential of the LHC, including the high-luminosity upgrade of the machine and detectors with a view to collecting ten times more data than in the initial design, by around 2030. This upgrade program will also provide further exciting opportunities for the study of flavour physics and the quark-gluon plasma.*

An intense LHC upgrade program has already started at CERN for both LHC accelerators chain and experiments. The extreme LHC performance foreseen for the next decades needs intense consolidation and upgrades of the detectors as well as simulation studies to understand their optimization as a function of the physics performance and goals.

2.1 The LHC Upgrade Phases

In 2012 with the final LHC running conditions, an integrated luminosity of about $30\,\text{fb}^{-1}$ has been accumulated with a peak luminosity of $7.7\times10^{33}\,\text{cm}^{-2}\,\text{s}^{-1}$. Data collisions have been recorded both at $\sqrt{s}$ = 7 and 8 TeV leading to the major discovery of a 126 GeV Higgs boson [7], [8].

The LHC has been upgraded to the design energy of 13 to 14 TeV with an expected bunch spacing of 25 ns and instantaneous luminosity of $10^{34}\,\text{cm}^{-2}\,\text{s}^{-1}$ during the first LHC Long Shutdown (LS1, 2013-2014). The new parameters will allow to deliver $\geq$50 fb^{-1} before the following shutdown. The current planning of upgrades foresees two other long shutdowns (LS2 and LS3) as it is visible in Figure 2.1, which shows a time line of the LHC upgrade phases.

During LS2 the injector chain and the LHC will be both improved with the integration of Linac4 into the injector complex [19]. Potentially a further increased luminosity of about

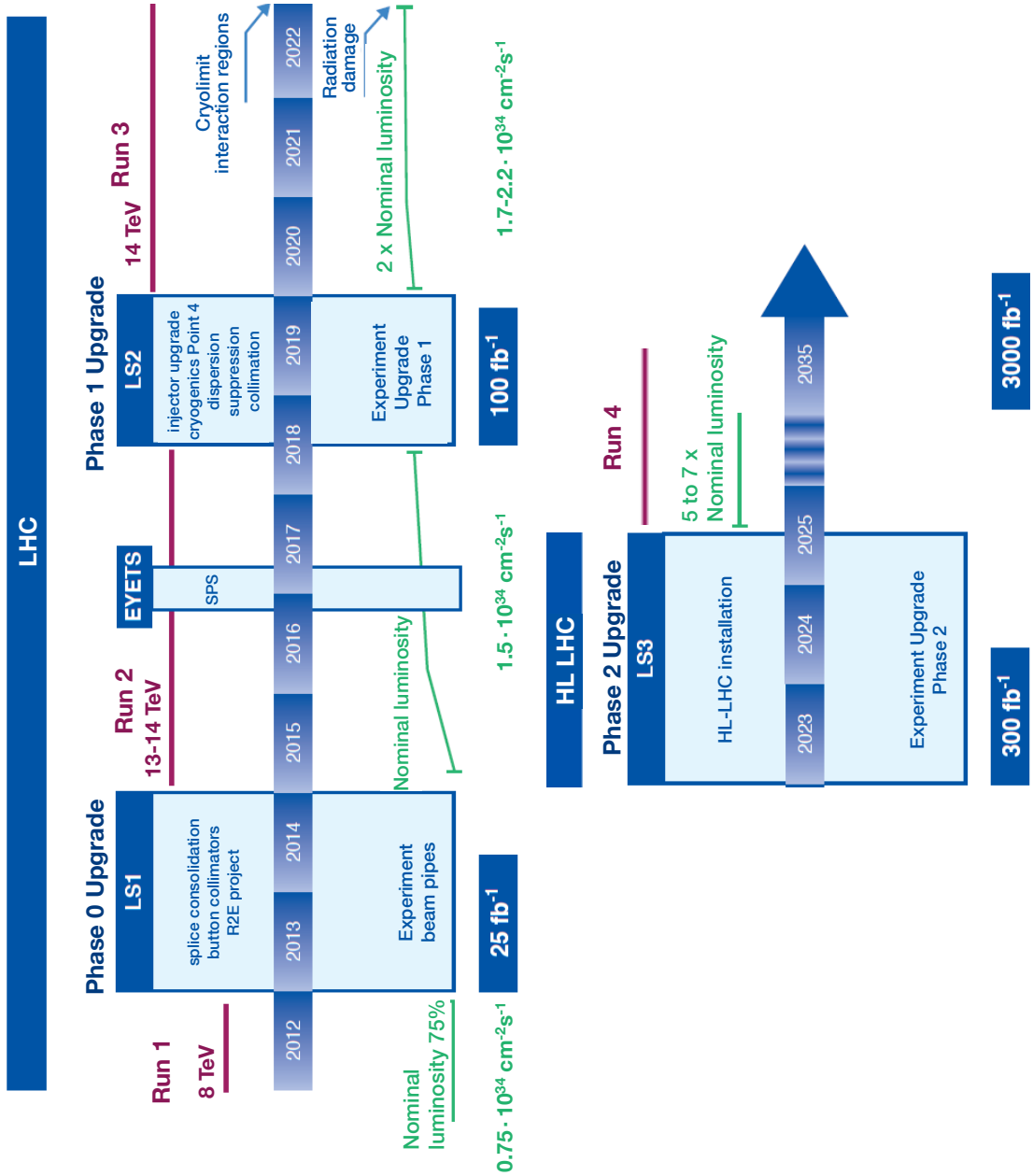

Figure 2.1: LHC long term schedule including performance projection until Phase 2. Three technical long shutdowns are planned for 2013-2014 (LS1), 2018-2019 (LS2) and 2023-2025 (LS3) as well as a long technical stop at the end of 2016 (EYETS). The first three-year LHC running period took place in 2010-2013 (Run1) at a center-of-mass energy of 8 TeV. During 2015-2018 (Run 2) and 2020-2022 (Run 3) the center-of-mass energy increases to 13-14 TeV. After LS3, a luminosity 5 to 7 times the nominal is expected.

2×10^{34} cm^{-2} s^{-1} will be delivered with the data resume in 2020 corresponding to 55 to 80 interactions per crossing (pile-up) with 25 ns bunch spacing. A total integrated luminosity of about 300 fb^{-1} is expected before LS3, extending the reach for discovery of new physics.

During LS3 the LHC will be upgraded to High Luminosity-LHC (HL-LHC) to provide more populated and denser bunches at the collision regions of ATLAS and CMS. Virtual peak luminosities of 5-7$\times10^{34}$ cm^{-2} s^{-1} will be reached at the beginning of LHC fills, corresponding to up to 200 interactions per crossing and a total integrated luminosity of about 3000 fb^{-1}, a factor 10 more than Run 3.

The LHC consolidation and upgrades are necessary to reach the extreme performance foreseen for the next decades. These achievements will be possible only with integration of new features and replacement of several LHC machine components. Operation with increasing rates and pile-up will become more and more challenging for the experiments. The major upgrades of LHCb and ALICE will take place during LS2 with the redesign of read-out electronics and the replacement of some sub-systems to improve precision measurements and to overcome the limits set by detector constraints related to the increasing of integrated luminosity [20], [21]. The detector performance degradations due to the integrated radiation dose will also need to be addressed for the HL-LHC era. ATLAS and CMS will require substantial upgrades to follow the LHC improvements. A staged upgrade program through the long shutdowns is proposed [22], [23], [24]. The major upgrades will take place in LS3 to replace systems due to radiation damage, obsolescence or inability to read-out at HL-LHC data rates as well as to maintain appropriate performance for physics in the very high pile-up environment.

In the next sections, a brief overview of the main LHC detectors upgrade programs, as foreseen today, is provided.

2.2 Motivation and requirements for Tracker Upgrades

The identification and reconstruction of particles created during collisions at LHC is primarily done by tracking detectors. Their characteristics and performance allow also the reconstruction of short-lived particles such as charm and beauty mesons that would be impossible or rather difficult with other types of detectors. Their tracking capability is fundamental for physics analysis and for its preservation at higher luminosity LHC phases, the four LHC tracking systems need to be upgraded. The ATLAS and CMS tracking systems will suffer more the increased luminosity since they were designed to operate efficiently up to an integrated luminosity of about 500 fb^{-1}, which corresponds to the luminosity that will be accumulated at the end of Run 3. The major reason of these upgrades is the longevity of the present trackers. The Pixel Detectors (the innermost tracking detectors) are the first sectors of the tracker that will show limitations at high rates and therefore they are being upgraded for both ATLAS and CMS experiments before LS2.

ATLAS took advantage of the first shutdown period (Phase 0, 2013-2014) for the installation of a new innermost barrel layer in the Pixel detector, the Insertable B-Layer (IBL) [25] as well as for detector consolidation works, including a new inner detector cooling system, a diamond beam monitoring, the replacement of the Pixel internal services, new power supplies for the calorimeter and a new beam pipe. IBL is an additional 4^{th} pixel layer, which is located between

a new smaller radius beam pipe and the previous innermost pixel layer (B-layer). It will improve the vertex resolution, secondary vertex finding and b-tagging, hence extending the reach of the physics analysis. Moreover it will compensate for defects (irreparable failures of modules) in the existing B-layer, assuring tracking robustness (Figure 2.2(a)). IBL has been installed at the core of the ATLAS experiment in May 2014. A detailed overview of the IBL detector and of its performance is given in Chapters 3 and 4.

The CMS strategy foresees a complete Pixel Detector upgrade [26] during the extended winter technical stop in 2016-2017: the new detector will feature 4 barrel layers and 3 forward discs, yielding on average one more spatial point measurement per track compared to the present system, in the whole acceptance range. The goal of the upgraded Phase1 Pixel Detector is to be fully efficient at a luminosity of $2\times10^{34}\,\mathrm{cm}^{-2}\,\mathrm{s}^{-1}$, with less material and with four hit coverage up to $|\eta|<2.5$. The improvements of the Phase 1 Pixel detector have a net effect on the expected performance: pattern recognition, track parameter resolution, vertexing, and b-tagging performance of the upgraded detector are expected to be significantly better than in the current detector (Figure 2.2(b)).

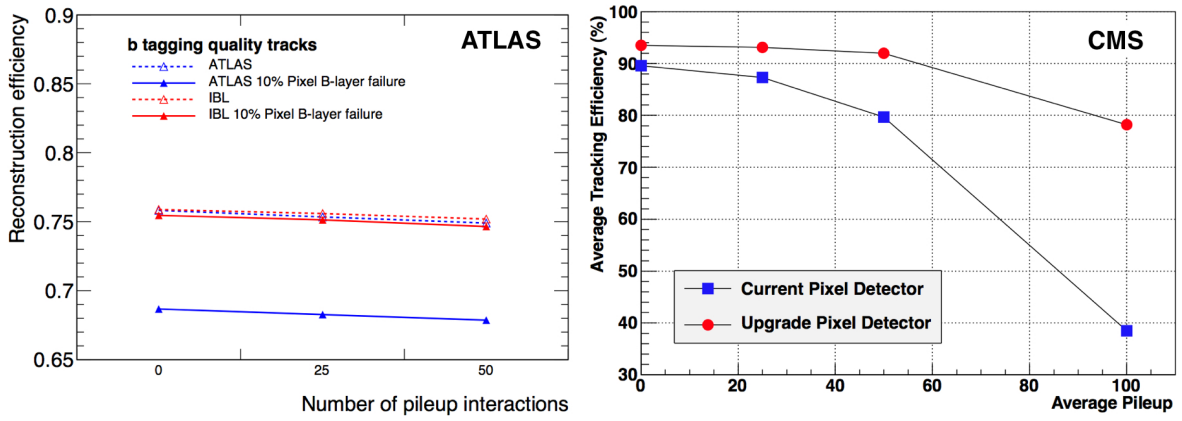

(a) (b)

Figure 2.2: (a) Efficiency for b-tagging-quality tracks with and without additional detector defects as a function of the average number of pileup events, for a detector with and without IBL for the ATLAS experiment [25]. (b) Tracking efficiency performance of the current CMS pixel detector (blue squares) and upgrade CMS pixel detector (red dots) for $t\bar{t}$ events [26].

Both ATLAS and CMS pixel detector upgrades will help to cope with the increased integrated luminosity but they will be not enough for the LHC Phase 2. The ATLAS and CMS trackers will be completely replaced during LS3 by pixel detectors made of hybrid pixel sensors with smaller pixel size surrounded by large outer trackers also made of silicon sensors. The baseline technology for the outer trackers is n-in-p planar sensor while for pixel detectors several option are still under study, as thin planar silicon, 3D silicon sensor, CMOS, etc. The basic requirements of the new trackers are: high radiation hardness (ultimate integrated luminosity considered 3000 fb^{-1}), high granularity (efficient pattern recognition and tracking with pile-up of 140-200), improved material budget with the consequence of improving the tracking performance (Figure 2.3). The biggest changes compared to the current tracker are: an extension of the pixel system out to larger radii, more pixel hits foreseen in forward direction to improve tracking and the use of smaller pixels and short inner strips to increase the granularity.

Furthermore, in the ATLAS case the Transition Radiation Tracker (TRT), made of 300000 gas straw tubes, will be completely substituted by silicon detectors since the 5 to 10 times higher detector occupancy will be beyond the TRT performance. An important point, common to both experiments, is the low power electronics and ASICs: new complex chips in novel technologies need to be developed.

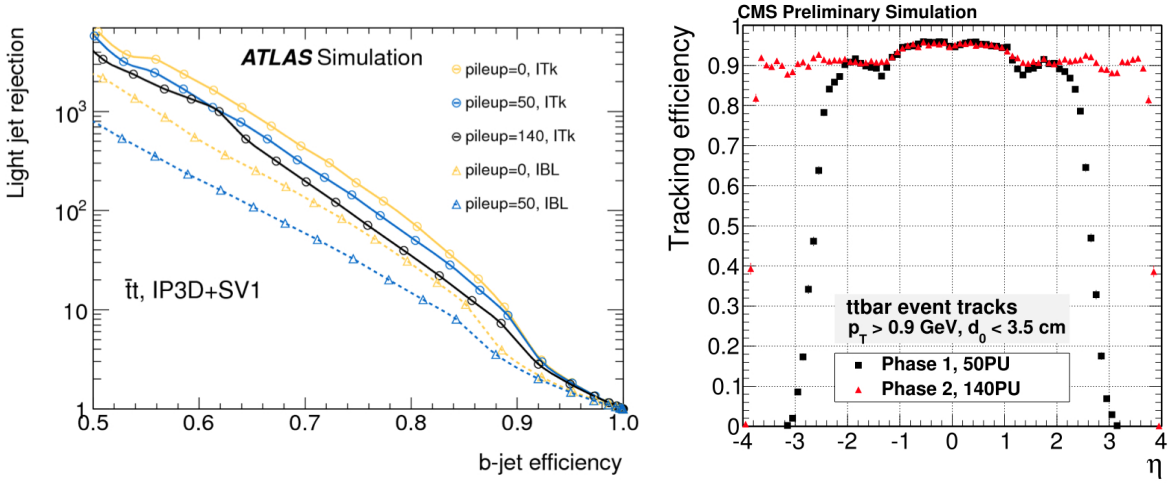

(a) (b)

Figure 2.3: (a) Performance of b-tagging in $t\bar{t}$ events, for a range of pile-up levels for the proposed Phase-2 Tracker layout in comparison with the current ID for the ATLAS experiment [23]. (b) Tracking efficiency as a function of η for the CMS tracker during Phase 1 and 2 [24].

The ALICE and LHCb tracker systems will be upgraded to cope with higher event rates during LS2 [20], [21]. Indeed, ALICE will have to read out data related to each individual interaction at a rate of 50 kHz for Pb-Pb collisions with the goal of having high precision measurements of rare probes at low p_T and a target recorded PbPb luminosity $\geq$10 nb^{-1}. This will require a new inner tracking system with higher rate capability and an upgrade of the rate capability of the Time Projection Chamber (TPC). Furthermore a very low material budget is necessary for high efficiency tracking of low p_T. The new Inner Tracking System (ITS) [27] will be made of seven layers of monolithic pixel detectors of very small pixel size ($20\times20\,\mu$m^2), produced in a 0.18 μm CMOS process. The TPC will be upgraded substituting wire detectors with Gas Electron Multiplier (GEM) detectors [28]. On the other hand, LHCb is targeting operation at a readout from 1 MHz to 40 MHz and at a luminosity of 2×10^{33} cm^{-2} s^{-1}, a factor of ten higher than the original design values. To achieve these results, a replacement of all FE-electronics, event builder and new computing farm will be necessary. A further requirement will be the change of some sub-detectors with silicon sensors. For example, the LHCb Vertex Locator (VELO) will adopt hybrid pixels with thin sensors and small pixel size ($55\times55\,\mu$m^2) [29]. For the large stations behind the magnet, scintillating fibers with SiPM read-out will replace the existing straw tubes.

A common effort of all LHC experiments is also devoted to mechanics and cooling. The material budget is crucial to avoid interaction and scattering into the mechanical parts of the detector and the thermal management plays a crucial role due to the high power densities. Novel

materials and technologies have been developed or are under study for material and cooling improvements. For example, the two-phase CO_2 cooling is the technology of choice for most future trackers, as it is already for ATLAS IBL and LHCb VELO.

2.3 Motivations and Requirements for Calorimeter Upgrades

Calorimeters provide essential input for the precise measurement of basic physics objects and complex global event topologies, as well as being vital to the triggering capabilities of all the LHC experiments. For ATLAS and CMS, the very challenging HL-LHC environment imposes a change in the input of the Level-1 trigger systems for more selective and sophisticated trigger algorithms based on high granularity and high precision calorimeter information. This requires both increased bandwidth and longer latency of the read-out systems. A common goal of the four experiments is to provide the highest possible granularity and resolution information to the trigger processors for handling the increasing pile-up. In the ATLAS case, the calorimetric trigger will have an upgrade in Phase 1 to provide finer granularity, higher resolution and longitudinal shower information for the Level-1 trigger decision. In the barrel region 10 super-cells instead of 1 trigger tower will improve the trigger energy resolution and efficiency for selecting electrons, photons, τ leptons, jets and missing transverse momentum while enhancing discrimination against background and fakes (Figure 2.4(a)). The calorimeter systems of ALICE and LHCb expect a read-out upgrade during LS2. A particular mention has to be addressed to the CMS experiment where the replacement of the two calorimeter systems is planned [30]. Indeed the performance of both the CMS end-cap Calorimeter ECAL (homogeneous $PbWO_4$ detector) and the Hadronic Calorimeter (sampling detector based on plastic scintillating tiles) would substantially degrade due to the radiation levels at the HL-LHC (Figure 2.4(b)). A R&D program is underway to meet all challenges of replacing the end-cap calorimeters during LS3. Furthermore already in LS2, a change of photodetectors in hadron barrel and end-cap calorimeters is foreseen.

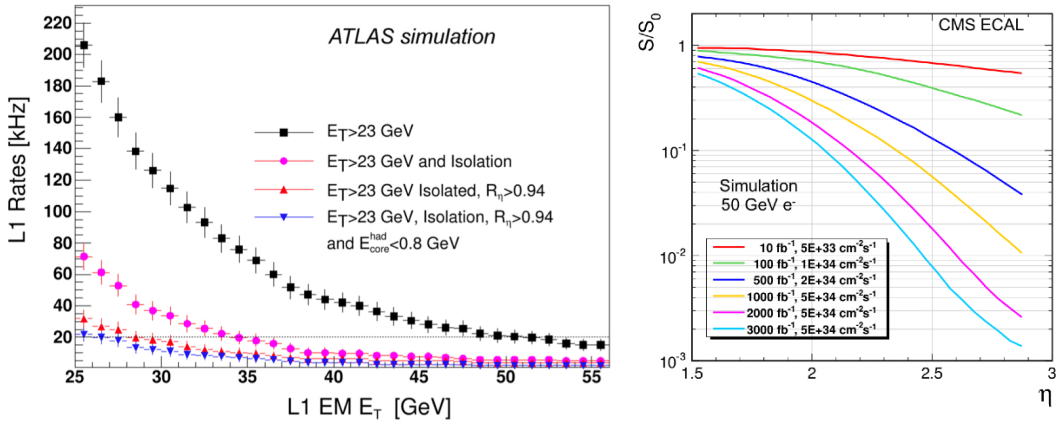

(a) (b)

Figure 2.4: (a) Expected Level-1 rates for different algorithms and conditions: the current Level-1 rate for non-isolated EM objects, for isolated EM objects, for isolated EM objects after a shower shape R_η>0.94 cut applied in the ATLAS experiment [22]. (b)The extrapolation of the response evolution of the CMS ECAL end-cap up to an integrated luminosity of 3000 fb^{-1} [30].

2.4 Motivations and Requirements for large Gaseous Detector Systems Upgrades

Gaseous detectors are widely used in the LHC experiments for tracking, trigger and particle identification. The LHC muon systems are fundamental for muon identification and momentum measurement and they have shown excellent performance during the first LHC run. Most of the detectors used in muon systems are gaseous detectors either using wires (drift and wire chambers) or without wires (resistive place chambers), which have been designed and built to operate for about 10 years at LHC. Three major aspects need to be addressed for the future operation of gaseous detectors at LHC: performance degradation (due to aging, high luminosity, etc.), read-out electronic limitations (high rate, trigger scheme, etc.) and generation of fake hits.

Even if the detectors of muon systems will experience the least issues with integrated radiation doses, a continuos monitoring of performance is necessary to verify their response under higher particle fluxes and to spot any possible weaknesses or failures. Only in the forward regions, where particle and background rates are higher, a replacement or addition of new detectors is foreseen.

LHC high luminosity requires improved timing resolution and greater trigger sharpness, which will exceed the capability of most of muon systems present electronics. The main affected systems will be in ATLAS and CMS, particularly for the forward regions where the accuracy of the p_T measurements will be improved by installing additional detectors [23], [24]. On the contrary, ALICE and LHCb emphasize greater precision measurements and plan to maximize the number of recorded events by going to continuos read-out where hardware trigger electronics will be taken over by software trigger algorithms [20], [21].

In the last decades a huge effort has been addressed to develop Micro Pattern Gaseous Detectors (MPGD). MPGDs offer several advantages for LHC experiments, as high rate capability, high energy and space resolution, high granularity and fast collection time as well as very low sensitivity to aging. Thanks to these features and the possibility to scale to large systems, several MPGD technologies have been proposed for the LHC upgrades.

The ATLAS experiment has adopted two different gaseous detector technologies for its LS2 muon upgrade program: the MicroMegas (MM) for precision tracking and Small-strip Thin Gap Chambers (sTGC) for the Level-1 trigger function. These detectors will constitute the New Small Wheel (NSW) [31], which replaces the existing Muon Small Wheel (MSW). Indeed it has been demonstrated that in the ATLAS experiment about 90% of the muon triggers in the end-caps are fake or background dominated by low energy particles, which are created in the material located between the MSW and the middle station, and they can be confused with real high p_T muons (Figure 2.5(a)). The installation of the NSW will allow an improved tracking and trigger capabilities satisfying the Phase 2 requirements. The MMs will cover an area of 1200 m^2 with high granularity and rate capability due to small gas amplification region and small space charge effect. A very good precision is crucial to maintain the current ATLAS muon momentum resolution in the high background environment of upgraded LHC. The trigger improvement is given by the sTGC thanks to their single bunch crossing identification capability with a good timing resolution to suppress fakes.

The CMS experiment has the least robustness and redundancy in tracking and reconstruction capabilities for the high η region, where muon identification relies only on the Cathode

Strip Chamber (CSC) system. The main challenge for triggering in this region at high luminosity is high background rates. An intense R&D effort has led to the proposal of equip two stations in the endcap region (GE1/1 and GE2/1) with triple Gas Electron Multipliers (GEMs) [32]. The installation of 36 double-layered triple-GEM chambers in $1.55<|\eta|<2.18$ during LS2 (GE1/1 system) and a second installation of two rings of double-layered triple-GEM chambers in $1.6<|\eta|<2.45$ during LS3 will reduce the trigger rate in this region thanks to the improved momentum resolution (Figure 2.5(b)). The detectors will have to sustain background rates up to 10^5 kHz/cm^2 at the instantaneous luminosity expected for Phase 2. Most of triple-GEMs have a trapezoidal shaped area with a 3/1/2/1 mm field gap configuration, which is usually used with a CF_4 based gas mixture to allow a fast signal collection.

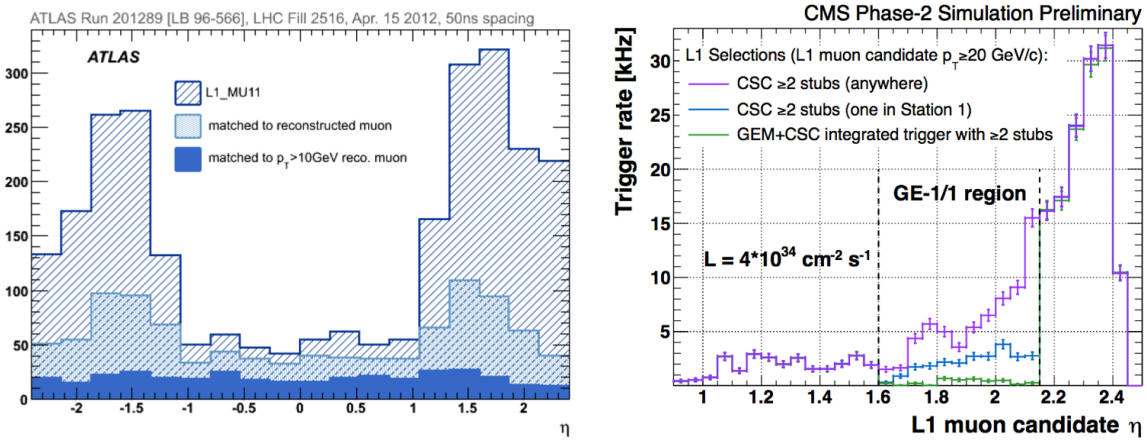

(a) (b)

Figure 2.5: (a) η distribution of Level-1 muon signal L1_MU11 distribution of the subset with matched muon candidate to an offline well reconstructed muon and offline reconstructed muons with p_T>10 GeV for the ATLAS experiment [31]. (b) Trigger rate distribution for high p_T muon candidate as a function of η in the scenario with and without GEM detectors for the CMS experiment [32].

The third experiment using MPGD technology is ALICE, which will need to improve the rate capability of its TPC. Nowadays the trigger rates are restricted to about 1 kHz due to the use of Multi Wire Proportional Chambers (MWPCs) in the TPC. GEM detectors can be operated in a continuous, triggerless readout mode, allowing an increase in event rate by a factor of 100. Although charge amplification by GEM foils offers an intrinsic suppression of the ion backflow, R&D studies have been necessary to reach a value well below 1%. ALICE will implement GEM foils instead of MWPCs in the read-out planes with corresponding new electronics during LS2 [28].

Besides the detectors upgrades, common topics for the four LHC experiments are related to the gas mixtures used in such large systems and to greenhouse gas emissions, in particular to their contribution to climate changes and for cost saving. Indeed, possible future restrictions will be addressed on the use of $C_2H_2F_4$ (R134a), SF_6 and CF_4. The $C_2H_2F_4$ is the main component of the Resistive Plate Chamber (RPC) gas mixture and it is used in ATLAS, CMS and ALICE experiments, each one with a gas volume of about 15 m^3. Also the SF_6 is a component of the RPC gas mixture and even if its concentration is 0.3%, its contribution is relevant since it

has a very high Global Warming Potential (GWP)[1]. The RPC gas mixture is recirculated in the system, nevertheless about 5-10% of fresh mixture needs to be injected. The case of CF_4, used for GEM, CSC and RICH detectors at the LHC will be discussed in Section 5.5. In particular, the CMS CSC system will be used as an example of reducing gas emission through the development and operation of a dedicated recuperation plant (Section 5.6). New R&D studies have started aiming in replacing expensive or high environmental impact gases. Section 6.3 describes the tests for evaluating performance of RPC detectors operated with a new freon having a very low GWP. However, years of R&D are still needed before any conclusion can be drawn about the use of new gases at LHC.

2.5 Conclusion

The upgrade program of the LHC accelerator is setting important challenges to all detector communities. In order to achieve the required performance, new detector technologies are being developed and others will be used at large scale in the years to come. Two examples of detector performance optimization are discussed in details in the present work: the IBL Detector and the gaseous detectors (in particular CSC, GEM and RPC).

The IBL Detector is the example of the general pixel detector strategy for future upgrades. New sensor technologies and front-end electronics have been developed as well as less invasive services (CO_2 cooling) and mechanical supports to reduce material budget. These detectors will be operated until radiation damage effects will become too important and then they will be replaced with newer generation detector technologies.

The case of gaseous detectors is quite different. In general, they are very large apparatus and it is unthinkable to replace the full system. Therefore, the activity is addressed to the optimization of gas mixtures and gas systems allowing to reduce operational costs and gas emission maintaining or improving the detector performance. New layers of detectors will be added, especially in the forward regions, where the increased particle rates will become an issue for triggering and track reconstruction. These new detectors will benefit of all on-going R&D studies about detector performance, improved gas recirculation, gas monitoring systems and new environmental friendly gases.

[1]The GWP is a relative measure of how much heat a greenhouse gas traps in the atmosphere. It compares the amount of heat trapped by a certain mass of the gas in question to the amount of heat trapped by a similar mass of CO_2.

Chapter 3

The ATLAS Pixel Detector Upgrade during the first LHC long shutdown

During the next years the ATLAS Pixel Detector will have to cope with an increase of luminosity, which will bring higher pile-up and radiation damage. The most affected layer will be the innermost layer (B-layer), whose operation is critical to the full realization of the physics capabilities of the ATLAS experiment. Good vertexing and b tagging performance have to be ensured for the remainder of the LHC Phase 1 physics program. This can be accomplished with the installation of a fourth layer of pixel modules inside the B-layer: the Insertable B-Layer (IBL). The IBL will improve the overall Pixel Detector performance, compensating inefficiency, radiation damage and losses of pixels by adding redundancy in the system for the LHC Run 2 and 3 periods. The refurbished Pixel Detector has been designed to operate efficiently up to an integrated luminosity of 500 fb^{-1} that will be reached at the end of Run 3 when the ATLAS tracking system will be completely replaced.

This chapter will briefly introduce the IBL Detector. The installation of a fully efficient and functional detector has to be considered a "must" given the IBL location inside the ATLAS experiment. A careful attention has been dedicated to the quality control and quality assurance aspects, which will be described in detail in the next chapter.

3.1 Upgrade of the Pixel Detector during LS1

Before LS1, the ATLAS Pixel Detector [33], which is the innermost detector of the ATLAS experiment, was made of 1744 modules, which were located in three barrel layers and three end-cap disks on each side for a total of about 80 millions readout channels (Figure 3.1). It provided three high-resolution measurements points in the pseudo-rapidity[1] region $0 < \eta < 2.5$, reaching a resolution of 10 μm in Rϕ and 110 μm in z.

An ATLAS Pixel Module has a 250 μm thick n^+-in-n silicon sensor divided in 47232 pixels with a nominal size of 50$\times$400 μm^2. Each of these pixels is bump bonded to one readout cell

[1] ATLAS uses a right-handed coordinate system with its origin at the nominal interaction point in the centre of the detector and the z-axis along the beam pipe. The x-axis points from the interaction point to the centre of the LHC ring, and the y-axis points upwards. Cylindrical coordinates (r,ϕ) are used in the transverse plane, ϕ being the azimuthal angle around the beam pipe. The pseudorapidity η is defined in terms of the polar angle θ as $\eta = -\ln\tan(\theta/2)$.

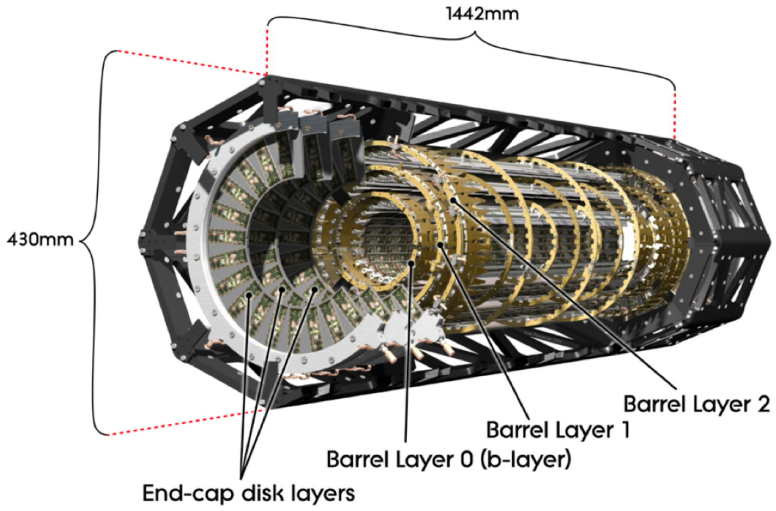

Figure 3.1: Layout of the ATLAS Pixel Detector with 3 barrel layers and six disks, three for each region [33].

of a front-end chip (FE-I3). A pixel module has 16 FE-I3, which are combined in one timing, trigger control and readout by the Module Control Chip (MCC). The data transfer readout is 160 Mbit/s for the innermost layer (B-Layer), 80 Mbit/s both for Layer 1 and disks and 40 Mbit/s for Layer 2 since the readout link speeds are tuned by design to the expected data rate.

The ATLAS Pixel Detector showed excellent performance over LHC Run 1; during 2012 the data taking efficiency was 99.9% [2] and the radiation effects observed during operation are within expectations, the most visible being the change of leakage current and depletion voltage.

Despite the overall good performance, the number of disabled and problematic pixel modules increased from 1.5% to 5% during LHC Run 1, especially because of read-out issues (Figure 3.2(a)). The Pixel Detector readout system has to cope with an average pile-up of 20.7 interactions per bunch crossing (BC), which are already beyond the design specifications. Indeed readout limitations would degrade Pixel Detector performance before radiation damage does.

The Pixel Detector was extracted from the ATLAS Experiment during LS1 for an intensive upgrade and consolidation campaign. The major upgrade was the installation of the new innermost layer IBL [25], which is described in Section 3.2. The extraction allowed other important upgrades: the replacement of Pixel Service Quarter Panels (SQPs)[3] with new Service Quarter Panels (nSQPs) [34], the extended campaign to classify and repair non-working pixel modules, the installation of a new Diamond Beam Monitoring [35] and the addition of hardware to double the readout speed of Pixel Detector Layers 1 and 2.

The modules recovery obtained with the replacement of SQPs is outstanding: about 75% of disabled modules were recovered on the surface. The Pixel Detector was re-installed into the ATLAS Experiment in December 2013. After the reconnection of the services, few new modules found faulty due to opening of HV or LV lines as well as the impossibility to data

[2]Data delivered during stable beams for 21.3 fb^{-1} pp-collisions and considered as good for physics by the data quality criteria.

[3]The SQPs are installed with the detector and carry electrical power, cooling and optical data both into and out of the detector. They also house the electro-optical converters (Optoboards), which enable bidirectional conversion of electrical and optical signals.

readout, as it is summarized in Figure 3.2(b). At the beginning of LHC Run 2, the total disabled modules will be 33, about 2%.

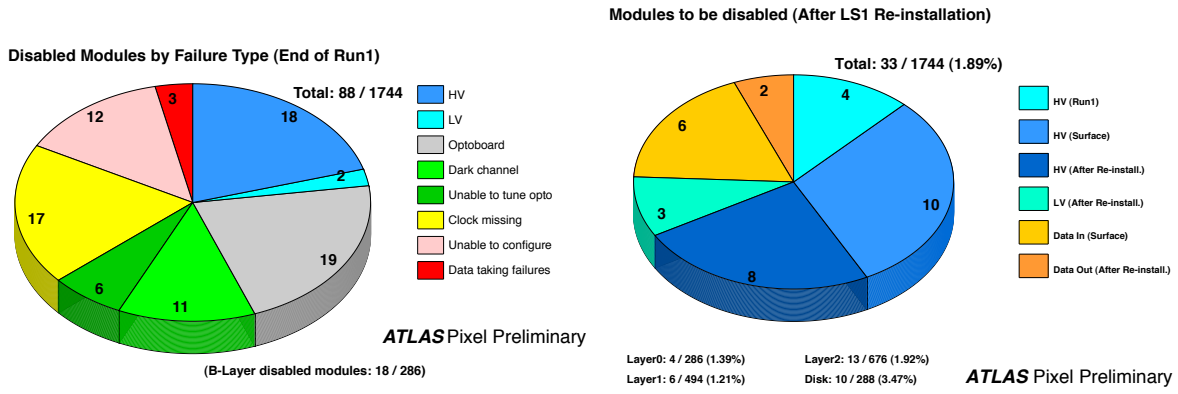

(a) (b)

Figure 3.2: (a) Number of disabled modules of the Pixel Detector at the end of Run1 classified by type of failure. (b) Number of modules of the Pixel Detector to be disabled after re-installation in ATLAS Experiment classified by failure mode (HV/LV/Data In/Data Out) and the phase causing problems (Run1/Surface/After re-installation). Modules having performance issues but being operable are not included [36].

3.2 The IBL Detector

The Insertable B-Layer [25] is the fourth layer added to the Pixel Detector between the new beam pipe and the current innermost Pixel layer (B-layer). Thanks to IBL, the Pixel Detector is closer to the interaction point, improving the overall ATLAS physics performance.

The achievement of an innovative and sophisticated detector has been possible only developing new read-out and sensor technologies, which will be able to cope with high radiation and pixel occupancy.

A brief overview of the IBL characteristics and peculiarities will be provided in the next sections.

3.2.1 Improvement of the ATLAS performance with the IBL

The IBL improves the overall performance of the Pixel Detector and ATLAS experiment by enhancing the quality of impact parameter reconstruction for tracks (improving vertexing and b tagging performance). Furthermore, even in case of a complete B-layer failure, IBL can restore the full b tagging efficiency. The addition of a fourth layer will also help in mitigating luminosity effects such as the increase of event pile-up, which leads to high occupancy and readout inefficiency, and the large radiation doses accumulation thanks to a more robust pattern recognition. Detailed simulations of the Inner Detector (ID) performance with and without IBL have been performed. The IBL Detector has been fully integrated in the ATLAS ID software and its response is based on the existing Pixel digitization algorithm [37]. In the simulation, three substantial differences with respect to the Pixel Detector have been taken into account:

wider range of particle incident angles in the Rϕ plane, wider clusters in the z direction and lower Time over Threshold (ToT) resolution.

The IBL is expected to improve the impact parameter as well as the primary and secondary vertex resolutions. The most important parameter for b tagging performance is the impact parameter resolution, which is estimated using several algorithms. For IBL studies, the default ATLAS impact parameter-based b tagging algorithm (IP3D) and secondary vertex based algorithm (SV1) are used[4] [38]. Figure 3.3 shows the impact parameter resolution at different η for tracks in $t\bar{t}$ events with $2\,GeV < p_T < 4\,GeV$. The impact parameter resolution improves in both planes. The deterioration towards higher pseudorapidity is due to the increase of cluster size in the z-direction and to multiple scattering effects in the innermost materials and beampipe. Figure 3.4 shows the d_0 impact parameter significance distributions[5] for b, c and light jets

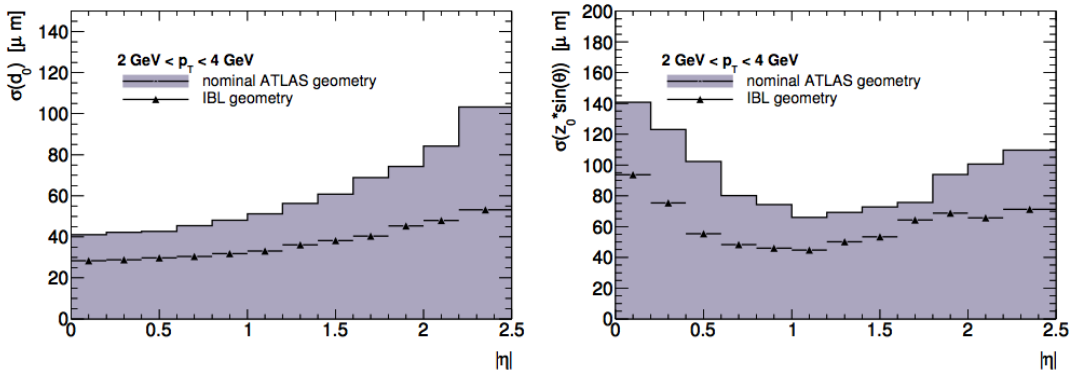

Figure 3.3: Impact parameter resolution as a function of η for tracks in $t\bar{t}$ events without pileup. Results with and without IBL are compared; (right) transverse impact parameter distribution d_0 and (left) longitudinal impact parameter distribution $z_0 \times \sin\theta$ with respect to the true primary vertex position of the event [25].

in $t\bar{t}$ events reconstructed with and without IBL: a clear excess of tracks from b and c hadrons is visible in the tail at positive significance, meaning a b tagging capability. Finally IBL will improve also the resolution for the reconstructed primary vertex from 15 μm to 11 μm (RMS) in x and from 34 μm to 24 μm in z.

3.2.2 IBL sensor and front-end technologies

The central performance and operational challenges for the IBL system provide severe and difficult constrains on the IBL components:

- The high radiation dose foreseen in the LHC Phase 1 makes radiation hard technologies mandatory. In the readout electronics a total ionizing dose of 250 Mrad at the IBL end of lifetime is expected.

[4]The IP3D tagger algorithm uses both the longitudinal and the transverse impact parameter. The SV1 tagger uses the invariant mass of the fitted vertex, the ratio of energy in the vertex compared to the total energy in the associated jet and the number of two-track vertices used for the inclusive vertex.

[5]The displacement between the primary vertex and the tracks reflects that tracks are not prompt tracks from the primary vertex but they originate from a secondary particle decay. The displacement is quantified by the signed transverse impact parameter significance (IP-Sig) $S_{d0} = d_0/\sigma_{d0}$ where σ_{d0} is the error on the d_0 measurement.

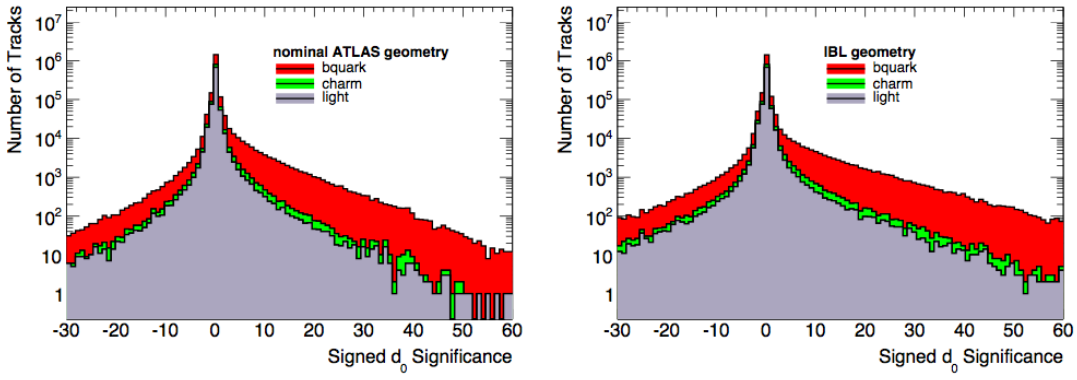

Figure 3.4: Transverse impact parameter significance distributions, signed with respect to the jet axis, for b, c and light jets from $t\bar{t}$ events without pileup. Compared are results with the present ID (left) and with the IBL added (right) [25].

- The reduction of the geometrical inefficiency, especially along the z direction, can be reached with an improvement of sensor using an active edge or a slim guard ring. A full coverage in the ϕ angle can be obtained with modules with the same active width but with only one row of front-end chips.

- The optimization of tracking and vertexing performance can be enhanced minimizing the material budget both for modules and IBL materials. The sensor thickness has been reduced to about 200 μm and the front-end chip is 130 nm CMOS technology. A special attention has also been addressed to electrical and mechanical parts as, for example, the use of kapton flex for data and service transmission and CO_2 as evaporative cooling. The IBL radiation length is just 60% of the present Pixel B-layer.

- The tight tolerances and clearances of the IBL detector has to be taken into account also for services. The whole IBL package is 7 m long (a stave is 64 cm long) and the radial clearance for insertion in the Pixel Detector is only 2 mm.

IBL planar silicon pixel sensor design

The IBL planar sensor is an electron-collecting n^+-in-n silicon sensor design fabricated by CiS[6] [39]. It has a thickness of 200 μm and it needs an adequate detection efficiency following fluences up to $6{\cdot}10^{15}$ n_{eq}/cm^2 while the ATLAS Pixel sensor is 250 μm thick and is specified for a fluence of 10^{15} n_{eq}/cm^2.

The readout electrodes are n^+-doped implants separated by modulated p-spray and a single p^+-doped high voltage pad at the back side. The p-spray is adopted to guarantee the inter-pixel isolation and the p^+ implantation is made as a single large high voltage pad opposite the pixel matrix. The n^+ implantation is segmented into a matrix of 160 columns and 336 rows of mainly $250{\times}50$ μm^2 pixels surrounded by an inactive edge region. The pixels in the central double column are enlarged to $450{\times}50$ μm^2 to accommodate the region between the two front-end chips. The outermost pixels are extended to 500 μm length overlapping the guard ring structure by 250 μm. A bias-grid has been adopted to allow access to the sensor before flip-chip and to

[6]CiS Forschungsinstitut fur Mikrosensorik und Photovoltaik GmbH, Germany.

avoid a floating potential on pixels having an open bump connection. It consists of metal lines that provide the possibility to connect the bias dot to ground. Each pixel, the bias grid and the outer guard are connected to the read-out chip via bump-bonds.

Particular care has been provided to the edge termination for minimizing the dead areas in the IBL Detector. A 13 guard rings implantation with a total width of approximately 350 μm is shifted into the active pixel region under elongated 500 μm wide edge pixels to minimize the inactive edge to 200 μm while in previous ATLAS Pixel sensor 16 guard rings were used in a more extended area (Figure 3.5). This implantation is used to generate a well controlled potential drop from the high voltage pad to the sensor edge.

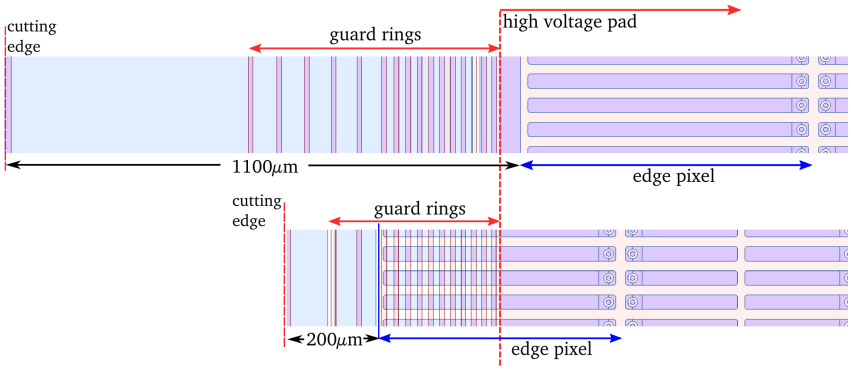

Figure 3.5: Comparison of the edge region of the current ATLAS Pixel design (upper) and the IBL planar sensor design (lower). The difference in region with p^+-doped guard rings is visible for both Pixel and IBL sensor design as well as the minimization of the edge termination area [39].

IBL 3D silicon pixel sensor design

The IBL Detector is the first large scale application of 3D sensor technology. IBL 3D sensors are 230 μm thick produced with the Double-side Double Type Columns process with two n^+ electrodes columns from the front side surrounded by six p^+ biasing electrodes columns from the back side [39]. The distance between the electrodes is 67 μm which leads to a faster charge collection, lower charge trapping probability and lower bias voltages than planar sensors.

The sensors have been developed in cooperation with two different companies: CNM[7] and FBK[8]. The two companies implemented similar processes for the sensor fabrication using the double sided etching technique called Bosch-process, which allows to edge narrow pillars through the silicon bulk. However in CNM sensors the columns do not traverse the substrate but stop at a short distance from the surface of the opposite side whereas FBK sensors have traversing columns (Figure 3.6).

An important feature of 3D sensors is the edge termination, which is different for the two 3D sensor types (Figure 3.7) [40]. FBK sensor has a slim edge, which consists of a multiple fence of ohmic columns extending from the active area toward the scribe line. This structure is intended to shape the electric field so that it is impossible for the depletion region spreading from the outermost junction columns to reach the highly damaged cut region. In this way, no

[7]Centro National de Microelectronica, Barcelona, Spain.
[8]Fondazione Bruno Kessler, Trento, Italy.

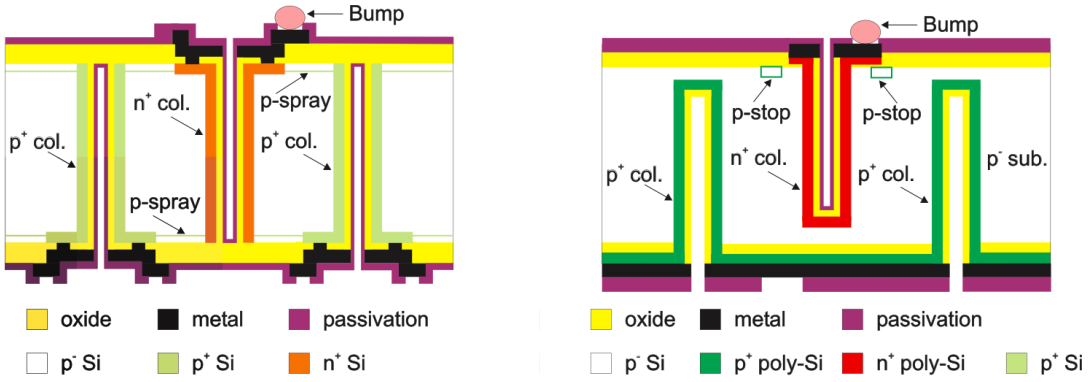

(a) (b)

Figure 3.6: 3D etched columns from the pixel sensor design of the (a) FBK and (b) CNM fabrication facilities [39].

leakage current contribution from the highly damaged cut-line is present. In CNM sensor a guard ring is implemented to drain any parasitic current coming from the edge. Since planar guard-rings are not effective with 3D detectors, a viable solution is to realize a "3D guard-ring" made of both junction columns and ohmic columns with fences that are at the bias voltage from the ohmic side.

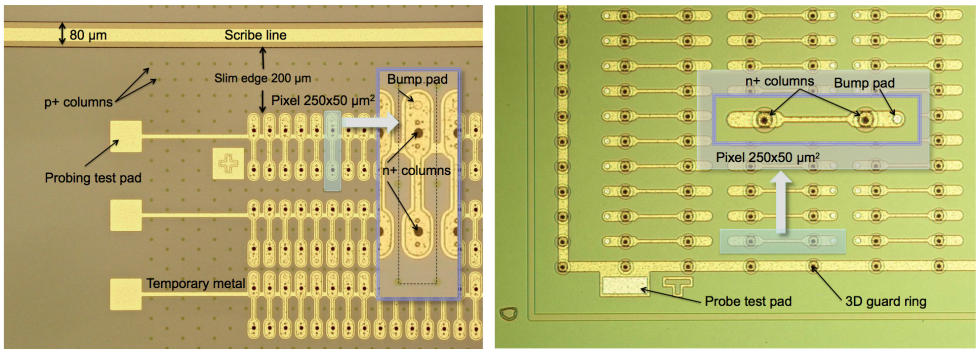

(a) (b)

Figure 3.7: (a) FBK temporary metal used for sensor selection on wafer. On the left, the metal line termination on probing pads are outside the active region to avoid surface damage. The slim edge of 200 μm is visible. (b) Corner picture of CNM 3D sensor showing the guard ring surrounding the pixel matrix active area [40].

IBL front-end chip: FE-I4

The current 3-layer Pixel Detector read-out system is based on the FE-I3 integrate circuit (IC) [33], which has a pixel granularity of 400×50 μm^2 in a 250 nm feature size bulk CMOS process, a size of 7.6×10.8 mm^2 and it has been designed for 100 Mrad ionizing radiation. At the IBL radius, the fluences expected are higher and the FE-I3 limitations, both in term of radiation hardness and ability to cope with high hit rates, make this chip unusable for IBL [41]. A completely new readout chip, the FE-I4 IC [42], is used for IBL: it is radiation tolerant up to 250 Mrad and it has a high efficiency versus luminosity. The FE-I4 is developed in a 130 nm

feature size bulk CMOS process in view of future ATLAS high luminosity pixel applications. It consists of an array of 80×336 pixels (total of 26880 pixels) with a pixel size of 250×50 μm^2 giving a total area of 20.2×18.8 mm^2. The active over inactive area fraction passes from 74% to 89% with a 2 mm high periphery while the power consumption is kept at 26 μW/pix (for FE-I3 is 75 μW/pix).

Each pixel holds an analog and digital circuitry [43]. The FE-I4 analog front-end is implemented as a 2-stage amplifier optimized for low power, low noise and fast rise time, followed by a discriminator (Figure 3.8). Hits are discriminated at the level of a tunable comparator with an adjustable threshold. Charge is translated to Time over Threshold (ToT) with a proportionality factor that the user can tune by changing the return to baseline behavior of the pixel. The feedback currents of the amplifier stage can be adjusted to have all pixels of the matrix affected all at once. A local tuning for each individual pixel is also possible through an additional current adjustment using the 4-bit FDAC, which allows the fine tuning of the ToT response, and the 4-bit TDAC, which allows the fine tuning of the threshold response.

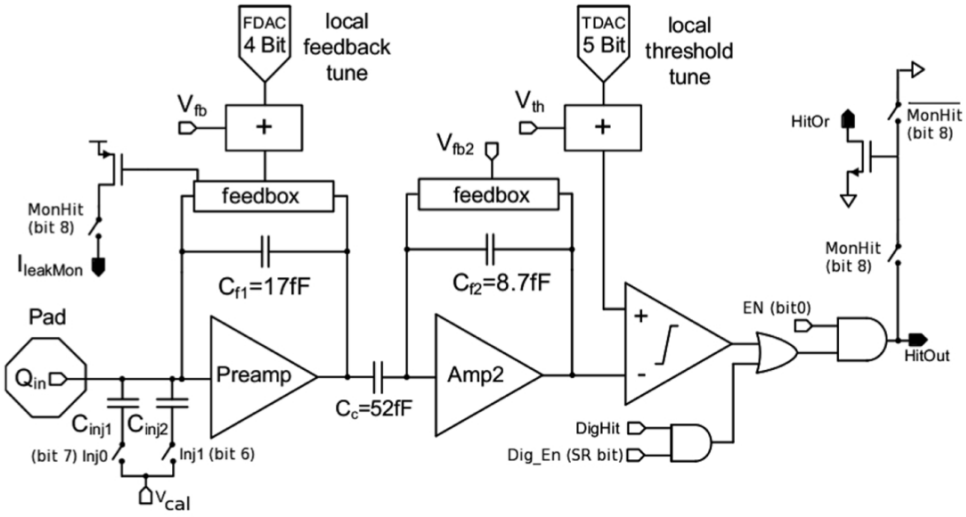

Figure 3.8: Analog pixel section schematic for the IBL FE-I4 [39].

For test purposes and calibration, a test charge can be injected at the pre-amplifier input through a set of two injection capacitors (C_{inj1}, C_{inj2}) using a voltage step defined by the calibration voltage (V_{cal}). The injected charge is given by

$$Q\,[e] = C_{inj}\,[F] \cdot V_{cal}\,[V] \cdot \frac{1}{e\,[C]} \tag{3.1}$$

with e being the elementary charge. Hits can also be injected to an OR element after the discriminator to test the digital part of the pixel. The output of the analog readout chain of each pixel can be disabled using an AND connected to the discriminator output and the enable bit (EN) on each pixel. The output (HitOut) can be connected to the HitOR bus, which is routed to each pixel of the matrix and can be used for test purposes enabling the self trigger operation of the chip.

The FE-I4 pixel array is organized in double columns as the FE-I3 chip even if the readout architecture is very different. Four independent analog pixel channels share a common digital

logic cell (memory and logic block) called Pixel Digital Region. Thanks to this structure, hits are stored close to the analog readout chain and they are processed only if a trigger signal is received (in the FE-I3 chip the buffering of pixel hits is grouped per column pair in the chip periphery). This is an advantage as it enables the FE-I4 chip to work at much higher hit rates than FE-I3 chip. The digital region can store up to five events for four pixels while each pixel holds his own set of five ToT counters. For each event, a counter clocked at 40 MHz keeps track of the time elapsed since the event took place with 25 ns resolution and the charge information belonging to this specific time stamp is stored in the buffers for all pixels connected to the 4-pixel digital region. When an external trigger arrives, it is distributed to all the regions simultaneously within 2 ns, then the transfer of the hit data to the end of chip logic starts and latency counters and buffers memories are deallocated. If the counter exceeds the latency without a trigger, the event is erased.

3.2.3 IBL Layout

Module concept

An IBL module consists of a silicon sensor bump bonded to one or two FE-I4 readout chips, depending if the 3D (single chip) or planar (double chip) sensor technologies are used. The choice between double and single chip module is related to the different yields of the planar and 3D fabrication processes. A flexible PCB, called module flex, is glued on each sensor and wire bonds connect it to the FE-I4, allowing data and services transmission.

The pixel cells on the IBL sensor are connected to the readout channels on the front-end through fine-pitch bump bonds. For each readout chip, 26880 SnAg solder bumps have to be done with a pitch of 50 μm and a failure rate less than 10^{-4}. The critical parameters for the bonding process are the large size of the read out chip and the requirement of a much thinner chip where open bumps can occur at the corners due to the chip bending. This challenge has been overcome modifying the bonding process used at the IZM company[9] [44]. A support glass wafer is glued to the backside of the readout chip to create the necessary thickness for the bump bonding process. After the operation, the support is detached with a laser exposure that dissolves the polyimide glue.

A high failure rate of IBL modules occurred in the first IBL batches during the production in 2012. Two types of failure categories have been defined: “opens”, which are large areas of disconnected bumps, and “shorts”, which are areas or single bump defects distributed over the module. In the second case the chip failure rate reached about 85%. The problem was related to excessive flux in the flip chip process and it was solved by changing the bonder and using a flux-free flip chip. The original issue was not observed in later batches.

After the flip-chip process, a flex hybrid (called “module flex”) is glued with an epoxy glue (UHU EF 3000) on the back of the sensor to provide the connection between the readout electronics and the external services. This module flex is a two copper layer flex circuitry of 130 μm thickness with passive SMD[10] components loaded on it. Two types of module flexes are built to be compatible with SC and DC modules. The last step of the module dressing is the

[9] Fraunhofer-Institut fur Zuverlassigkeit und Mikrointegration, Gustav-Meyer-allee 25, 13355 Berlin, Germany.
[10] Surface Mounted Device.

wire bonding of readout chip and sensor to the module flex using 25 μm diameter aluminum wires. Figure 3.9 shows photos of dressed IBL single chip and double chip modules.

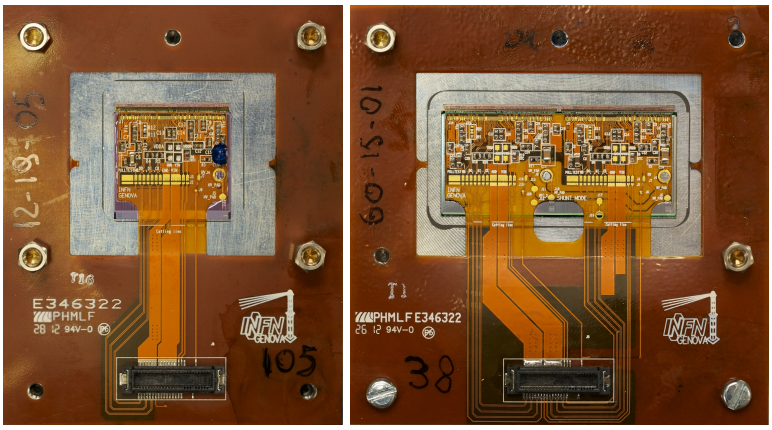

(a) (b)

Figure 3.9: Photo of a dressed IBL (a) single chip and (b) double chip modules. The flex extension is present to allow testing the module prior to its loading on the stave.

Stave layout

A bare stave is a 64 cm long object based on carbon foam material. It provides a path for the heat generated in sensors and front-end chips to the cooling CO_2 fluid boiling at low temperature in the cooling channel, which consists of a 1.7 mm diameter titanium pipe inserted in the carbon foam. Due to material budget and space constraints the services have to be tightly integrated with the stave itself. This requirement is accomplished gluing a so called "stave flex" on the opposite side of the stave. A single stave is served by two flexes, which provide the electrical connection of all modules to the end of stave card. A stave flex is a mixed multi-layer circuit, which holds four copper layers for signal links and high voltage lines and two additional aluminum layers for supply voltage and return lines.

Each stave holds 20 IBL modules: 12 Double Chip planar sensors, which cover the region $-2 < \eta < 2$, and 8 Single Chip 3D sensors, which are located at both ends of the stave (4 on each side) for a total of 32 FE-I4 chips (Figure 3.10).

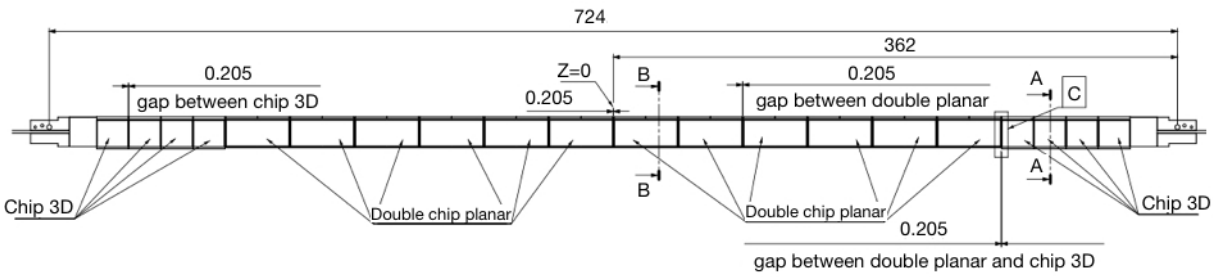

Figure 3.10: Layout of an IBL stave showing the modules placement [25].

Design concept of the IBL Detector

The IBL Detector consists of a cylindrical layer formed by 14 staves, which are arranged around the new ATLAS beam-pipe and tilted by 14° to ensure complete coverage in ϕ and to coincide with the Lorentz angle[11] in the 2 T solenoidal magnetic field of the ATLAS experiment (Figure 3.11). The new ATLAS Be beam pipe (X/X$_0$≃0.003), designed considering the new

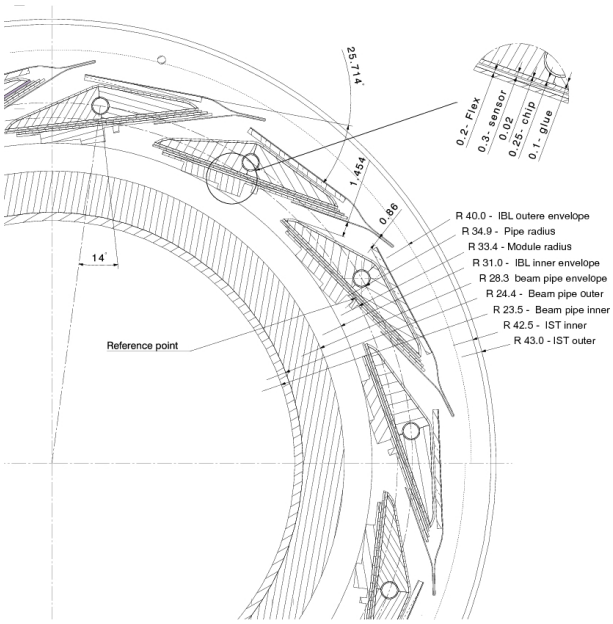

Figure 3.11: Cross section of the IBL layout in r ϕ view [25].

machine and physics requirements, has a radius of 23.5 mm allowing the insertion of a new layer to the pre-existing Pixel Detector. In this configuration the Pixel Detector becomes closer to the interaction point, moving from 50.5 mm to 32.7 mm. The clearance available between the beam-pipe and IBL is 9 mm, decreasing the distance to the interaction point. Staves and services are packed inside a 12 mm envelope along the 7 m IBL long structure. The main IBL layout parameters are summarized in Table 3.1.

3.3 IBL stave production and construction

The IBL Detector components were built, assembled and tested in several institutes. Two parallel starting workflows describe the processes: the production, construction and testing of IBL modules, and the production and quality control of mechanical parts (mainly carbon staves and flexes). Once all components have been qualified, they are shipped to an assembly point where the modules are loaded on bare staves and wing flex are connected to these modules.

[11] An electron or a hole moving in an electric field experiences, in the presence of a magnetic field B, the Lorentz force $\mathbf{F} = \pm e\,(\mathbf{E} + \mathbf{v} \times \mathbf{B})$ with the sign of the charge carrier under consideration. The drift direction will deviate from the direction of the electric field by the Lorentz angle θ_L.

Parameter	Value
Number of staves	14
Number of modules per stave (single/double FE-I4)	32/12
Pixel size (ϕ, z)	50, 250 μm
Module active size WxL (single/double FE-I4)	16.8$\times$20.4 / 40.8 mm^2
Coverage in η, no vertex spread	$\|\eta\| < 3$
Coverage in η, 2σ (=112 mm) vertex spread	$\|\eta\| < 2.58$
Active z extent	330.15 mm
Geometrical acceptance in z (min, max)	97.4, 98.8%
Stave tilt angle in ϕ	14°
Overlap in ϕ	1.82°
Center of the sensor radius	33.25 mm
Sensor thickness (planar silicon)	200 μm
Sensor thickness (3D silicon)	230$\pm$15 μm

Table 3.1: Main layout parameters of IBL Detector [25].

3.3.1 Single module qualification

One of the key steps in the IBL construction is the Quality Control (QC) of the IBL modules that have to be integrated on staves. The QC is essential to avoid the loading of a bad module or a module that could develop a failure during operation in the ATLAS experiment since at that point there will be no opportunity to repair or substitute any module. Sufficient information must be gathered to select the modules that are more likely to operate in ATLAS with acceptable efficiency and performance.

Several tests are performed at different stages of the assembly procedure:

- Preliminary electrical tests are executed just after the assembly to check if all wire bond connections have been done properly.
- Basic properties of the module are checked at room temperature. A preliminary module tuning is performed with a reference threshold of 3000 e$^-$ and 9 BCs ToT at 20000 e$^-$.
- The module undergoes a thermal stress procedure where ten temperature cycles between -40°C and +40°C are done. After that, the basic electrical tests done in the first step are executed again. A comparison between before and after thermal cycles is carries out.
- The module is completely calibrated, including an ^{241}Am source scan. The electrical tests are performed at about -10°C.

A ranking procedure and module selection has been settled referring on sensor properties, electrical performance and mechanical problems. Each of these categories is divided into specific issues to which a penalty score is related. A requirement of less than 1% of pixel defects per front-end has been established for the QC procedure.

Figure 3.12 shows the yield of IBL module production for sensor types (planar PPS, CNM, FBK) and per production batch groups. The module failures are divided into three main categories: “B.B. Fail.” stands for large bump-bonding failure, “Bare Fail.” stands for the module not assembled due to mainly mechanical damages and “Other Fails.” stands for both electrical

and sensor failures discovered after assembly. A large fraction of bad modules is present in batch L1 because of serious bump bonding issues (Section 3.2.3) and about 15 % of the modules have issues in a regulator on FE-I4 chips which are not tested before bump-bonding. Apart from bump-bond failure, the average qualification yield is 75% for the planar PPS, 63% for CNM and 62% for FBK.

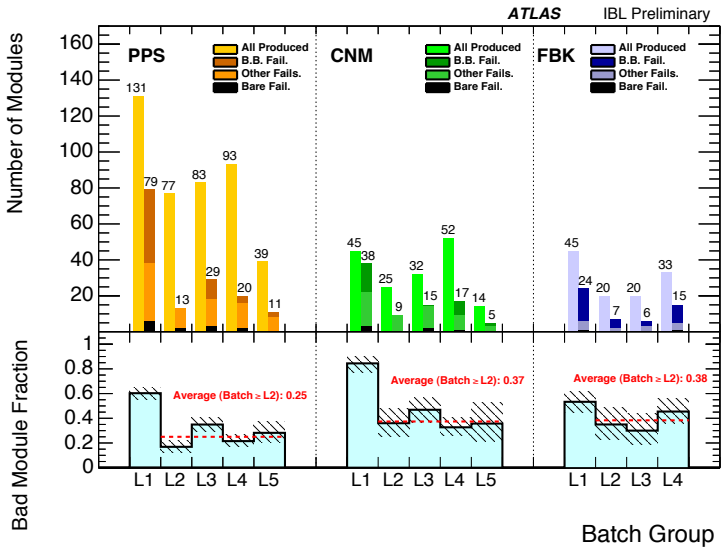

Figure 3.12: Yield of IBL module production divided for sensor types, planar (PPS) and 3D (CNM and FBK), and production batch group [36].

3.3.2 Stave assembly

The qualified IBL modules, bare staves and flexes are collected at the "stave assembly point". Basic functionality tests are performed to check for any possible damage occurred during transportation. Each bare stave goes through a metrology survey before and after ten thermal cycles to crosscheck that the IBL specification of 350 μm planarity is fulfilled.

After the quality checks of each component, the module loading procedure is executed following the steps summarized in Figure 3.13. The qualified bare stave is installed in the loading tool providing all required reference points (Figure 3.13(a)) and the flex tail of each IBL module is cut (Figure 3.13(b)). A 70 μm layer of thermal grease is deposited on the stave and modules are sequentially glued using a module spacers to guarantee a 250 μm gap between neighboring modules (Figure 3.13(c)). After loading all modules, the stave-flex wings are glued to the module flexes by means of clamps (Figure 3.13(d)) and a weight of about 20 g is positioned during the curing time. As final steps, wire-bonding between module flex and stave-wings is performed (Figure 3.13(e)) and a pull-test is done to verify its quality (Figure 3.13(f)).

The final IBL stave goes through a series of QC electrical tests to verify the functionality of each individual module. In the QC procedure, ten thermal cycles (between -40°C and +40°C) are expected for each IBL stave. However in this set-up the humidity cannot be fully controlled. After this observation no thermal cycles were done anymore. This decision was taken in the middle of the staves assembly and so the first 10 production staves were exposed to thermal cycles.

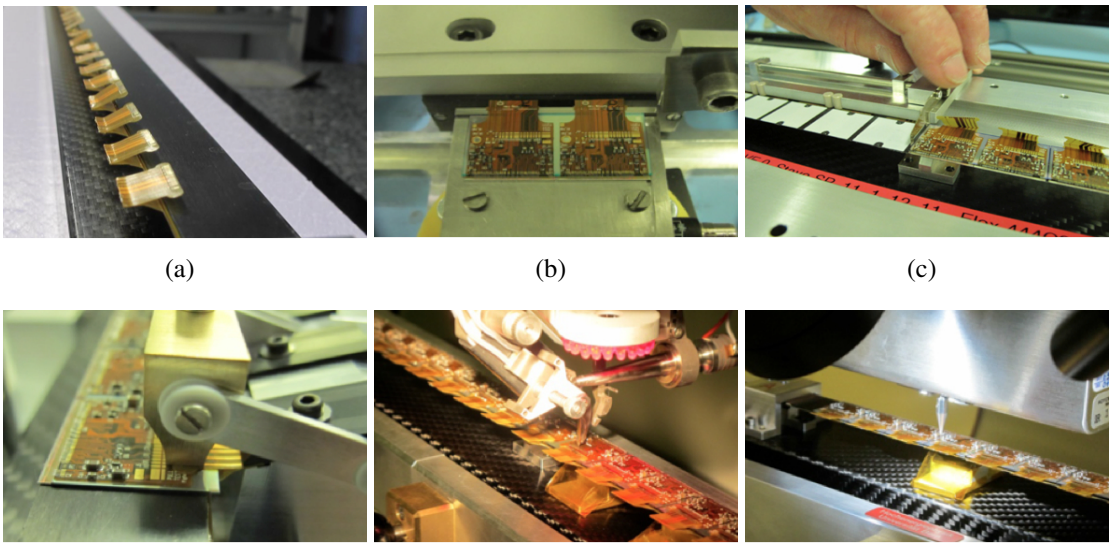

(a) (b) (c)

(d) (e) (f)

Figure 3.13: Sequence of module loading procedure for an IBL stave.

A total of 20 staves have been produced loading 400 modules. Fourteen staves out of the production have been assembled around the beam pipe to build the IBL detector, which has been installed in the ATLAS experiment in May 2014. In the next chapter, an overview of the stave quality assurance and selection will be discussed.

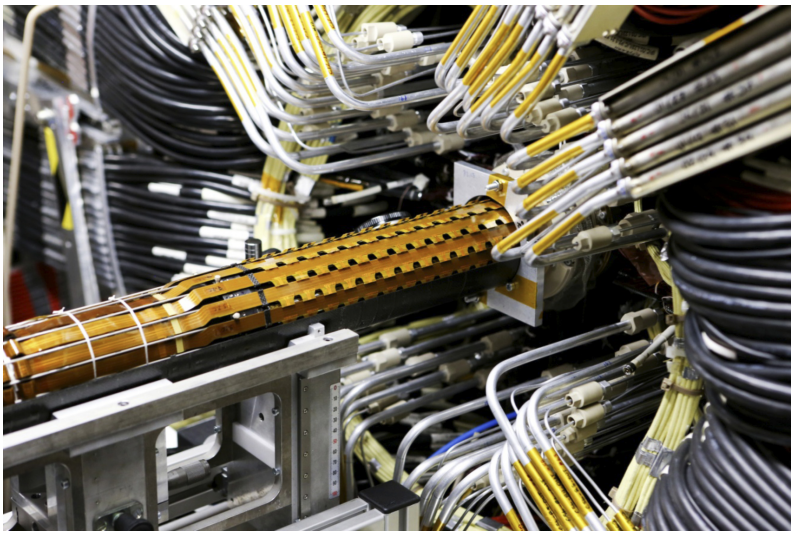

Figure 3.14: Insertion of the IBL detector in the ATLAS experiment.

Chapter 4

IBL staves quality assurance and reliability of detector components

Particle detectors at LHC are very complex apparatus and access for interventions is very difficult and limited after their installation. This is especially true for inner detectors, which are located in the center of the experiments, as it is the IBL case for which an exceptional reliability is demanded. The control of all construction processes from beginning to end is a very difficult task due to the complexity of the technologies and the spread of the activities in many universities and research centers. In these conditions, a robust Quality Assurance (QA) is necessary to guarantee the achievement of a good result. QA is a tool to prevent mistakes or defects during construction and to guarantee the quality requirements. Well defined testing protocols are established for achieving the necessary homogeneity in the selection of the best materials for the assembly of components and final detector. In parallel to the detector QA, the reliability of all single detector constituents has to be ensured for the final operation. In this respect, systematic studies have been conducted to understand the behavior of wire bonds in the ATLAS magnetic field and to prevent possible damages due to wire bond oscillations induced by alternating currents.

4.1 Quality assurance and performance of the IBL production staves

The QA of IBL staves [45] needs to be a reliable process allowing to select the best staves for integration into the ATLAS experiment. The outcome of the stave QA procedure provides a deeper understanding of the assembled detector. A total of 18 production staves are considered[1] for the IBL integration and included in the QA results. The global characterization of the staves allows to select the best 14 for the detector assembly.

The stave QA procedure has been developed for testing the IBL production staves in the more efficient and systematic way. Figure 4.1 shows the time flow necessary to perform the QA tests. The QA of each stave includes a detailed optical inspection, electrical functionality and

[1]Two staves out of the 20 produced were rejected a priori due to the very low quality of several modules caused by the occurrence of an accident. The performance of these two staves will be not discussed in this work.

reception tests, calibration in different environmental conditions, data taking with radioactive sources as well as a classification of pixel failures.

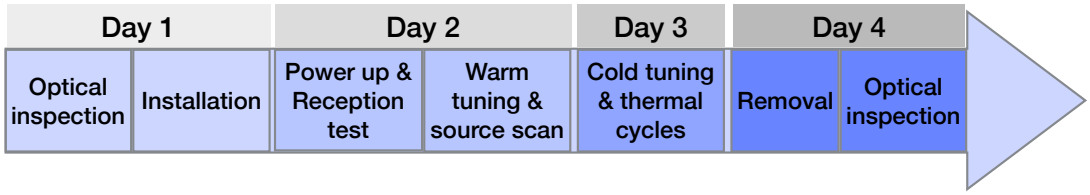

Figure 4.1: Time flow for the tests needed to qualify an IBL stave.

4.1.1 Experimental set-up

The QA set-up has been built at CERN for testing two staves simultaneously[2]. It uses as much as possible services and readout components of the final detector. Figure 4.2 shows a schematic view of the stave QA stand. Three main blocks can be identified: Detector Control System (DCS), Data Acquisition (DAQ) system and the environmental box hosting two staves.

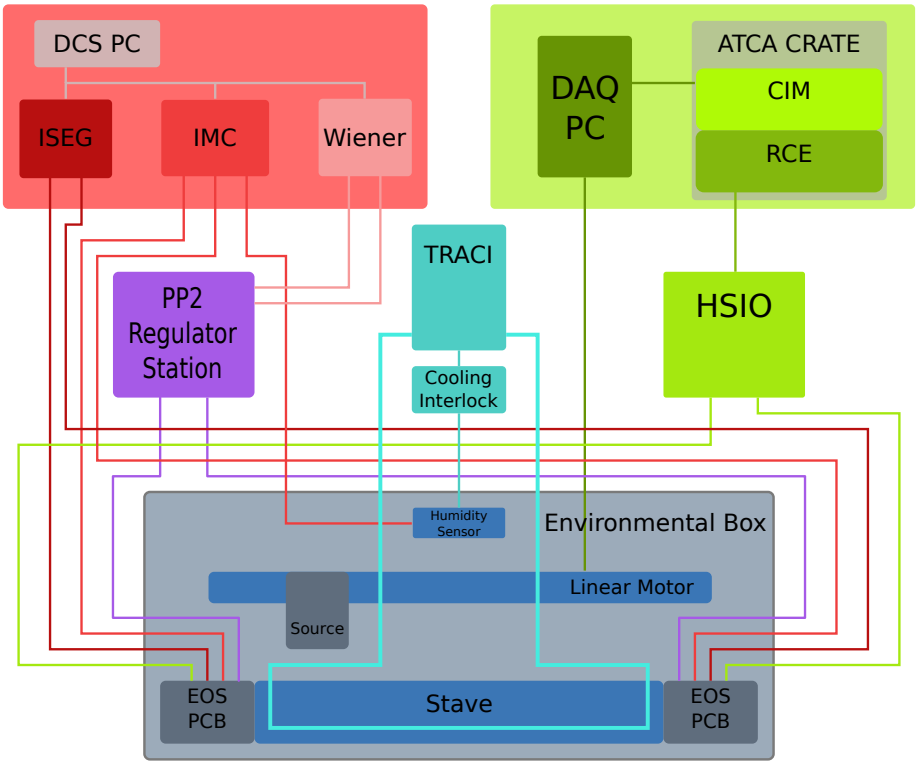

Figure 4.2: Schematic view of the IBL QA set-up. Three main blocks can be identified: Detector Control System (DCS) in red, Data Acquisition (DAQ) system in green and environmental box containing two staves (plus cooling system) in grey [45].

The environmental box, made of aluminum sheets covered inside with insulating foam, is flushed with dry air to keep the inside dew point below the temperatures of staves and cooling

[2]In the following, the two testing positions inside the set-up will be called SR and CR side.

pipes. The minimum dew point achieved during operation is -26°C. As additional safe-guard, the staves are kept in a smaller plastic box flushed with N_2 at both extremities. A linear motor, installed inside the box between the two staves, holds a mechanical support for two ^{90}Sr radioactive sources. The distance between the two sources corresponds to the distance between six front-end chips, meaning that two chips can be irradiated at the same time. Figure 4.3 shows an overview of the set-up where two connected staves and the mechanical support with two ^{90}Sr sources are visible.

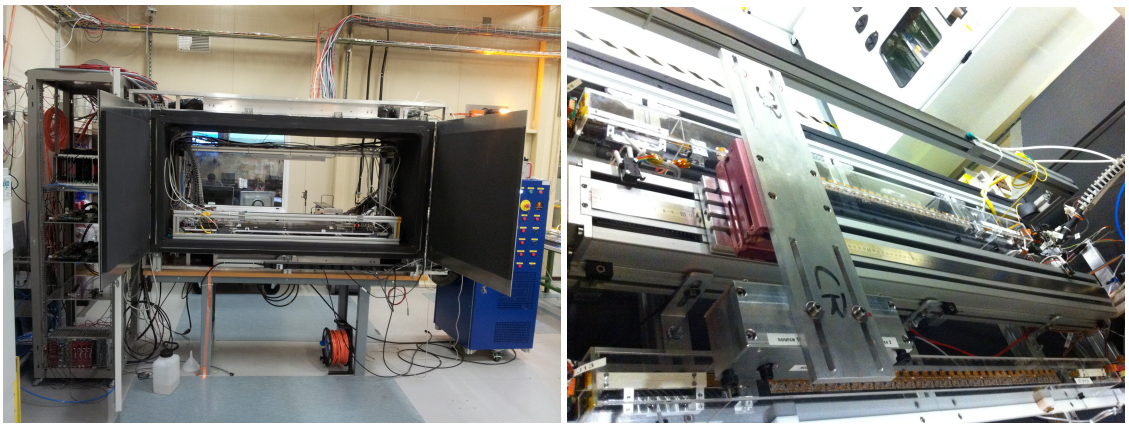

(a) (b)

Figure 4.3: Stave QA test stand pictures showing the (a) outside and (b) inside of the environmental box.

The cooling system uses CO_2 as main refrigerant as it is in the final IBL cooling system. The cooling plant, named TRACI (Transportable Refrigeration Apparatus for CO_2 Investigation) [46], uses a concept called 2PACL (2-Phase Accumulator Controlled Loop), which is a pumped 2-phase loop where the saturation temperature is controlled in an accumulator filled with liquid and vapor. The circulating CO_2 in the loop is condensed and sub cooled in a heat exchanger cooled by an external cold source and it is sent in parallel to two IBL staves via a dedicated circuit. The TRACI cooling power is 100 W allowing a temperature operation range from -40°C to 25°C. Each IBL stave dissipates about 30 W during normal operation. However, given the dimension of the environmental box, the heating dissipation cannot be neglected and the temperature operation range is restricted between -20°C and 25°C. The TRACI is also equipped with an interlock system for safe operation of staves: the cooling system cannot be switched on if the doors of the environmental box are open and in case of CO_2 temperature close to the dew point (within 10°C).

The DAQ system and the powering supply are connected to the stave through an End-Of-Stave (EOS) Printed Circuit Board (PCB). Unlike the DCS, the DAQ is not as the IBL final one but it consists of a new readout system based on a high speed, parallel and modular system based on Advanced Telecommunications Computing Architecture (ATCA) technology. The main hardware components are:

Reconfigurable Cluster Elements (RCE) It is the primary computational element responsible to send and receive data from the IBL front-end chips. Each RCE contains a Power-PC System-on-chip running the operating system. A single RCE board contains two RCEs,

each of which is interfaced with half stave. The RCE board communicated with the HSIO board via optical transmission.

High-Speed Input-Output (HSIO) board It is the intermediary step between the optical signals sent-out and received-by the RCE and the electrical signals sent-out and received-by the FE-I4s. Each HSIO serves one half stave and it is connected to two RCEs through separate fibers. The HSIO performs the buffering and multiplexing of the data sent to or coming from the chips as well as the 8b/10b decoding of the front end (FE) data. It is also responsible for generating and sending the clock signal to the FE and for formatting and sending cyclic and external triggers to the FE-I4B.

A dedicated DAQ software has been developed to interface with the front-end chips. The user interface is a ROOT-based GUI [47]. Each front-end chip can be singularly configured with the DAQ providing the final histograms and results. All tuning values can be set up individually in the GUI and a collection of scans can run automatically. The GUI accepts also command line as input allowing to run Unix scripts in between two scans. This feature is used to run the C++ software developed to operate the linear motor.

A schematic of module layout, mapping and powering modularity has been implemented to allow a easy identification of FE-I4 and powering group (Figure 4.4). The stave is divided into two main regions called “A side” and “C side”, each one having 6 planar and 4 3D modules for a total of 16 FE-I4 chips. Groups of four FE-I4 chips are powered in parallel (this represents a powering group for the DCS) and have a Negative Temperature Coefficient (NTC) sensor to monitor the modules temperature.

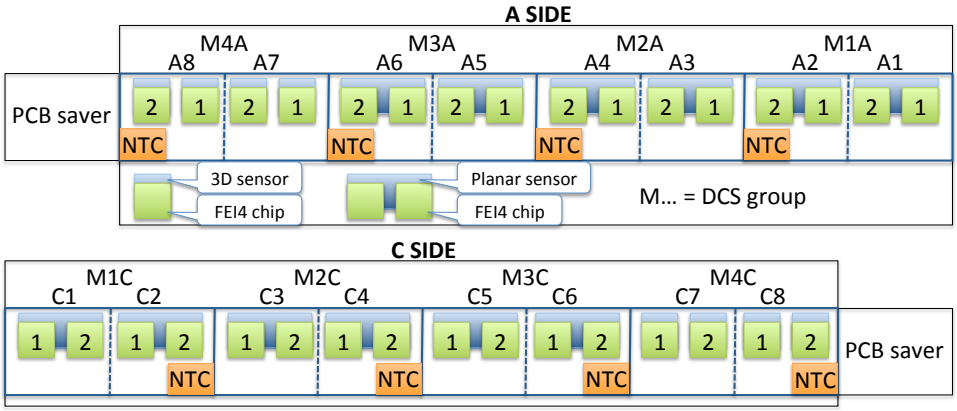

Figure 4.4: Schematic view of module layout, mapping and powering modularity for an IBL stave [45].

4.1.2 Optical Inspection

A detailed optical inspection is performed at the beginning and end of the QA procedure. High resolution pictures of each chip are taken to spot any major damage or eventual debris that might have been left on the stave during assembly or wire-bonding. These pictures can be compared by eye to the ones collected during the modules QC or stave assembly to identify the source of any problem.

After, the stave is inspected with an optical microscope: each wire bond and bond pad are carefully controlled. Irregularities are classified as following:

Misaligned module Two neighboring modules are not well aligned on the z-axis (Figure 4.5(a)). This problem comes from a bad alignment during the stave assembly and nothing can be done at the QA level.

Loose wire bond A wire bond is attached on the module in a place where it should not be. The wire bond can easily be removed by means of tweezers or Kapton tape.

Lifted wire bond A wire bond is detached on one foot. Usually multiple wire bonds are connected on each pad, so it is not a critical problem if one of them is disconnected.

Bent wire bond A wire bond is in contact with something and it gets bent (Figure 4.5(b)). The bent wire bonds are left as they are since their functionality is not affected by this type of damage.

Broken wire bond on HV ring Each HV-ring has three or four wire bonds to provide HV to the sensor[3]. It rarely happens that one of these wire bonds is pulled out. Given the redundancy, nothing is done in this case but for future modules it was decided to increase the number of wire bonds on the HV ring.

Residues Different types of debris can be found on module flex (usually hairs, dust, textile wires). Normally they are left on the module.

The outcome of the microscope inspection is recorded in a table where the number of problematic wire bonds are pointed out for the different regions of the modules. The optical inspection is repeated after the qualification tests.

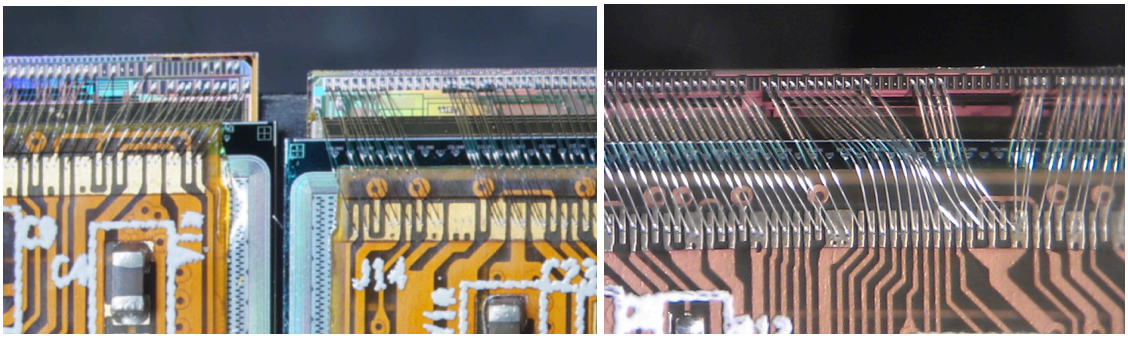

(a) (b)

Figure 4.5: (a) Example of misaligned module found in ST11 module C6. (b) Example of bent wire bonds on the FE-flex region in ST16, module C6-2.

[3]The number of wire bonds depends if the chip has been wire-bonded at universities of Genova or Bonn.

4.1.3 Electrical functionality

After the optical inspection, the stave is connected to cooling lines and electrical services (HV, NTC, DAQ, LV and sense lines of LV power regulators).

The electrical functionality tests are performed for front-end chips and sensors. The FE-I4 consumption before and after configuration is an important parameter for verifying the chip functionality during detector operation. The chips, grouped in one DCS group, are powered on-off between 0 V and 2.1 V ten times in about 400 s. In case of faulty modules, the current consumption varies significantly between cycles. The modules pass the test as long as the current is well below 2 A and above 0.8 A[4]. No major deviations from the standard operation are found except for some DCS groups where a large discrepancy from the standard unconfigured current values is known from the production sites.

An important step of the electrical functionality studies is to verify the behavior of current as a function of bias voltage (IV curves) for the sensors. The measurement of the breakdown voltage is a very powerful tool for sensor testing since almost all possible problems in the sensor production process lead to a deviation of the IV curve from the expected behavior. Also defects on the ohmic side or problem located on the p-side can be easily spotted with IV curves. For un-irradiated modules, the measured current can be dominated by surface effects until the bias voltage exceeds the breakdown voltage.

The power supply lines are grouped in one DCS group (Figure 4.4) meaning that it is possible to verify the IV curves only for grouped modules (four 3D modules or 2 planar modules). This can be considered as a limitation since the HV to be applied to a DCS group has to be the depletion voltage of the less performing sensor. In the QA procedure, the HV is increased in 20 steps from 0 V to 100 V for 3D sensors and from 0 V to 200 V for planar sensors since the breakdown voltage of 3D silicon sensors is very low in comparison to planar. A 20 μA current limit has been set for all IV measurements. The typical operation voltage is 20 V for 3D sensors and 80 V for planar sensors.

Figure 4.6 shows the IV characteristics of all powering groups divided by sensor type. The planar sensors deplete at about 50 V and most of them have a breakdown voltage above 200 V as well as very low leakage currents (below 5 μA). Only few DCS groups present breakdown voltages below 200 V and currents of the order of 10-20 μA that are by the way still inside the accepted QA region. The worst IV curve comes from the DCS group M1A of ST11, which has nevertheless been selected for the final IBL detector. The FBK sensors present a rather steep and consistent break down behavior with breakdown voltages between 30 V and 40 V, except for M4A of ST10 where it is below 20 V. On the contrary, 3D CNM sensors show a rather smooth break down behavior overall a large voltage range (0-100 V) with sometimes currents at around 20 μA already below 20 V. The lower FBK breakdown voltage with respect to CNM sensors is mainly due to the different full-through versus partial column designs. Furthermore the CNM ohmic behavior is probably due to the slim-edge being too close to the 3D guard-ring, which effectively connects the ohmic side to ground (Figure 3.7). This behavior is already observed at the production and assembly sites. Anyway, the sensors are fully depleted as verified by source scans and the currents are not extremely high at operational voltages, making these modules suitable for operation in the IBL detector.

[4]Usually the un-configured current is 1.1 A while the configured current is 1.5 A for each powering group.

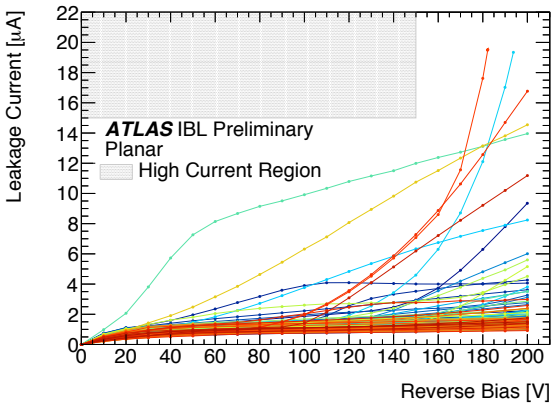

(a)

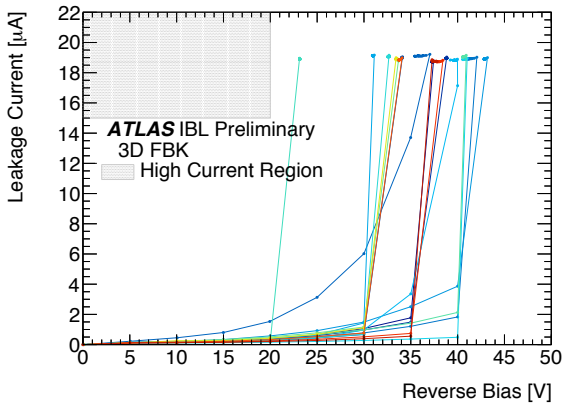

(b)

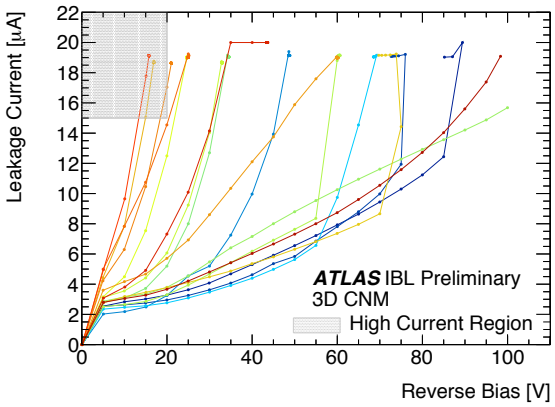

(c)

Figure 4.6: IV curves of 17 staves (stave 20 is excluded due to lack of data) for (a) planar, (b) FBK and (c) CNM sensors [45].

4.1.4 Functional tests

For each QA procedure step, several scans are executed for every single module at the pixel cell level. The scans are a series of test injection commands and read out. They can be divided as [48], [49]:

Digital scan It tests the digital part of the pixel cell injecting 50 pulses into each pixel bypassing the analog part. It can detect failures in the global and pixel registers that may affect the proper configuration of the module.

Analog scan It tests the analog part of the pixel cell injecting 50 pulses into each pixel.

Threshold scan It injects various defined charges into the analog pixel cell for 50 times. Every time that the injected charge is seen by the electronics, the event is counted as a hit. During the test both capacitors on the pixel are used. The efficiency method is applied: the number of collected hits versus the injected charge is recorded. Ideally a step function should appear while in practice a curve like the one shown in Figure 4.7(a) is reported since some injected charges are below the threshold while some others are not. The best way to describe this function is the error function, which is a convolution of the ideal step

function with the Gaussian pixel noise distribution:

$$f_{error}(x) = \frac{1}{\sqrt{2\pi}} \int_0^x e^{-t^2} dt \tag{4.1}$$

with $t = \frac{x-\mu}{\sigma}$. The threshold is defined to be the charge for which the hit efficiency is 50% while the noise σ of a pixel is inversely proportional to the steepness of the transition from no detected hits to full efficiency. The noise can be calculated, for example, between the 30% and 70% points of the error function as:

$$\sigma = \frac{Q_{70\%} - Q_{30\%}}{f_{error}^{-1}(70\%) - f_{error}^{-1}(30\%)} \tag{4.2}$$

where f_{error} is the error function normalized to 1 and Q is the injected charge.

ToT scan It injects repeatedly a fixed charge of 16000 e^- into each pixel. The Time over Threshold (ToT) is defined as the time in which signal is above threshold and it is proportional to the deposited charge, as it is visible in Figure 4.7(b). The ToT is measured in units of bunch crossings, i.e. 25 ns.

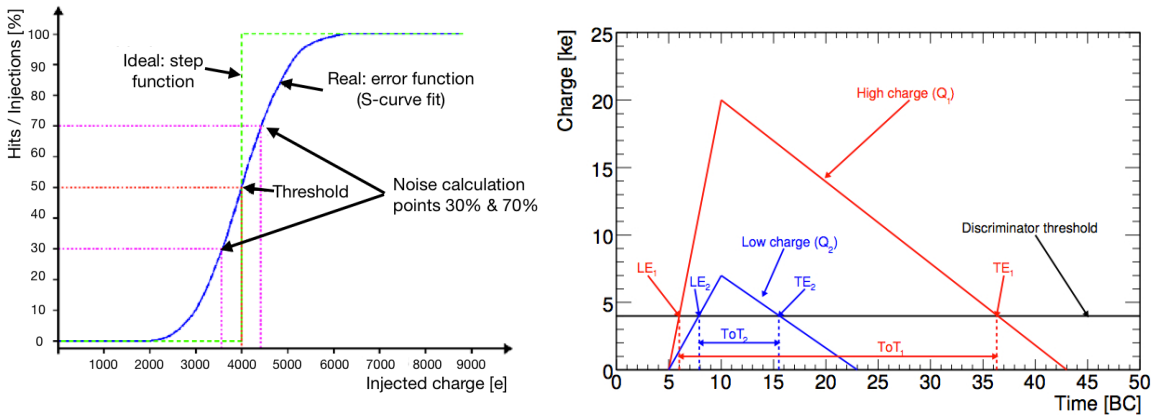

(a) (b)

Figure 4.7: (a) Schematics of an example of S-curve with the method to select the threshold and noise. (b) Overview of the ToT method to defined the charge [50].

Crosstalk scan It injects a high charge into the pixel in the row below and the row above a pixel and it enables the readout only for the pixel in between. The procedure is repeated for each pixel.

Noise scan It sends random triggers at a high rate (about 50 kHz depending on the DAQ system) to the configured chip and it records the number of hits for each pixel. The result is an upper limit of the noise hit probability for every pixel:

$$Noise\ Occupancy = \frac{Occupancy}{Sensitive\ time\ [BC]} \tag{4.3}$$

where the sensitive time in BCs is given by the number of triggers send to the module times the trigger multiplication mode set in the front-end.

Selftrigger scan The front-end are set into self trigger mode with the HitBus signal acting as an input to the command decoder for automatic triggering. During the scan, the chip is configured.

4.1.5 Reception tests

A set of scans is executed to get a preliminary overview of the stave functionality and as an indication of possible damages occurred during the transport. The measurements are taken at 22°C with the same configuration file used at the assembly point. Before starting reception tests, the trend of the sensor leakage current is monitored for about 10 min to ensure stability over time. A verification of the chip configurability is also performed.

Once the correct operation of the stave is verified, the following scans are performed: digital scan, analog scan, threshold scan, ToT scan, crosstalk scan and threshold scan with HV off. A specific focus is given to differences in number of digital or analog dead pixels to spot possible problems due to transportation. Figure 4.8(a) shows the results of the analog scan comparison for one stave. For each chip, the number of bad analog pixels are divided into two categories: pixels identified already bad at the assembly site and pixels that appear bad at the QA. Usually the number of analog bad pixels is of the order of 5 for chip at the assembly site. After the transportation a couple of more analog bad pixels is found. Considering the number of pixels for each chip (26880), such a small difference is negligible. Similar results are obtained for the digital scans. Only some modules have about 0.1% more digital or analog bad pixels that can just be attributed to statistical fluctuations.

A comparison of the threshold scans and its noise before and after transportation is also performed to verify the chips tuning and performance. An example of the difference in the threshold noise for each chip is shown in Figure 4.8(b). A higher noise on 3D modules on A side of the set-up is visible and it is due to the HV bias supply line serving the 3D modules on the CR A-side, which has a 0.2 V noise. In general, sensitivity to such external noise is observed for 3D modules, especially for FBK. Figure 4.9 shows the pixel by pixel threshold and noise for several production staves. Only a small shift in the per pixel threshold is observed and it can be explained by different operational environments of the two laboratory set-ups. The threshold noise shows a significant offset for some powering groups due to the noise on HV supply lines of the A side. Finally, a comparison of the threshold scan without HV is done to roughly check if a huge area of pixels have been disconnected since a pixel that is no longer connected to the sensor is not affected by the higher noise present when the sensor is not fully depleted. In general, no major differences in stave performance or bad pixels are found after the comparison.

4.1.6 Calibration

The calibration is a key phase of the QA since it allows to set the working point in terms of threshold and charge response as well as to have a uniform pixels response. Indeed, without calibration and tuning it would be impossible to distinguish between electronic noise and ionizing particle as well as to determine the amount of deposited charge in a pixel matrix. The

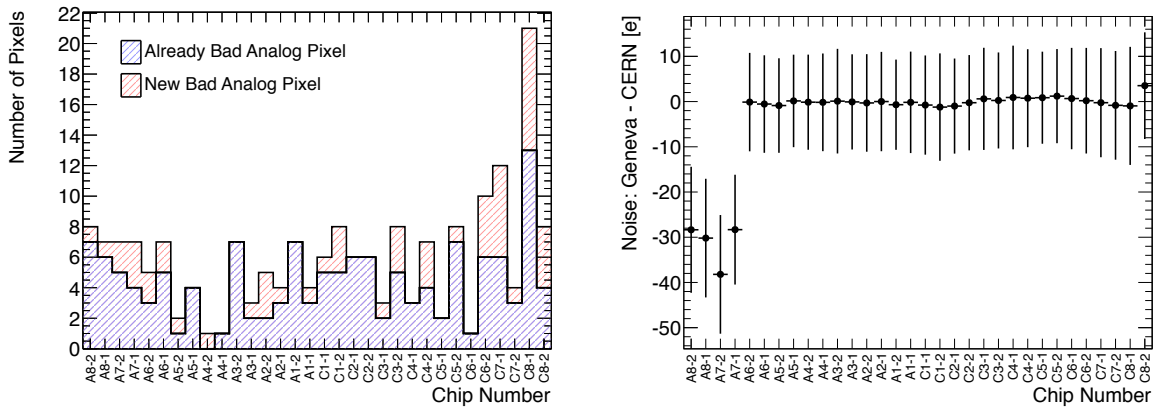

(a) (b)

Figure 4.8: (a) Number of pixels identified as bad analog at the assembly site and number of new bad pixels appeared at the QA set-up. (b) Difference in the noise value obtained with the same configuration file at the University of Geneva and CERN as a function of the chip number for ST18.

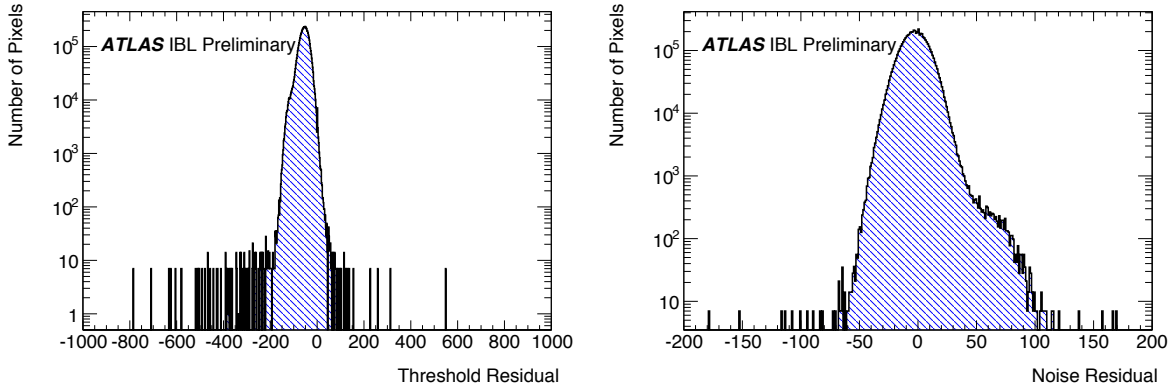

(a) (b)

Figure 4.9: Pixel by pixel (a) threshold and (b) noise residuals between the stave loading and stave QA sites. Only eight staves are used for this comparison [45].

calibration will have to be done many times during IBL lifetime to compensate for radiation damages. For example, the threshold will have to be lowered as the charge collection efficiency decreases with increasing radiation damage.

The calibration capabilities of IBL chips are tested at 22°C, which is the temperature at which most QA tests are performed, and at -12°C, which is the ATLAS Pixel Detector operating temperature. Furthermore the IBL staves are exposed to two thermal cycles between 22°C and -12°C to identify potential not well functioning modules. The module tuneability is tested for reference thresholds of 3000 e^- at 22°C (warm tuning) and 1500 e^- at -12°C (cold tuning). The ToT is tuned to 10 BC for a reference minimum ionizing particle (mip) charge of 16000 e^-.

Threshold and ToT tuning

The threshold setting is a trade-off between the need to have a high enough signal above the threshold and the need to have a low noise hit occupancy, crucial to avoid fake hits that degrade the performance of the pattern recognition algorithms. The threshold and feedback current are widely distributed over the pixel matrix due to process variations. Their tuning procedure is an iterative process of threshold and feedback current adjustments since both influence each other. Figure 4.10 shows an example of a threshold distribution of pixels before and after tuning where it is visible the large spread of the untuned chip while a tuned threshold distribution typically has a standard deviation of less than 100 e^-.

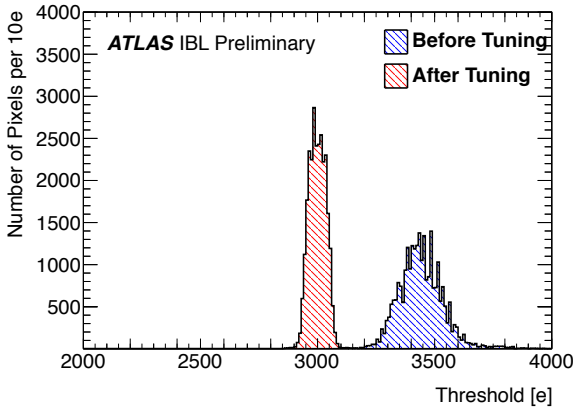

Figure 4.10: Threshold distribution of pixels before and after tuning for an IBL chip for 3000 e^- threshold tuning at 22°C powering group temperature [45].

The threshold can be tuned globally or individually for each pixel. The discriminator threshold for each pixel is controlled via two global 8 bit digital to analog converters (DACs) at the chip level allowing the shift of the threshold for all pixels at the same time. A 5 bit DAC at the pixel level is used for fine tuning of each pixel after the global DACs are tuned. Multiple charge injections are performed at the target threshold and the number of hits resulting from these injections are counted for a given set of global and pixel DAC settings. The global or pixel DAC is shifted until the optimal value achieves a hit efficiency closest to 50%.

The ToT tuning is done after the threshold tuning as the discriminator threshold affects the measured ToT along with the feedback current of the amplifier. Similar to the discriminator threshold, the preamplifier feedback current is controlled via a 8 bit global DAC for all pixels in a chip and a 4 bit DAC per pixel. The ToT mean value is calculated for a given set of global and pixel ToT DAC settings. The global or pixel DAC is shifted until the optimal value achieves the set ToT.

Threshold and ToT scans

After the threshold and ToT tuning, threshold and ToT scans are performed to verify that the tuning is correct. Figure 4.11 shows the threshold distribution of a FE-I4 chip after a successful tuning procedure. Most of the pixels are tuned to the target value of 3000 e^- (Figure 4.11(a)). Only one pixel (channel 8715 in Figure 4.11(b)) out of 26880 channels has a threshold of 1000 e^- demonstrating the very good tuning procedure and threshold tuneability of the chip.

The threshold scan provides also informations on the electronic noise (called Equivalent Noise Charge, ENC). A noise below the threshold dispersion level of 200 e^- is usually required. Figure 4.12 shows the noise distribution of the same chip. The mean value of the gaussian fit is

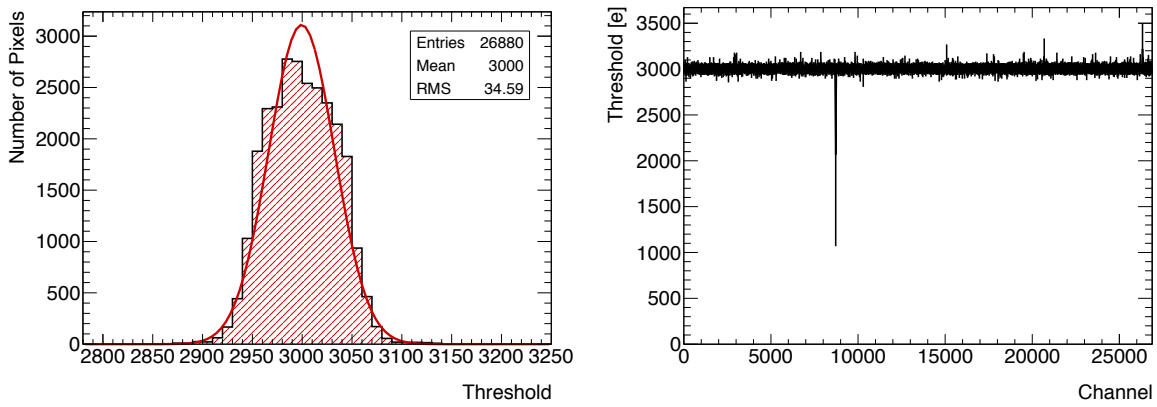

(a) (b)

Figure 4.11: Threshold distribution of a FE-I4 chip (A1-1- in ST18) after a successful tuning procedure for reference threshold of 3000 e^- at 22°C. (a) Fit of the threshold values and (b) threshold values as a function of pixel channels, where channel number is calculated as (row+col)×336.

around 130 e^-, which is a very good value for an un-irradiated module. Only few pixels have an ENC very different from the mean value (Figure 4.12(b)). It has to be noticed that the ENC is higher for the first and last channels, which correspond to the first and last chip columns where long planar pixels are present. In the case of 3D sensors, the external pixels do not have a higher noise since their size is equal to the size of internal pixels. However the 3D mean noise value is higher than for planar because of a larger pixel capacitance, which has been calculated to be (110±4) fF for planar pixel cell, (170±2) fF for CNM and (200±8) fF for FBK pixel cell [51].

Figure 4.13 shows the ToT distribution of the same FE-I4 chip. The majority of pixels gives a ToT response of 10 BC when a charge of 16000 e^- is injected and only some of them have a slightly different ToT as it is visible in Figure 4.13(a) (blue or red pixels). The gaussian fit mean value of the ToT distribution is 9.99 BC with a standard deviation of 0.11 BC, which corresponds to only 176 e^- (Figure 4.11(a)). Similar results are obtained for the tuning at -12 °C.

Results for tuning at warm and cold temperatures

The final results obtained for the calibration of 18 IBL production staves to the reference threshold of 3000 e^- at 22 °C and 1500 e^- at -12 °C are reported in Table 4.1. Both tunings are performed for a 10 BC ToT response at 16000 e^-. Planar long pixels are listed separately as they show a higher noise due to their larger pixel size. The standard deviation of the threshold is slightly higher for planar long pixels. The obtained values can be considered excellent remembering that the minimal dispersion value is 40 e^-, as dictated by the precision of the injection circuit [43].

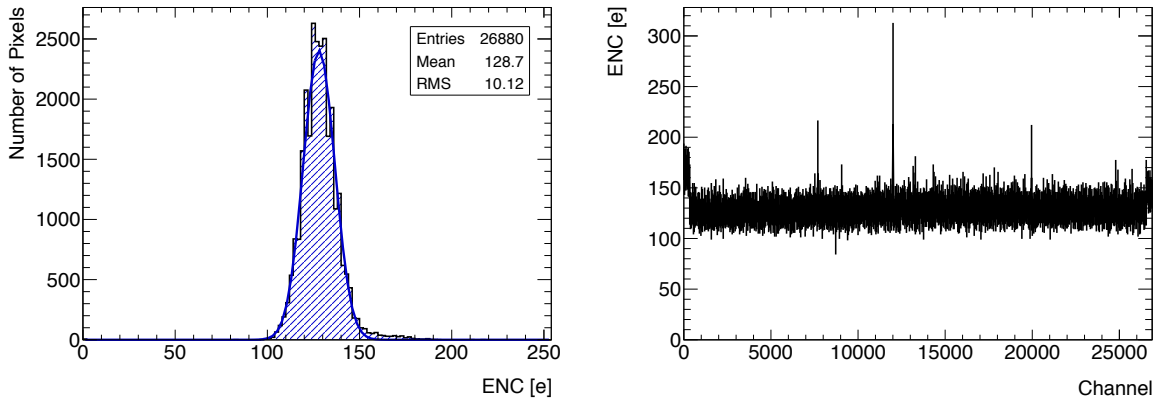

(a) (b)

Figure 4.12: Noise distribution of a planar module (A1-1- in ST18) after a successful tuning procedure for reference threshold of 3000 e^- at 22°C.

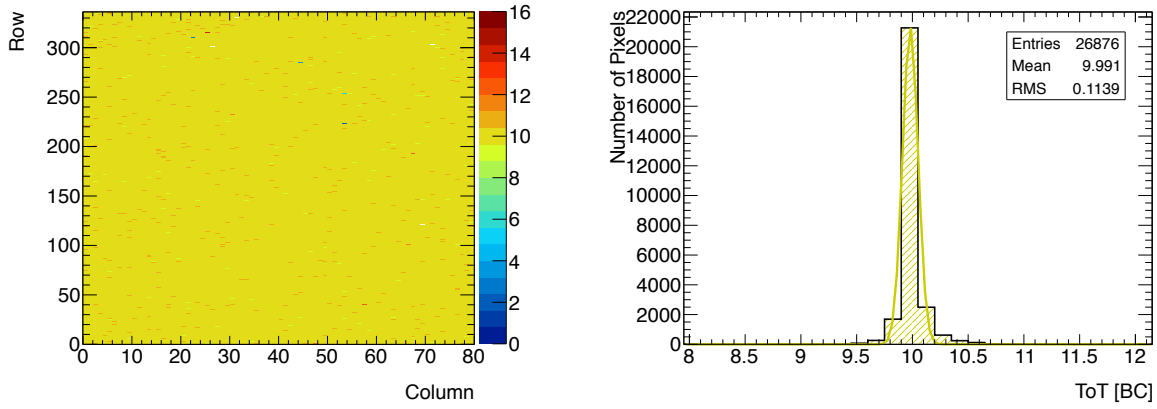

(a) (b)

Figure 4.13: ToT scan response to 16000 e^- injected for a FE-I4 chip (A1-1 in ST18) after a successful tuning procedure for reference threshold of 3000 e^- and ToT tuned to 10 BC for a reference mip charge of 16000 e^- at 22°C. (a) ToT scan 2D map for all FE-I4 channels and (b) fit of the ToT values.

The threshold and noise distributions of the different types of pixels have been investigated for all 18 production staves for both tunings. Figures 4.14 and 4.15 show the threshold and noise distributions obtained for the 18 production staves during the QA for the 3000 e^- threshold tuning at 22 °C and for the 1500 e^- threshold tuning at -12 °C, respectively. In both threshold distributions a bump of about 30 planar long pixels is present at a threshold of 1000 e^- and 500 e^- respectively, and some planar pixels have a threshold value away from the mean value. In particular, a pronounced peak is present around 2150 e^- for the 1500 e^- tuning that is not present in the 3000 e^- tuning: this peak is an artifact of one mask step in the threshold scan, where noisy pixels bias the s-curve. By re-doing the threshold scan and injecting in less pixels per mask step, the incorrect measurement can be avoided. Due to time constrains during the QA, having understood the feature and having obtained good results for the 3000 e^- tuning, it was decided to not re-do the tuning for these particular FE-I4 chips.

Tuned Threshold	Pixel Type	Std. Dev. [e^-]	Noise [e^-]	Threshold over Noise
3000 e^- at 22°C	Planar Normal	37	123 ± 10	25 ± 2
	Planar Long	58	146 ± 15	21 ± 2
	3D FBK	39	171 ± 25	18 ± 2
	3D CNM	40	149 ± 15	20 ± 2
1500 e^- at -12°C	Planar Normal	42	129 ± 13	12 ± 1
	Planar Long	47	149 ± 16	10 ± 1
	3D FBK	46	171 ± 25	9 ± 1
	3D CNM	41	146 ± 16	10 ± 1

Table 4.1: Threshold calibration summary for different pixel types for 18 staves. Listed values are the standard deviation of the threshold, mean noise and its standard deviation, and mean threshold over noise and its standard deviation [45].

The threshold noise distribution is similar for both tunings (Figure 4.14(b) and 4.15(b)). As already seen in Section 4.1.6, the 3D sensors have a higher noise than planar sensors. In particular, in the QA calibration a threshold noise of about 125 e^- is present for planar normal pixels while 3D FBK and 3D CNM pixels have a threshold noise of about 170 e^- and 150 e^-, respectively. A particular remark has to be done for the higher noise (around 300 e^-) of FBK pixels, which is primarily due to two modules located on staves 14 and 20 at the highest η position. These two staves were not chosen for IBL (as it will be discussed in Section 4.1.9)) and by taking into account only the 14 selected staves, the higher noise peak of FBK pixels disappears. Furthermore it has to be considered that ST14 and ST20 were tested on the CR-side of the QA set-up where a 0.2 V noise is present on the A-side (where primarily FBK are installed).

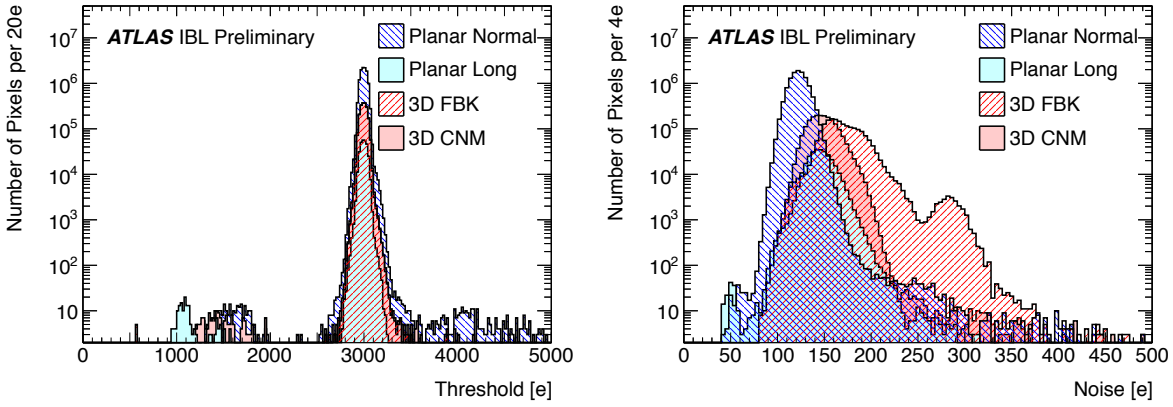

(a) (b)

Figure 4.14: (a) Threshold and (b) noise distributions after tuning all pixels to a target threshold of 3000 e^- at 22 °C module temperature for 18 production staves [45].

Figures 4.16(a) and 4.16(b) show the threshold and threshold noise distributions, respectively, for all 18 production staves as a function of chip number for the 1500 e^- threshold tuning at -12 °C. In general, it was possible to tune every chip to the desired threshold and the

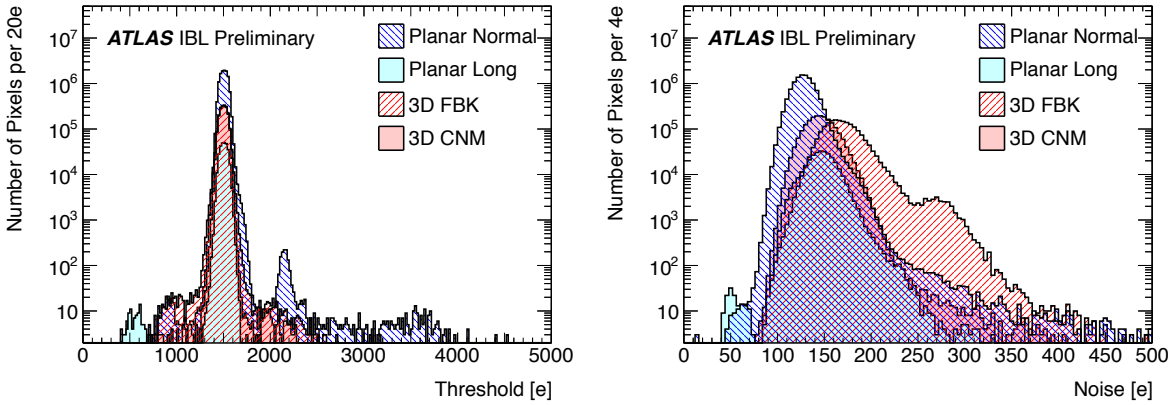

(a) (b)

Figure 4.15: (a) Threshold and (b) noise distributions after tuning all pixels to a target threshold of 1500 e^- at -12 °C module temperature for 18 production staves [45].

average threshold noise is below the expected values foreseen. As usual, an exception is the threshold noise for the 3D modules on the A Side of the set-up (mainly FBK but also CNM were tested on this side) due to a noisy HV line. However the noise for 3D sensor is set below 180 e^-.

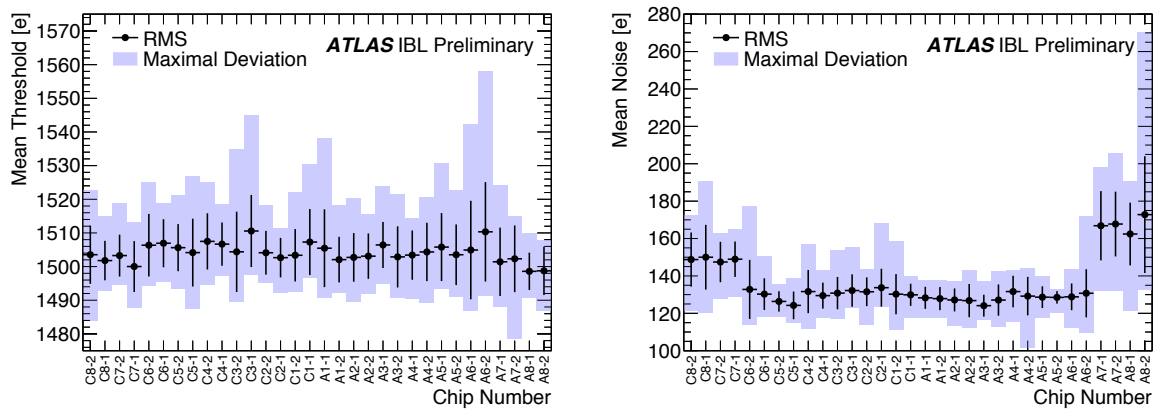

(a) (b)

Figure 4.16: Average (a) threshold and (b) threshold noise distributions for all 18 production staves as a function of chip number for the 1500 e^- threshold tuning at -12 °C. The plots show, for each chip position on the stave, the mean and scatter of the 18 data points (one from each stave). The error bars show the RMS spread, while the solid boxes show the minimum and maximum values [45].

The key parameter in the tuning is the threshold over noise, which determines the quality of the IBL modules with respect to their operability at a given discriminator setting. The bigger this factor is the less contamination of noise hits in the sample of physics hits will be recorded during collisions. Figures 4.17(a) and 4.17(b) show the threshold over noise distributions of pixels for 3000 e^- and 1500 e^- tunings respectively. Considering that the physics occupancy in the ATLAS Pixel B-layer was about 5×10^{-4} hits per pixel per BC at the end of Run1, an expected physics occupancy of 10^{-3} hits per pixel per BC is expected for IBL in early operation.

A threshold over noise value higher than 5 would ensure that the noise contamination in physics hits from IBL would be less than 0.1%. The threshold over noise distribution is a bit higher for planar sensors than for 3D sensors, especially the planar normal sensors have the highest value (25 ± 2 for the 3000 e^- tuning). The FBK distribution presents a small peak around 10, which is due, as for the noise distributions in Figure 4.14(b), to two modules located on staves 14 and 20 and it disappears taking into account only the selected 14 staves. One can notice that the threshold over noise value is reduced to half from the 3000 e^- to the 1500 e^- tuning for all types of sensor. The fraction of noisy IBL pixels is less than 0.03% for the 1500 e^- tuning, a factor two less than that for the current Pixel Detector.

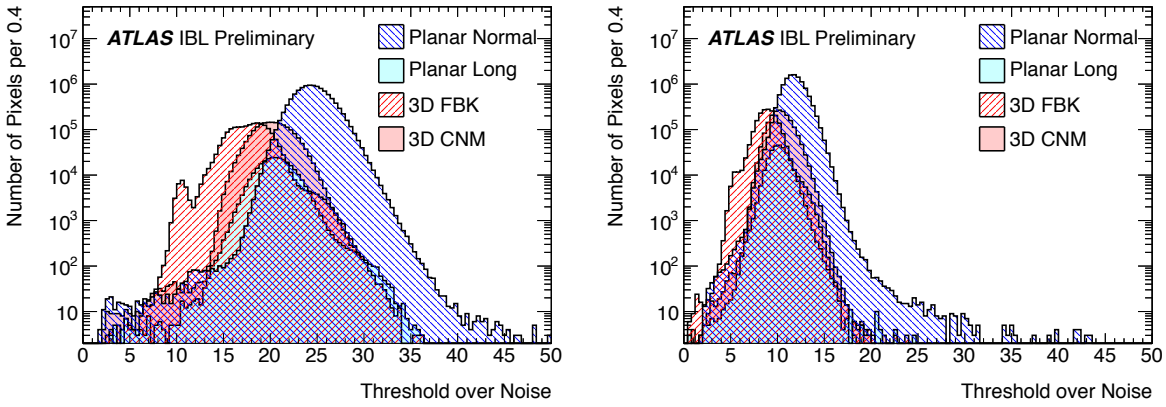

(a) (b)

Figure 4.17: Threshold over noise distribution of pixels for (a) 3000 e^- and (b) 1500 e^- tunings respectively [45].

The last calibration parameter to check is the ToT. Figure 4.18 shows the ToT distribution averaged over all 18 production staves as a function of chip number for the 1500 e^- threshold tuning at -12 °C. The average ToT value is distributed around 10 BC for all FE-I4 chips with a mean dispersion of 0.2 BC. Only two chip positions (A2-2 and A6-2) present a larger deviation from the mean value that can be attributed to two chips of two different staves.

A further investigation on the noise of 3D sensors have been performed, especially taking into account their testing position in the QA set-up since their noise can be affected by external sources. Figure 4.19(a) and 4.19(b) show the noise distributions of FBK and CNM pixels for the different HV bias lines in the QA set-up. Both types of sensor present a sensitivity to the noisy HV line (CR-A Side) with a more pronounced effect for FBK sensors. If the 3D FBK pixels in the CR-A Side are excluded, the FBK mean noise is reduced to 160 e^-. No difference in noise is observed for the planar pixels when biased with this noisy HV line.

4.1.7 Source scans

The module performance, including the verification of the tuning and the analysis of charge collection in the sensor, can be studied through the detector response to radiation. This can be done using cosmic ray particles or radioactive sources. The rate of cosmic hits is about 6×10^{-7} hits per pixel per second, which is too low for achieving good statistics during the limited time available for the QA. The use of radioactive source is therefore compulsory.

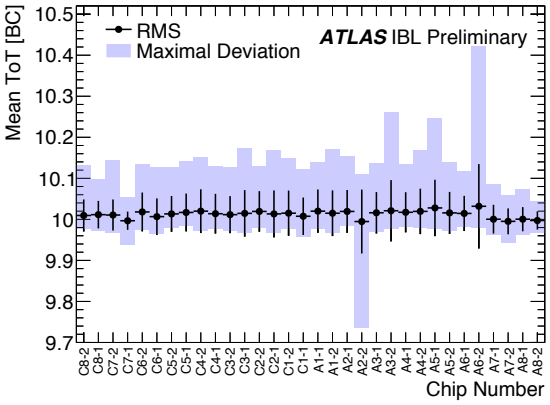

Figure 4.18: Average ToT distribution as a function of chip number for all 18 production staves. The pixels were tuned to 1500 e^- target threshold and to a 10 ToT target response for 16000 e^- at -12 °C [45].

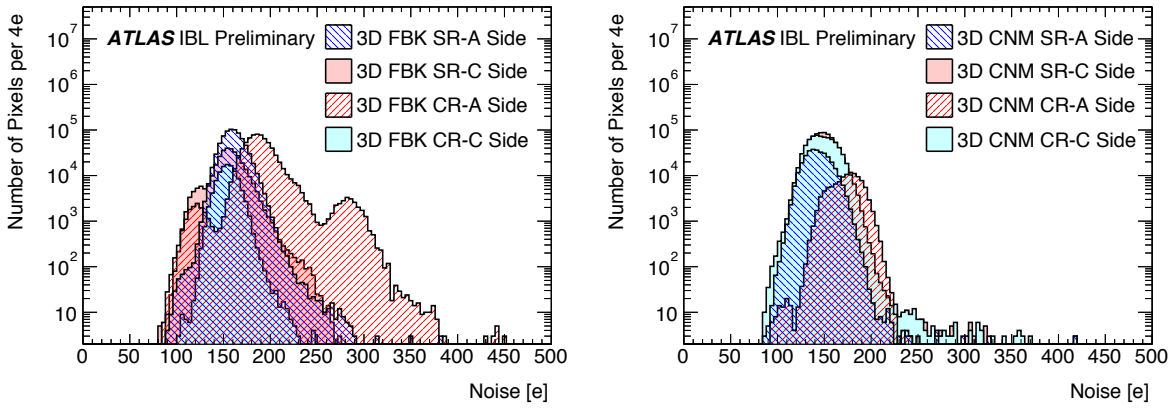

(a) (b)

Figure 4.19: Threshold noise distribution of (a) FBK and (b) CNM pixels for different HV bias lines in the QA set-up [45].

In the QA set-up two ^{90}Sr radioactive sources of 28.8 MBq each are available. They are collimated sources and they are positioned at a distance of about 10 cm from the modules to obtain an uniform irradiation of the module. ^{90}Sr decays via ^{90}Y into ^{90}Zr under emission of electrons with end-point energies of 546 keV and 2.28 MeV. The higher-energy electrons can be considered as minimum ionizing particles (mips) while the lower-energy electrons will deposit more charge than a mip. The charge deposited by mip electrons is expected to be about 18 ke$^-$ in silicon. Source scans can be performed using an external trigger or in selftrigger mode. The use of selftrigger is needed in case of γ-source while an external trigger is preferable for β-source to select only electrons simulating mip.

In the QA procedure, ^{90}Sr source scans are performed at 22°C with a 3000 e^- threshold and 10 BCs ToT at 16000 e^- tuning using the selftrigger mode. The two ^{90}Sr sources are fixed on the mechanical support of the linear motor and they are moved along the stave in 18 steps: in each step, the ^{90}Sr source is over one chip and data are collected for 400 s to have enough statistics.

Source scan occupancy

Figure 4.20 shows an example of a source scan hit map for a planar module. The occupancy distribution is uniform with about 150 to 200 hits per pixel. The regions with a lower number of hits match precisely the areas where Surface Mounting Device (SMD) components are mounted on the module flex PCB (Figure 3.9). The pixels in the external columns have a larger number of hits than the mean value, as expected given their size (Section 3.2.2).

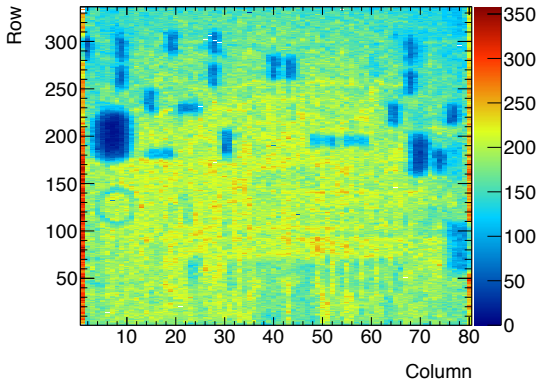

Figure 4.20: Source scan occupancy plot for a planar sensor on ST12 irradiated with ^{90}Sr at 22°C with a 3000 e$^-$ threshold and 10 BCs ToT at 16000 e$^-$ tuning.

Even if 3D pixel cells have all the same size, FBK modules have an higher occupancy in the external rows and columns. Figures 4.21(a) and 4.21(b) show the occupancy projection on the columns and rows for a FBK module. The number of entries is not uniform distributed because of SMD components, however it is visible a higher number of entries in external columns and rows with respect to the internal ones. This is the result of the chosen slim edge fence design of FBK (Figure 3.7(a)): the electric field does not reach the cut region but the charge collection efficiency extends beyond the active area giving a higher occupancy for the external pixels [40]. The occupancy for external rows is higher than the columns because the charge collecting area outside the active area is larger due to the difference pixel cell sides (250 μm $\times$ 50 μm).

In the CNM sensor design, a special "3D guard-ring" made of both junction and ohmic columns is present (Figure 3.6). This guard ring drains any parasitic current coming from the edge out of the pixels not allowing to collect the charge. In this case the occupancy for external pixel cells is the same of the internal pixel cells.

The discrepancy in the number of hits recorded for the different pixel cell categories has been quantified analyzing the ^{90}Sr occupancy distribution for all planar and 3D pixel cells of the 18 production staves. Figure 4.22 shows the number of hits acquired for each pixel during the source scans. The planar pixel cells have been divided into "normal" and "long". The mean number of hits is 162$\pm$41 for the planar normal pixels and 240$\pm$64 for the long pixels. Their ratio is 1.5$\pm$0.3 as expected since a long pixel has nearly double the length of normal pixel. For the 3D sensors, the defined categories are "normal 3D" for all 3D pixel cells except the external columns and rows that are divided into three categories for FBK and CNM sensors. The mean occupancy of the FBK pixels in the outermost columns and rows is increased by 1.1$\pm$0.3 and 1.6$\pm$0.3, respectively. These values can be translated in an increase of the active area of 20% for the external columns and 100% for the external rows. The 3D CNM external pixel cells have a

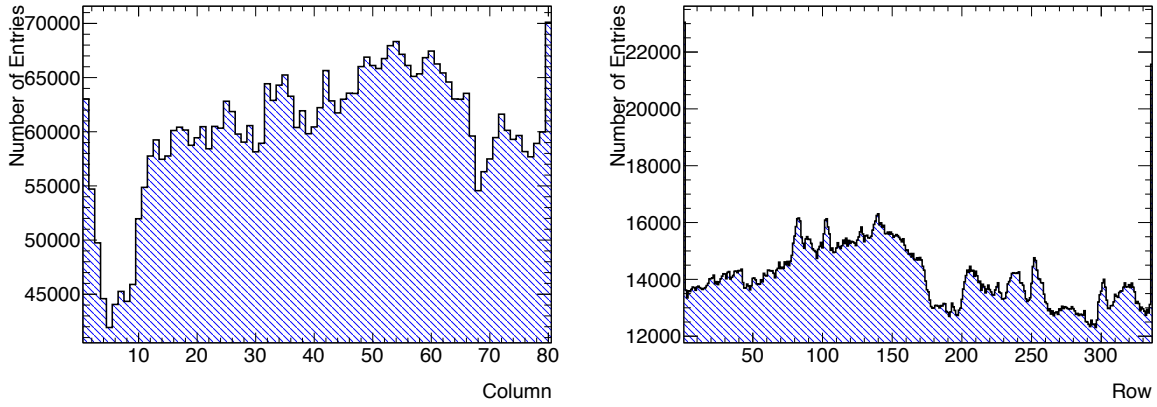

(a) (b)

Figure 4.21: (a) Projection of the occupancy plot on the columns and (b) projection of the occupancy plot on the rows for a FBK sensor on ST11 irradiated with ^{90}Sr at 22°C with a 3000 e^- threshold and 10 BCs ToT at 16000 e^- tuning. The number of entries is not uniform distributed because of SMD components, however it is visible a higher number of entries in both external columns and rows.

mean value of 163.5±42.5, which is very similar to the "normal 3D" mean value of 175.0±44.3. In this case the difference is considered only due to statistic fluctuations. A difference of about 10 in the distribution mean value is also present between the "planar normal" and "normal 3D".

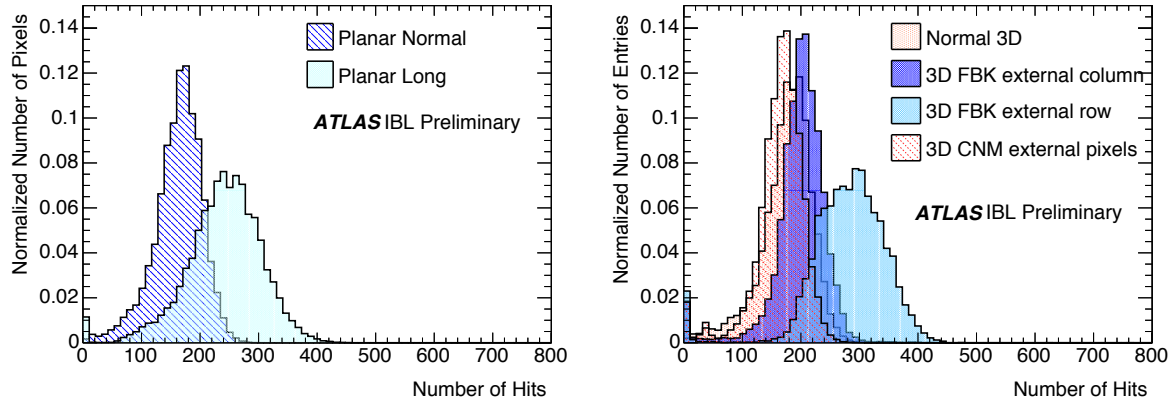

(a) (b)

Figure 4.22: Occupancy distribution for (a) planar and (b) 3D pixel cells in ^{90}Sr source scans [45].

Charge collection

The charge collection in a silicon sensor is measured through the ToT. A ToT of about 10-11 BCs is expected for the ^{90}Sr source scans since the tuning has been performed at 10 BCs ToT at 16000 e^-. Figure 4.23(a) shows the distribution of the ToT for a module. A peak is obtained at 4 BC, which is significantly below the expectation. This result can be explained

looking at the number of hits per each event (Figure 4.23(b)). Excluding the events with zero hits due to empty self-triggers, more than half of the total number of events has two or more hits, which in most cases are due to a particle that, passing through the sensor, deposits a charge in two or more pixels forming a cluster[5].

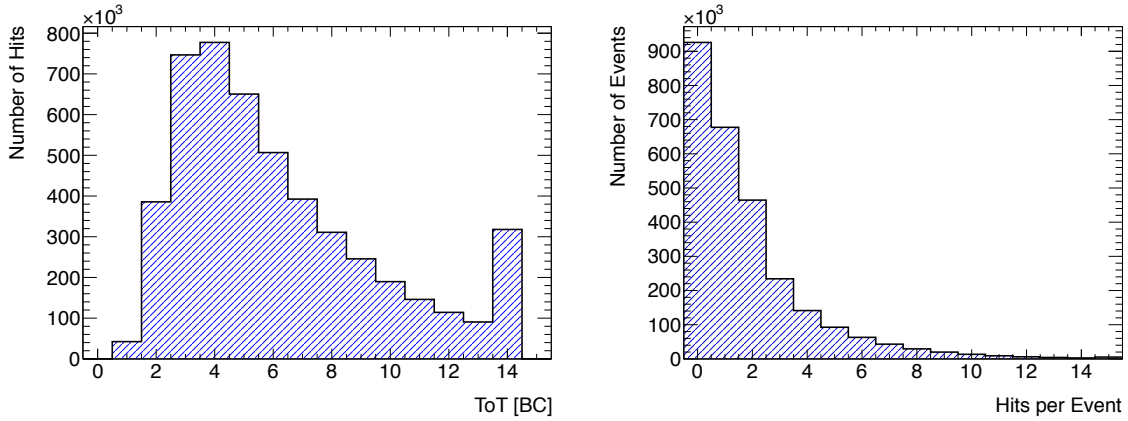

(a) (b)

Figure 4.23: (a) ToT distribution of the pixel cells in a ^{90}Sr irradiated chip. 1 BC ToT corresponds to a deposited charge of about 1600 e^- (considering a good calibration) and 14 BC ToT is the overflow value of the chip. (b) Distribution of the number of hits per event. The events with 0 hits are due to fake events caused by the selftrigger mode.

Figure 4.24(a) shows the cluster ToT where the energy deposited is calculated just summing the ToT value of each fired pixel. The distribution of the single hit clusters has a maximum at 2 BC ToT, which disappears when taking into account only clusters with two hits and more. This feature is caused by the use of selftrigger and by β particles energy. Indeed, the selftrigger cannot be used to select events and therefore every hit is recorded including the noise, which manifests itself in single pixel hits equally distributed on the module. Single pixel hits can also be caused by a partially electrons charge deposit or by low-energy electrons, which cause a longer tail of the measured signal distribution. Another possible explanation for the presence of low energy entries is charge sharing: pixels which are not directly hit but see a small amount of induced charge cause low energy entries in the histogram and lead to clusters of two or more pixels. The distribution of clusters with more than one hit is used in the QA analysis to exclude completely the noise and partially charge deposition contributions to the energy spectrum. In this way also the single hit clusters caused by a real charge deposit of electrons are rejected. However, given the QA purpose of source scans, the error is negligible. The distribution of clusters ToT with more than one hit is fitted with a Landau distribution convolved with a Gaussian.

The most probable cluster ToT value obtained from the Landau-Gaussian fit has been plotted for planar and 3D sensors (Figure 4.25(a)). The 3D cluster ToT value of the distribution peak maximum is slightly higher than for planar sensor. This shift is related to the difference in the sensor thickness (200 μm for planar and 230 μm for 3D). Nevertheless this feature cannot be observed for a single pixel since the ToT resolution is of 1 BC. The most probable cluster

[5]A cluster is defined as adjacent hits in the same trigger time.

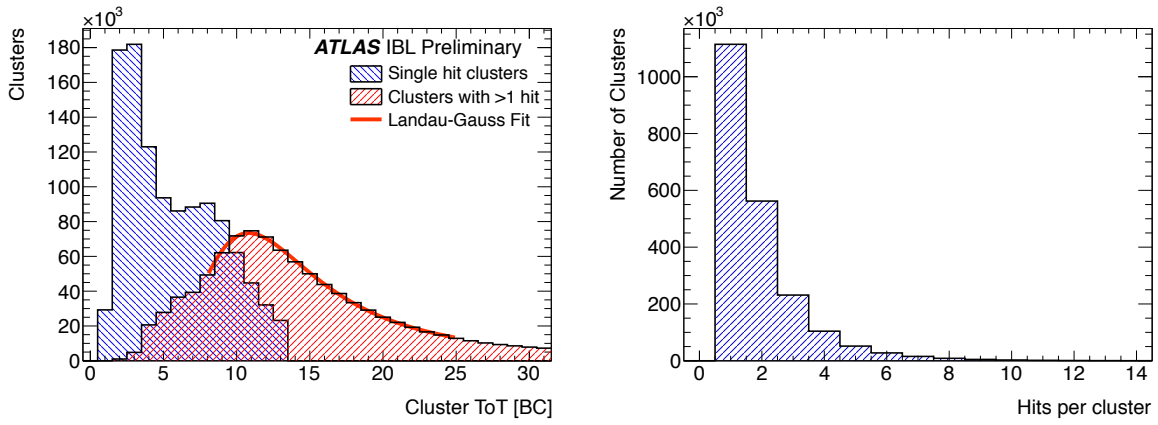

(a) (b)

Figure 4.24: (a) Clustered ToT for single hit clusters and for clusters with more than one hit. (b) Distribution of the number of hits per cluster.

ToT value has been plotted also as a function of chip position (Figure 4.25(b)) and no major differences are observed. The mean most probable ToT value is 10.5±0.3 BC, which is consistent with the given tuning of 10 ToT BC for 16000 e^- charge.

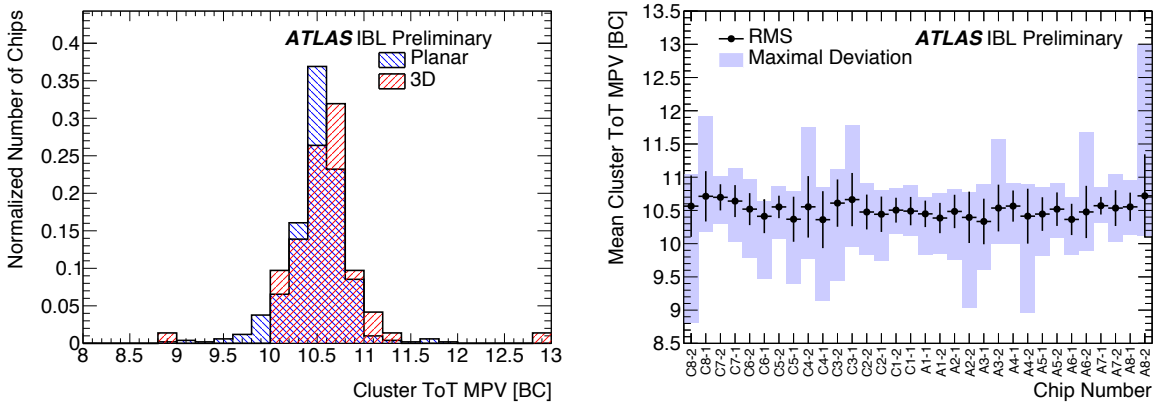

(a) (b)

Figure 4.25: (a) Distribution over all chips and (b) average as a function of chip number for the most probable cluster ToT value obtained from a Landau-Gaussian fit [45].

The fit results are used to compare the relative charge calibration of the chips to each other while an analysis of the absolute charge calibration is not possible with this method. Furthermore, as it will be discussed in the next section, source scans are also used to identify disconnected bumps thanks to occupancy plots.

4.1.8 Pixel defects

IBL modules can present several types of pixel defects, which are categorized into three main classes: defects pertaining to front-end, sensor or bump-bonding. A combined analysis of calibrations and source scans allows the classification of failing pixels into several sub-categories, listed below:

Digital and Analog Dead and Bad Pixels The quality of the digital and analog front-end cells is checked through digital and analog scans. Two different cases of not-well responding pixel cell can occur: digital and analog dead pixels, which are common electronics failures with an occupancy less than 1% of the injections, and digital and analog bad categories, which appear in case of a low ohmic connection between pixels and they are identified having an occupancy less than 98% or more than 102% of the injections.

Tuning Failed The fit of the s-curve can fail in case of a bad response from the injection circuit. In this case, the tuning fails and the pixel cell is considered bad. If the ToT response is 0 or 14 BCs (overflow value of the chip), the pixel is classified as untunable. In the QA tuning failed classification, a high discrepancy from the tuning target is allowed since even the pixels that cannot be completely tuned can still be used for operation despite just to a limited extend.

Noisy Pixel A noise scan is performed to measure the noise hit probability per bunch crossing for each pixel. The noise occupancy is a very important quantity for operation since pixels with high noise hit rate decrease the tracking performance. A pixel is masked during operation and classified as a noisy pixel for the QA procedure if the noise occupancy exceeds 10^{-6} hits per BC (the expected physics occupancy rate for IBL is about 10^{-3} hits per pixel per BC in early operation).

Disconnected Bump The bump bond connections of the sensor to the front-end are rather sensitive to mechanical stress and it is crucial to verify their integrity during all steps of the production and QA. Several types of scans can be used to identify a disconnected bump. The method used during the QA is to analyze the response from a source scan: if a so-far good pixel shows no hits or an occupancy less than 1% of the mean occupancy value, the bump is assumed to be disconnected.

Merged Bump A second type of connection damage is the merging of bumps. Merged bumps still form a connection between sensor and FE, but two or more channels are merged to a single connection decreasing the granularity in that part of the detector. This can happen with non-uniform mechanical pressure during flip-chip process, module handling or detector assembly. Several methods can be used to identify this type of defect, all based on the fact that in a merged bump the charge does not pass through one pixel when it has been injected but it goes also in a neighboring pixel, which results noisier since it sees more sensitive area. In the QA procedure a merged bump is identified with an analog failing pixel, which still gives a response in a crosstalk scan. Another method to identify this connection damage is using source scans: a pixel shows no hits while the neighboring has an occupancy that is almost twice with respect to the mean occupancy value.

High Crosstalk Ideally each pixel is an independent detector: whether current from the pixel or charge in the pixel is measured, the electrical content and activity in one pixel does not affect its neighbors (or any other pixels across the detector) and vice versa. In a real detector, this is not the case since electrical signals can couple to another through direct means, such as charge spilling from one pixel to its neighbor, or indirectly through capacitance or inductance (as for example too large bumps, small separation between sensor and FE

electronics, pouring of glue in the sensor-FE interstitial region, etc.). This phenomena is called "crosstalk" and it can lead to an increased fraction of double and triple hits, which may have to be taken into account in the position reconstruction algorithms. In the QA procedure, a pixel is considered having a high crosstalk when it records a signal with an injection of 25 ke$^-$ in the neighboring pixel cells.

Table 4.2 summarizes the pixel failures and the scans needed for their identification. The QA pixel failure classification is exclusive, meaning that only one category of failure is used per pixel in the order listed in Table 4.2.

Failure Name	Scan Type	Criteria
Digital Dead	Digital Scan	Occupancy $< 1\%$ of injections
Digital Bad	Digital Scan	Occupancy $< 98\%$ or $> 102\%$ of injections
Merged Bump	Analog Scan	Occupancy $< 98\%$ or $> 102\%$ of injections
	Crosstalk Scan	Occupancy $> 80\%$ of 25 ke$^-$ injections
Analog Dead	Analog Scan	Occupancy $< 1\%$ of injections
Analog Bad	Analog Scan	Occupancy $< 98\%$ or $> 102\%$ of injections
Tuning Failed	Threshold Scan	s-curve fit failed
	ToT Test	ToT response is 0 or 14 BCs
Noisy	Noise Scan	Occupancy $> 10^{-6}$ hits per BC
Disconnected Bump	Source Scan (^{90}Sr)	Occupancy $< 1\%$ of mean Occupancy
High Crosstalk	Crosstalk Scan	Occupancy > 0 with 25 ke$^-$ injection

Table 4.2: Classification of pixel failures for the QA procedure [45].

The classification and amount of pixel defects is crucial for the qualification of IBL staves. During the staves integration it is important to consider where the pixel defects are distributed along a stave and in which quantity. For these reasons, a complete study on pixel defects has been performed for all production staves with the final goal of using the pixel defects as one of the criteria for the stave selection.

Analysis of pixel defects at the module level

The QA analysis for pixel defects have been performed individually for each module and then for each stave. The number of bad pixels per chip is shown in Figure 4.26. The IBL target required was to have less than 0.37% pixel defects for each chip. Some chips have a larger number of bad pixels since the IBL constraint was shifted to higher value at the end of the production due to a shortness of modules. Nevertheless 73% of all chips on 18 staves have less than 0.1% of bad pixels.

An interesting study, which can be useful also for better optimization of future module production, is related to possible correlations between pixel defects and their location on the chip. In this case, pixel defects have been divided mainly into two categories: disconnect bumps (mainly due to mechanical features) and other defects (due to problems in sensor and chip). The fraction of disconnected pixels over all chips as a function of the geographical pixel position is shown in Figures 4.27(a) and 4.27(b) for 3D and planar sensors, respectively. Disconnected bumps are clearly located in the corners of the chip that is already known being a weak point in the bump-bonding process. Similarly, disconnected bumps are located in the outer columns and

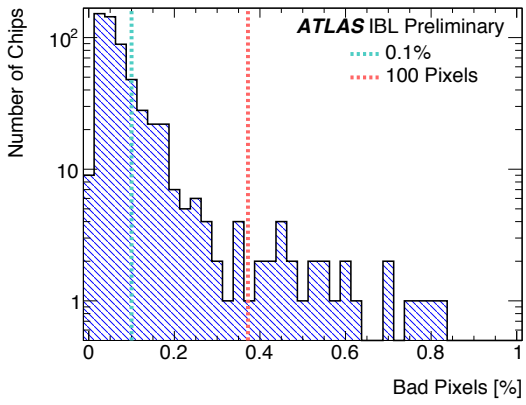

Figure 4.26: Distribution of bad pixel fraction per chip for 18 staves [45].

rows of the chip. Planar modules have a larger number of disconnect bumps just in the middle of them (columns 80 and 81) since two FE-I4 chips are bump bonded to one planar sensor. It is also to be noticed that some areas of disconnected bumps are generated only from one chip. Figure 4.28 shows the total fraction of bad but not disconnected pixels as a function of chip row and column numbers for 18 staves. Pixel failures other than disconnected bumps are distributed over the whole chip or can appear in form of columns, as a results of the interconnection scheme of pixels.

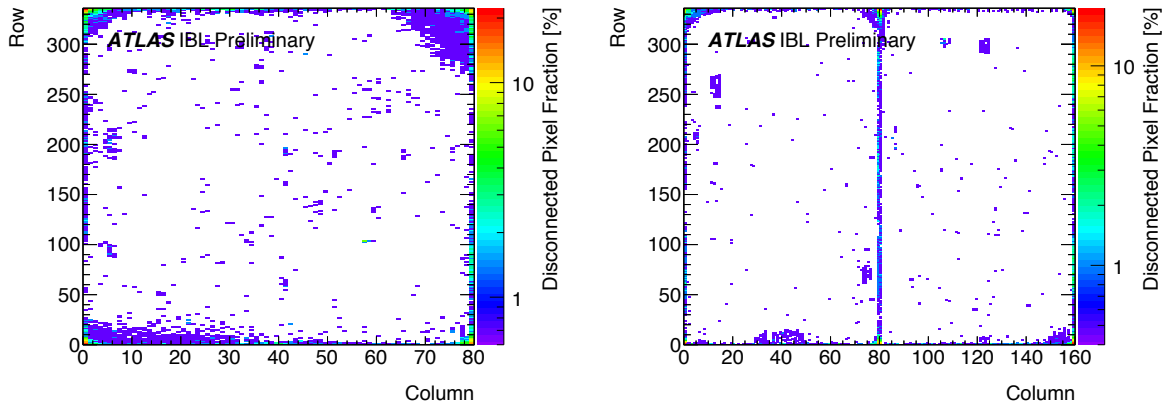

(a) (b)

Figure 4.27: Total fraction of disconnected pixels on (a) 3D and (b) planar modules as a function of chip row and column numbers for 18 staves [45].

Analysis of pixel defects at the stave level

Besides the pixel failures distribution over the chip, it is useful to see their distribution along the stave. Figure 4.29 shows the total number of bad pixels as a function of η. A clear increase of the number of bad pixels with the increment of η values is visible. This feature is explained by the chosen strategy to load the best modules into the central region of a stave. Furthermore, considering that at the highest η values only 3D modules are present, it is easy to conclude that the average quality of planar modules is better than 3D modules. This is also visible in

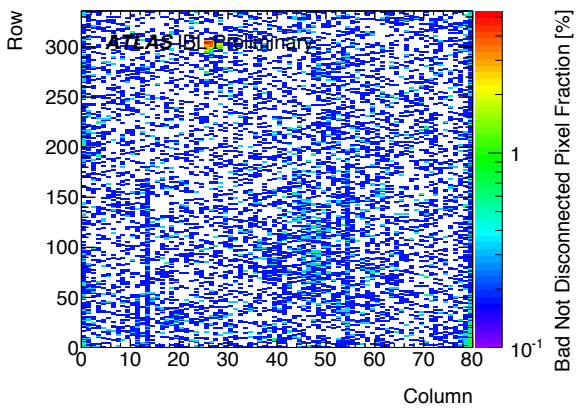

Figure 4.28: Total fraction of bad but not disconnected pixels as a function of chip row and column numbers for 18 staves [45].

Figure 3.12 where the yield of IBL 3D modules production results already lower than for planar modules.

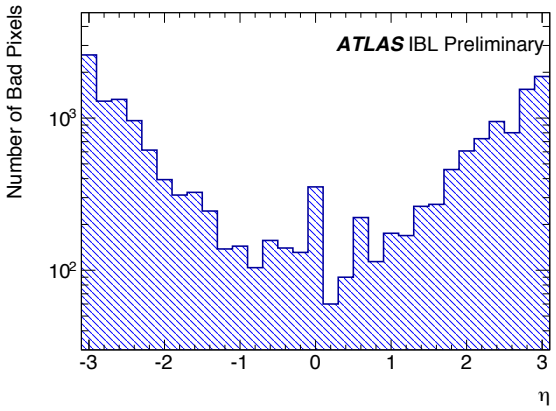

Figure 4.29: Total number of bad pixels as a function of η for all 18 production staves [45].

An overview of the total number of bad pixels for each stave is shown in Figure 4.30(a). The two dashed lines indicate marks at 0.1% and 0.2% of total bad pixels per stave as the IBL specification requires a stave to be below 1%. All staves are well below this cut, 80% of staves are below 0.2% and 50% of those staves are even below 0.1%. Figure 4.30(b) summarizes the total number of bad pixels divided per failure category. About 50% of failures are due to disconnected bumps, the other 50% are distributed between a pixel being analog dead or its tuning being impossible. The exact numbers of pixel defects per category and stave are collected in Table 4.3.

4.1.9 Selection of the 14 best staves

Since all 18 production staves have passed the QA criteria, the 14 best staves to be installed around the new ATLAS beam-pipe have to be selected. The main concern for the stave selection is the coverage efficiency of the geometrical acceptance in terms of bad pixels since during IBL operation these pixels will need to be masked. The stave quality is ranked taking into account the

Stave	Digital	Analog	Disconnected	Merged	Untuneable	Noisy	Crosstalk	Total
ST01	6	389	272	3	232	11	98	1011
ST02	10	255	54	3	117	15	125	579
ST03	6	375	473	0	182	21	178	1235
ST04	2	201	254	0	275	8	59	799
ST05	2	207	172	0	183	4	33	601
ST06	6	206	337	0	147	9	29	734
ST09	8	360	476	3	167	8	88	1110
ST10	16	179	304	0	141	3	3	646
ST11	10	196	159	0	155	8	37	565
ST12	15	172	169	0	166	7	13	542
ST13	9	127	205	0	336	6	35	718
ST14	4	161	1364	0	330	7	11	1877
ST15	5	222	350	0	259	20	8	864
ST16	1	237	414	1	187	15	24	879
ST17	2	214	598	0	229	5	4	1052
ST18	13	161	902	1	178	2	9	1266
ST19	10	163	543	0	228	11	16	971
ST20	14	224	1051	0	535	13	302	2139
Total	139	4049	8097	11	4047	173	1072	17588

Table 4.3: Overview of the number of different bad pixel categories for the 18 staves [45].

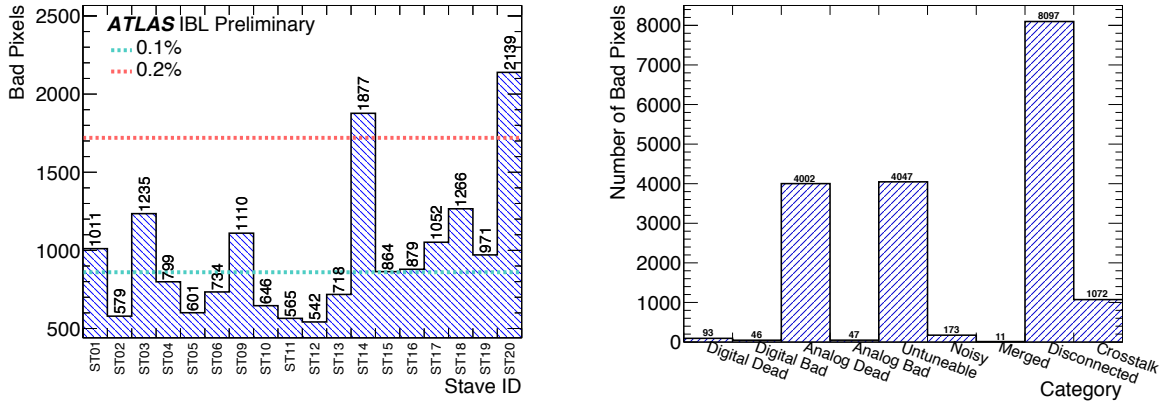

(a) (b)

Figure 4.30: Number of bad pixels (a) per stave and (b) for 18 production staves.

geometrical acceptance inefficiency due to bad pixels where the η-weighted bad pixel fraction V is defined as

$$V = \frac{\sum_{i \in \text{ bad pixels}} \cosh^{-1}(\eta_i)}{\sum_{i \in \text{ all pixels}} \cosh^{-1}(\eta_i)} \tag{4.4}$$

the factor $\cosh(\eta_i)^{-1}$ is the weight of the geometrical acceptance of the pixel i measured in the η-ϕ coordinate system. A low score indicates a small bad pixel ratio. This weighting scheme is preferred to simply sum-up the bad pixel ratios as it enhances the pixels in the central rapidity region and suppress them in the forward rapidity region. In addition to the geometrical acceptance in the η-ϕ plane, other factors have been taken into account for the stave ranking more related to mechanical and engineering constrains. In particular, the difference between the minimum and maximum height of staves, i.e. planarity, has been considered for their integration around the beam-pipe with the restriction to have the best planarity in the first and last integrated stave due to installation necessities. Table 4.4 summarizes the stave position in the IBL detector, the score obtained for each stave and the planarity. The production staves that have not been selected are ST01, ST03, ST14 and ST20. In total 168 planar, 60 3D CNM and 52 3D FBK sensor modules are mounted on the 14 staves that form the IBL Detector.

The two-dimensional distribution of bad pixel ratios has been plotted as a function of η and ϕ (Figure 4.31(a)). Stave overlap is taken into account in this plot and the ratio is computed as the number of bad pixels per total number of pixels in a unit cell. The higher ratio of bad pixels is distributed uniformly on ϕ at high η regions as expected from the results obtained in Section 4.1.8. Nevertheless the operational fraction of pixels in the η-ϕ plane can be considered well distributed with only few exceptional channels with an operational fraction around 95%. The total bad pixel ratio of the integrated IBL staves is 0.07% for $|\eta| < 2.5$ and 0.09% when considering the full eta range. The corresponding numbers for the four not installed staves are 0.16% and 0.18%, respectively (Figure 4.31(b)). The number of operational channels in the final IBL detector is 99.9%.

Position	Stave	Number of bad pixels	Score	Planarity [μm]
#01	ST17	1052	1.01	114
#02	ST02	579	0.44	205
#03	ST19	971	1.13	266
#04	ST09	1110	1.00	229
#05	ST18	1266	0.94	336
#06	ST04	799	0.69	235
#07	ST13	718	0.56	224
#08	ST10	646	0.62	243
#09	ST11	565	0.58	298
#10	ST12	542	0.62	314
#11	ST16	879	0.82	329
#12	ST06	734	0.79	290
#13	ST15	864	0.84	325
#14	ST05	601	0.68	189
n/a	ST01	1011	1.04	224
n/a	ST03	1235	2.48	223
n/a	ST14	1877	1.11	218
n/a	ST20	2139	2.01	237

Table 4.4: Ranking and loading order overview of the 14 IBL staves. The position is sequential around the beam pipe. The cooling pipe of the stave in position 01 is at $\phi = -6.1^\circ$, subsequent staves are displaced by 25.7° in ϕ. The score is determined by the number of bad pixels, each of which is weighted according to the position on a stave. A lower score thus translates into a higher quality stave. The planarity shows the difference between the minimum and maximum height of a stave. For completeness, the bottom four lines show numbers for the staves that were not chosen for installation. For the stave loading around the beam pipe, not only this score but a uniform $\eta - \phi$ bad pixel distribution and engineering constraints are also taken into account [45].

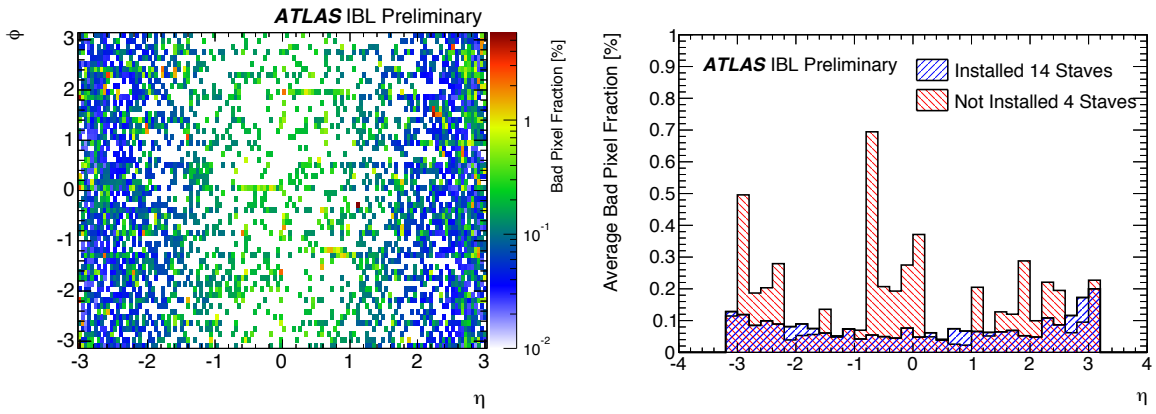

(a) (b)

Figure 4.31: (a) The bad pixel fraction in the η-ϕ plane for the 14 IBL staves. It represents the inefficiency map of the IBL as it is installed. (b)Average bad pixel ratio distribution as a function of η for installed and not installed production staves [45].

4.2 Studies of IBL wire bonds operation in a ATLAS-like magnetic field

In parallel to the stave QA, it is important to qualify the reliability of detector components under specific operation conditions that will be found in the ATLAS experiment. In this context, a particular attention has been addressed to the effects of magnetic field on wire bonds that could potentially have a critical impact on IBL.

A typical wire bond of 2 mm length in a 2 T magnetic field, having a 100 mA current passing through it, can suffer a maximum force of $4{\cdot}10^{-4}$ N, which is three orders of magnitude smaller than the minimum force needed to break a wire bond. However, the wire can start to oscillate if the current passing through it has an AC component with frequency close to the wire's mechanical resonance frequencies. This oscillation depends on several factors as wire length, wire orientation angle with respect to B-field, current, B-field strength, etc. Depending on oscillation amplitude and number of cycles, the wire can also cross the material elastic limit and micro-cracks can develop at the heel leading to possible failures of the bond [52].

The IBL modules have wire bonds connecting the FE to module-flex and the stave-flex to module-flex [25]. Several of these wire bonds transport an AC current, which amplitude varies depending on the wire functionality. Studies have been conducted to identify potential dangers of resonant wire bond vibrations in a 2 T magnetic field . Two different solutions for wire bond protection against damage have been tested.

4.2.1 Experimental set-up

IBL wire bonds connecting flex and FE-I4 are tilted with respect to the B-field at orientation angles between 50° and 90°. Depending on this angle, a wire carrying current experiences a Lorentz force, whose components can be parallel (90° orientation angle) or perpendicular (0° orientation angle) to the wire plane. In the IBL case, the force has both components while in the case of, for example, the ATLAS Pixel Detector in the disk region the force is maximum

and perpendicular to the wire plane (most dangerous orientation).

Only few IBL wire bonds, namely digital and analog voltage regulator wire bonds, can draw a high current [53]. For each regulator pad 2 or 3 wire bonds are present. They are the longest and most bended wires on the module. Furthermore, even if there are 2 or 3 wire bonds connected, it is a known feature of low resistance parallel connections that the sharing of current among them is not well defined: thus the worst case is when all the AC current component is passing through one of the three wires. Usually the analog current is larger but constant while the digital current varies with configuration and chip activity (hits and trigger). The configured currents are about 300 mA (DC) and 100 mA (AC) for analog and digital regulator wire bonds, respectively. The worst IBL case is 100 mA AC current passing through one wire. This current can be dangerous only if its frequency is close to the mechanical resonance frequency.

A dedicated set-up (Figure 4.32) has been assembled to reproduce the IBL wire bond operation conditions. Special test boards able to simulate the 370 μm step present between FE and flex, have been used to bond 25 μm diameter IBL-like FE-flex wires with different lengths[6] l (1.5 mm, 2.0 mm, 2.8 mm) and orientation angles (50°-90°). The board can be fitted into the two poles of the electromagnet, which produces a 2 T B-field perpendicular to the board. In these conditions the IBL configuration is fully reproduced.

Sine and square waves with an AC current amplitude varying between 0 and 100 mA are produced by a waveform generator and sent to the wire bonds. The wires are monitored with a CCD camera and a stroboscope is used to make the wire movement easily visible.

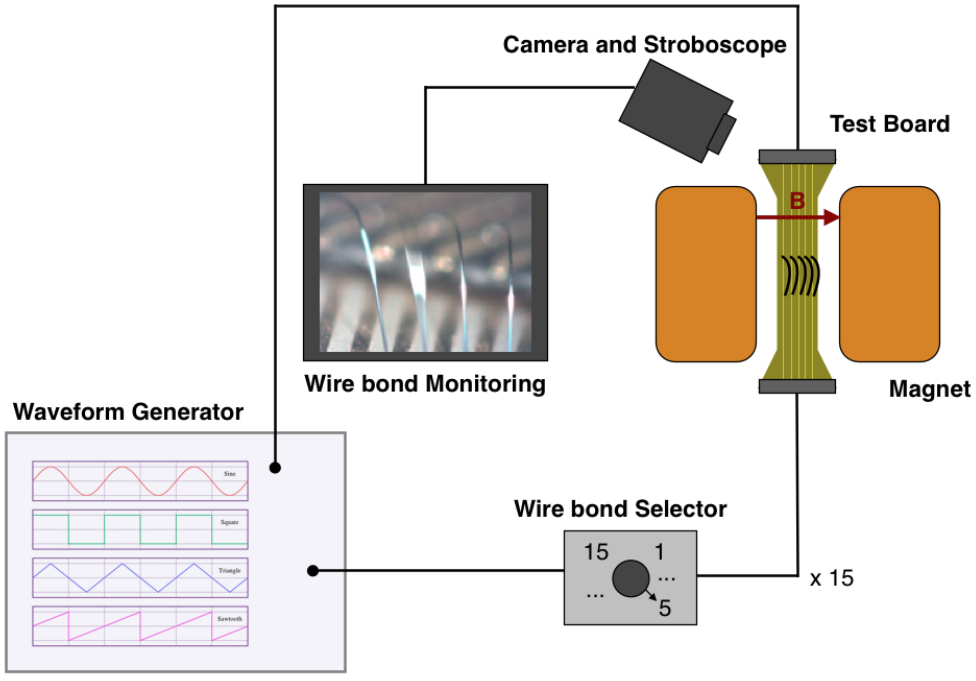

Figure 4.32: Schematic view of the experimental set-up used to test IBL-like wire bonds in 2 T magnetic field.

[6]IBL shortest and longest wire bonds are about 1.5 mm and 2.8 mm long respectively. A value in between, namely 2.0 mm, has been also used for the test.

4.2.2 Modeling approach for wire bonds fatigue

In a simplified view, a wire bond can be considered as a loaded beam that can oscillate in three dimensions. The natural frequencies depend on the wire bond length, diameter and loop height. However several factors can play an important role as for example the wire's material and the ultrasonic bonding process, which defines the final shape of the wire and the local deformations of the heel region.

A one dimension Finite Element Analysis (FEA) simulation has been performed to address the search of resonance frequencies in the experimental tests for different wire bond lengths (Table 4.5) [54].

Wire Length (mm)	Resonance Frequency (kHz)				
	1	2	3	4	5
1.5 mm	23.77	68.94	74.65	145.64	147.12
2.0 mm	12.75	37.32	40.62	78.72	79.61
2.8 mm	8.92	24.16	26.61	52.32	52.83

Table 4.5: Resonance frequencies for different wire lengths obtained with a 1D FEA model [54].

On the contrary, the empirical measurement of the fatigue threshold is extremely difficult and so, as approximate result, a numerical simulation has been performed, based on the vibration amplitude required to increase the plastic strains in the heel section of the wires used. The analysis is done in three steps:

Simulation of the effects of the ultrasonic bonding process. Instead of simulating the motion of the bonding tool, a rigid body has been used to compress the ends of the wire with a shape that replicates a deformed profile equivalent to the one observed in IBL-like wire bonds (Figure 4.33). A special attention has been given to the region of wire's foot and heel since it is known to be the weakest point during oscillation.

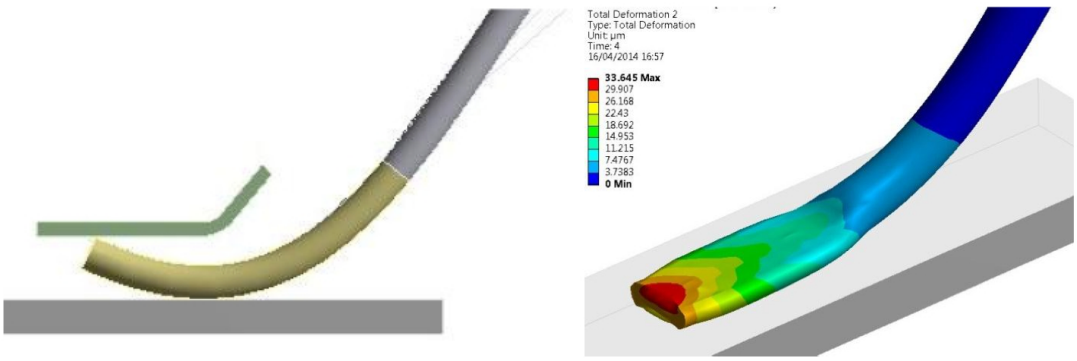

(a) (b)

Figure 4.33: (a) Simulation of the bond foot obtained with the ultrasonic bonding process. (b) Deformation in the foot region after the bonding simulation [54].

Thermal loading to account for Joule heating effects. After the accomplishment of the bonding process, the thermal stresses induced by the Joule heating effect have been included. The accumulated plastic strains obtained after the two steps are not negligible and they are considered as a reference point for the estimation of the vibration amplitude that induces an increase of this plastic strain.

Estimation of the oscillation amplitude to increase the plastic strains. A static load is applied to the wire in the direction perpendicular to the wire's plane: this load creates a deformation pattern equivalent to that of the first resonance mode. After each load increment, the plastic strain of every element within the heel region is compared to the one obtained after the thermal loading. When the critical load increment is identified, the corresponding vibration amplitude is obtained by the lateral displacement of the node located at the top of the wire.

Two different wire thicknesses in the foot region have been simulated since wire bonds have not all the same foot shape, which depends on the operator doing the bonding. As typical values, 11 μm and 17 μm thickness have been used . For a wire of 2.8 mm length, which is the maximum bond's length used in the IBL detector, the vibration amplitudes obtained are 42 μm and 45 μm respectively.

4.2.3 Experimental studies of resonant wire bond oscillations

The results obtained from the FEA simulation provide well defined resonance frequencies depending on the resonant mode and wire's length (Table 4.5). Nevertheless the bonding is not completely reproducible and each wire has small mechanical differences.

The resonance frequencies have been found experimentally on wires of different lengths bonded with the same bonding machine, i.e. using same setting parameters. The resonance frequency is defined as the frequency at which the oscillation amplitude reaches the maximum value. The spread of the resonance frequencies obtained testing several wires with the same length is about 1%, revealing a good reliability of the bonding machine. The first resonance frequency obtained for 1.5 mm, 2 mm and 2.8 mm are 25740 Hz, 15600 Hz and 9550 Hz respectively. These values are not in complete agreement with FEA simulation: a shift of about 10% is systematically observed. This can be explained by the simplified model used on the simulation where not all wire's characteristics have been included.

The resonance frequency ν is proportional to l^{-2} and the amplitude to l^4. The second, third and so on resonance frequencies are not visible with the present set-up. The square of the oscillation amplitude is proportional to the power spectrum of oscillations that can be fitted with the Lorentzian peak [55]:

$$p = \frac{(\gamma^2/4)\, H}{(\omega - \omega_0)^2 + (\gamma^2/4)} \tag{4.5}$$

where H is the peak height, ω_0 the resonance frequency, γ the full width half maximum (FWHM) of the peak. Figure 4.34 shows the oscillation amplitude as a function of the frequency obtained experimentally for a 2.8 mm wire. The amplitude has its maximum at the resonance frequency and it halves changing the frequency of $\pm$50 Hz. The range at which the

oscillation is still present is $\pm 2\%$ of the resonance frequency with an amplitude about a factor 7 less.

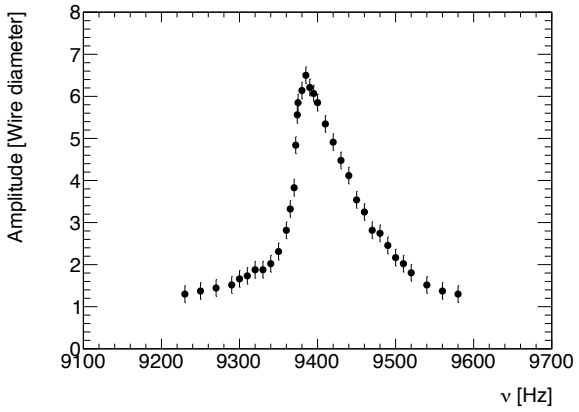

Figure 4.34: Oscillation amplitude expressed in wire diameter (25 μm) as a function of the frequency for a wire of 2.8 mm length.

Systematic studies have been conducted changing duty cycle and rise time of the AC current square wave passing through the wire. Indeed the electrical signal passing through the digital regulator wire bonds of an IBL module has a relative long rise time and it can have a duty cycle of about 5%. In this situation the power transmitted to the wire bond is different and consequently the oscillation amplitude changes. Figure 4.35(a) shows the oscillation amplitude and the root mean square (RMS) of the current as a function of the duty cycle for a 2.8 mm wire in a 2 T B field with a square wave current of 20 mA peak to peak. The maximum amplitude is obtained with a 50% duty cycle while it clearly decreases following the reduction of the RMS current. A drop of 75% of the initial amplitude is obtained at very low duty cycles. Figure 4.35(b) shows the variation of the oscillation amplitude as a function of rise time obtained testing 2.8 mm wire bonds at a resonance frequency of 9800 Hz. A rise time equal to 0 μs means a perfect square wave while 50 μs is equivalent to a triangular wave. In the latter case, a decrease of the oscillation amplitude of about 35% is visible.

Since the IBL current passing through regulator wire bonds can be a mix of a sine and square wave, the Fourier harmonics plays an important role in identifying the range of frequencies at which the wire bond oscillates in a B field. The amplitude of the Fourier harmonics for a square wave are:

$$Y(\nu) = \sum_{k=-\infty}^{\infty} \frac{1}{2} sinc\left(\frac{k}{2}\right) \delta\left(\nu - \frac{k}{T_0}\right) \quad for\ k \neq 0 \tag{4.6}$$

where T_0 is the signal period, ν is the frequency and $sinc(t) = \frac{sin(\pi t)}{\pi t}$ with $sinc(0) = 1$. Indeed the oscillation amplitude at the resonance frequency is higher (about 1.3 times) for a sine wave with respect to a square wave since the first can be considered like the first harmonics of the square wave. At the frequency of the third harmonics the wire bond oscillates even if the amplitude is about three times smaller than at the resonance frequency, in agreement with theory. At higher harmonics, the wire bond still oscillates but its amplitude is negligible and not anymore visible with the present set-up. The resonance frequency can also be considered

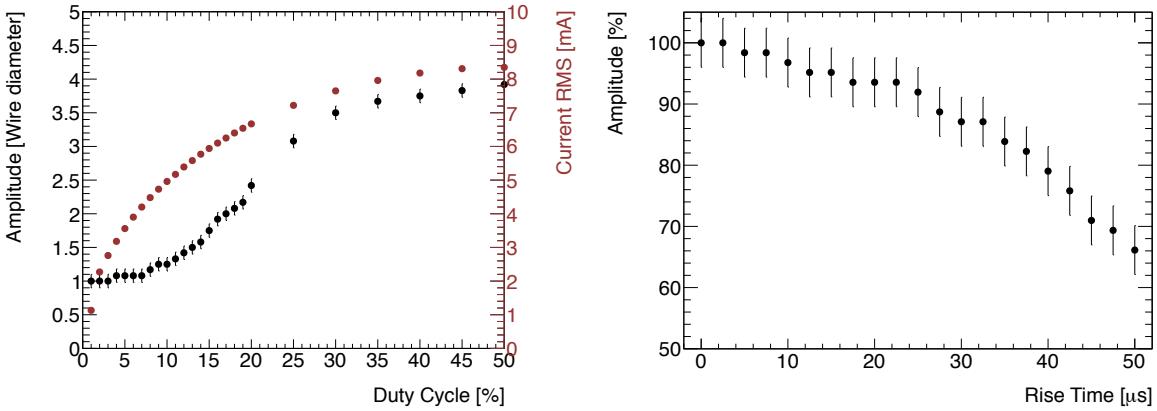

(a) (b)

Figure 4.35: (a) Oscillation amplitude at the resonance frequency and RMS current as a function of duty cycle sending a square wave to a 2.8 mm wire bond in a 2 T B-field (orientation angle $\sim$30°). As indication, a 30% duty cycle means the signal is on 30% of the time and off 70% of the time. (b) Oscillation amplitude at the resonance frequency as a function of rise time. The rise time on the x-axis takes into account only the leading edge (trailing edge has the same value).

as one of the "n" harmonics and therefore oscillations are present at lower frequencies (one third, one fifth, etc. of the resonance frequency) when a square wave is used. The oscillation amplitude diminishes with the decrease of the frequency since the square wave with frequency 1/n times the resonance frequency contains the resonance frequency only as the n harmonics, whose amplitude is given by 4.6. In the case of wires of 2.8 mm length with an AC current of 100 mA peak to peak, a frequency of $\nu/3$ or $\nu/5$ still generates an oscillation amplitude quite large that could cause damage to the wire. When the frequency is reduced by at least a factor seven, the amplitude is relatively small or almost invisible in the set-up.

4.2.4 Protection of wire bonds against oscillations

The most critical point of a wire bond is the heel where the Al wire has been scratched and bended during the bonding process. Indeed this is demonstrated by the fact that wire bonds usually break at the heel when they are exposed to mechanical strains as, for example, oscillation.

The typical method to protect wire bonds against breakage is to encapsulate their feet and heels. The ATLAS Semiconductor Tracker (SCT) and Pixel Detector applied the encapsulant Dymax 9001-E-V.3.1 (called Dymax in the following) on their wire bonds [56]. The same product has been tested on IBL-like wire bonds dropping it on the foot heel. The encapsulation height varies from 35 μm to 50 μm, being the application done manually. A second solution has been proposed to protect the whole wire against water contact or contaminants since it has been demonstrated that IBL wire bonds can be corroded in a high humidity environment. Urethan sprays are often used for standard PCBs to create a shield against dust, moisture and contaminants. The polyurethan "CellPack Urethan D9201PU" (called Urethan in the following) has been tested for the IBL case. The wire bond coating is done spraying manually the Urethan

from the canister. The consequence is a not uniform coating with Urethan drops along the wire and some areas not well covered.

Figure 4.36 shows the mean resonance frequency as a function of the wire bond length for the three cases (bare, encapsulated and coated wire bond) where the dependence of the resonance frequency to l^{-2} is visible. The resonance frequency of encapsulated wire bonds is about 10% higher than bare case and, on equal terms, a higher current is necessary to get them oscillating. This behavior leads to the assumption that the wire bond feet are protected by Dymax, which shortens the wire's length and lessens the heels movement. On the contrary the resonance frequency of coated wire bonds is lower (between 2% and 10%) than the bare case. The higher error bars are just due to a large spread of resonance frequencies because of a different amount of Urethan covering the tested wires. In general, coated wire bonds oscillate at higher currents than the bare case but lower than the encapsulation case, meaning that the coating offers a vibration protection, which is by the way weaker than the encapsulant.

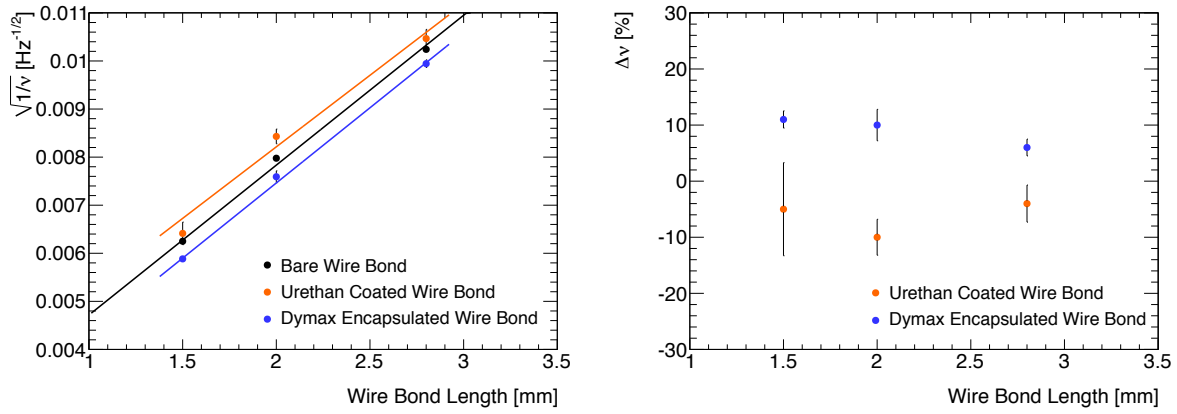

(a) (b)

Figure 4.36: (a) Resonance frequency as a function of wire bond length for bare, Urethan coated and Dymax encapsulated wire bond. (b) Resonance frequency shift after the application of urethan or Dymax to bare wirebonds.

4.2.5 Wire bond resistance against oscillations

The resonance frequency amplitude at which the wire oscillates is of fundamental importance since, depending on it and on number of cycles, the wire can overcome the material elastic limit and micro-cracks can develop at the heel. If the wire is left in oscillation mode at these conditions, the cracks can further enhance until the wire breaks. The breakage always occurs at the heel, in particular on the side where the first bond is done (for IBL case it is the upper bond). Indeed during the bonding process, the wire is extremely stressed since after the cold welding the wire is bended of about 45° before being driven to the second bond.

A first symptom of wire's weakening is the drop of oscillation amplitude along time, which can happen suddenly or after a certain number of oscillation cycles, and it is caused by the development of cracks at the heel. At this stage a new resonance frequency can be obtained decreasing the frequency of the current and the new oscillation amplitude obtained is lower then the first one. This process can be repeated several times causing further damages on the

heel wire until the wire breaks. The decrease of oscillation amplitude, and consequently the shift in the resonance frequency, can be used as parameters to monitor the wire resistance to oscillations.

The worst possible IBL scenario, that is an AC current of 100 mA peak to peak through the wire in 2 T B-field, has been tested on bare, coated and encapsulated wires of different lengths and with several orientation angles with respect to the B-field. The wires are left in oscillation for about 5 minutes, which has been estimated to be a reasonable time with respect to the operation time in IBL. After this time the number of broken wires as well as the quantification of the possible shift of resonance frequency are recorded. As a general remark, the oscillation amplitude of wire bonds with lower orientation angles is higher. Table 4.6 summarizes the results obtained. The 1.5 mm wires are not affected by any decrease of amplitude and none of them break in the three configurations. On the contrary, the 2.8 mm wires are considerably subjected to damages: all wires have a decrease of amplitude both in bare and coating cases and 30% of them suffer an amplitude decrease in case of encapsulation. Furthermore about 15% and 10% of wires break in the bare and coating case respectively. Despite that, 2.8 mm wires do not break if their feet are encapsulated, remarking the effectiveness of the Dymax. For the 2.8 mm wires, the resonance frequency shift has been estimated to be 4.6%, 3.4% and 0.3% for bare, coated and encapsulated wires respectively. The coating solution provides an improvement in term of protection with respect to bare wire bonds but it is not good as the encapsulation. This disadvantage could be overcome if a better coating method covering completely and uniformly the wire bond length is developed.

Wire's length	Type of test	Wires affected (%)		
		Bare	Coated	Encapsulated
1.5 mm	Decrease of amplitude	0	0	0
	Broken wires	0	0	0
2.0 mm	Decrease of amplitude	65	65	20
	Broken wires	9	10	0
2.8 mm	Decrease of amplitude	100	100	30
	Broken wires	15	10	0

Table 4.6: Percentages of wires affected by an amplitude decrease or broken after 5 min in oscillation mode at 100 mA AC current in the IBL configuration. The test has been performed with wires of different lengths and in different conditions (bare, coated and encapsulated wire bonds). A total of about 60 wire bonds have been tested.

Wire bonds have been tested also in a "disk orientation" mode with a B-field of 1.1 T. The disk orientation is the worst case since the force applied to the wire is perpendicular to the wire bond plane and has the maximum value. In this condition, also wires of 1.5 mm can break with, in general, half of the AC current used for the IBL case ("barrel orientation").

4.2.6 IBL wire bonds during detector operation

An experimental set-up has been built to simulate as much as possible the operation conditions of IBL wire bonds in the ATLAS magnetic field. The results provide useful information for the

comprehension of the IBL wire bonds behavior being the real conditions well reproduced in the experimental set-up. The worst IBL case is a 2.8 mm wire with an AC current of 100 mA at a frequency close to its mechanical resonance frequency and with a higher orientation angle with respect to the 2 T B-field. It has been demonstrated that in this case the wire gets irreparably damaged after few oscillation cycles and it can easily break. Two types of wire bond protections have been investigated: the classical encapsulation of the wire feet and the coating of the whole wire. The last method is also useful to protect the wire against humidity or other possible contaminants. Even if the encapsulation remains the best solution for oscillation protection, it has not been implemented for IBL. This decision is due to the fact that at the time of the studies most of the staves were already produced and the application of the Dymax was considered too risky for the modules. The alternative solution against oscillations consists in avoiding the currents with the frequencies at which the wire bond can oscillate. For the IBL detector a Fixed Frequency Trigger Veto (FFTV) has been implemented for excluding potentially dangerous frequencies.

4.3 The IBL Detector towards LHC Run 2

The staves QA has been an extremely important step in the production and final accomplishment of the IBL Detector. The QA procedure has been systematically followed for the 18 production staves holding 216 planar and 144 3D modules (576 FE-I4 chips) for a total of 15.5 M pixels. Each module has been fully characterized through a series of tests, ranging from calibration to source scans. The obtained results allowed the selection of the best 14 staves for the construction of the IBL Detector, which has been successfully installed in the ATLAS experiment. The results of the QA tests have not only been useful for the stave selection but also for a deep comprehension of the new technologies adopted for the IBL Detector (as for example FE-I4 chip and 3D sensors). In addition, the detector tunings performed are a valuable input for the final calibration and operation during LHC runs.

Systematic studies have been also conducted to identify the best conditions for the detector operation in the ATLAS experiment. In particular, it has been demonstrated the vulnerability of IBL wire bonds when an AC current with a frequency close to their mechanical resonance frequency passes through them in presence of a high magnetic field. IBL-like situations have been examined and all dangerous resonance frequencies have been identified experimentally. Wire bond protections have been proposed and tested. The results obtained have been used for the implementation of a trigger veto for the IBL operation. Furthermore these studies can be considered a preliminary evaluation for the use of wire bonds in future silicon detectors.

The quality assurance and final commissioning have shown that the IBL Detector works extremely well with all FE-I4 chips operational and 99.9% of functional channels in the modules. IBL has been successfully operated during several ATLAS global runs in the final conditions (cold operation in 2 T magnetic field). The ATLAS Pixel Detector will join the LHC Run 2 with a new layer and an improved configuration ensuring the best possible tracking performance.

Chapter 5

Optimization of gaseous detector systems operation at LHC

The LHC muon systems are very large apparatus and a meticulous work for the optimization and monitoring of the present systems is ongoing permanently. One of the most critical and important infrastructure for particle gaseous detectors is their gas systems. The present chapter, after an introduction about the LHC gas system design, describes the standard techniques adopted for monitoring the gas mixture composition as well as their impact on detectors. The topic is even more important for systems where gas mixture is recirculated to contain operational costs and gas emissions. As it will be discussed, gas mixture recirculation can easily lead to accumulation of impurities, which could affect detector performance. However gas recirculation is not always the solution. An alternative technique, implying the recuperation of an expensive gas mixture component (CF_4), is also described in this chapter.

5.1 Gas systems for detectors at the LHC experiments

At the LHC experiments, 30 dedicated gas systems deliver the proper gas mixture to the corresponding detectors [57]. They are complex apparatus that extend over several hundred meters and ensure an extremely high reliability in terms of stability and quality of the gas mixture delivered to the detectors. Indeed, the gas mixture is the detector's sensitive medium and a correct and stable composition is a basic requirement for good and safe long term operation. Gas systems, as well as gaseous detectors, are subject to severe requirements on design and components to guarantee safe detector operation.

A modular design is adopted for the construction of the LHC gas systems. Every module fulfills a specific function and it can be configured to satisfy needs of different detectors. This modular and function oriented design is the key choice allowing effective construction and it constitutes an enormous advantage for the maintenance. Modules are standardized and the same industrial components are used to achieve equivalent roles. This allows maintaining critical spares and fast repairs in case of any failure. Also the software control associated to each module is standardized and it is developed for industrial Programmable Logic Controller (PLC[1]). The gas system building blocks are located over three different levels (Figure 5.1): the

[1] A PLC is an industrial pc with basic functionalities.

surface room (SG), the underground service room (US) and the experimental cavern (UX). Most of the modules are located in SG since it is the most accessible location. A first gas distribution into several channels is done in US, where the pre-distribution modules are located, while the final gas distribution system to the detectors is located in UX, where also the experiment is installed.

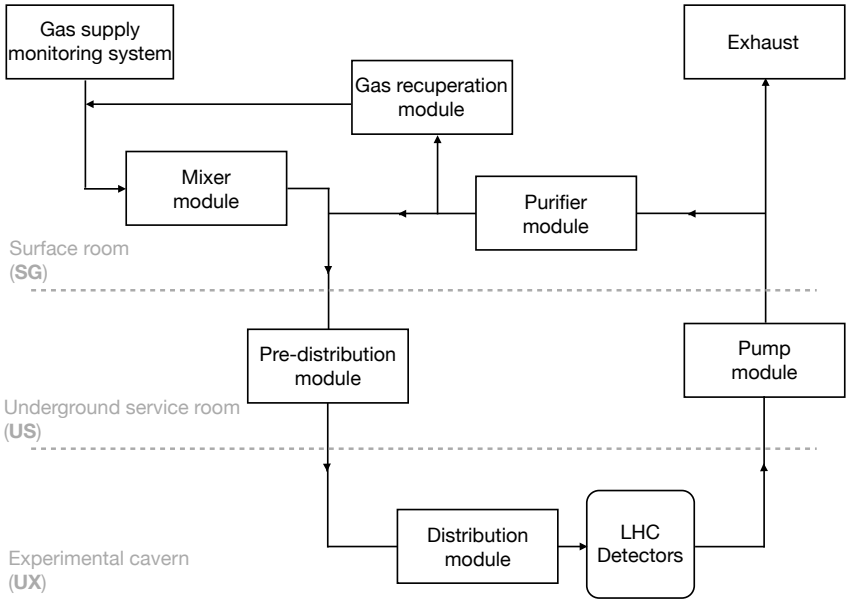

Figure 5.1: Schematic view of the main functional modules present in a LHC detector gas system.

Each LHC gaseous detector has its proper gas system since the requirements can be very different within the several detectors in the same experiment. Nevertheless a general description of the main building blocks can be commonly accepted for all LHC experiments:

Gas supply monitoring system Each gas is provided by two independent supply sources: one is in use while the second one is on stand-by and ready to automatically start when the first source is empty. In case of dewars for cryogenic liquids, the back-up source is ensured by a set of cylinders containing compressed gas. The gas supply monitoring system controls the availability and quality of each primary gas supply before it goes into the gas system. This implementation avoids the injection of contaminants into the gas system, and consequently into the detectors. It also detects unavailability of a gas by monitoring the supply pressure, the weight of low vapor pressure liquid, the gas flow as well as O_2 and H_2O concentrations.

Mixer module The primary task of the mixer module is to provide the suitable gas mixture. The mixer module has up to four gas input lines equipped with Mass Flow Controller (MFC)[2], which are controlled via software according to the detector needs: the flow is automatically tuned to guarantee the required replacement rate, to cope with detector's leak or gas recuperation efficiency, or even more to compensate for atmospheric pressure

[2] A MFC is a device used to measure and control the flow of fluids.

changes. Two MFCs are installed in each line since, during particular phases, it might be needed to supply different gases (for example for purging the detector when the standard gas mixture needs to be evacuated, like at the beginning of a long shutdown period) or standard mixture at very high flows (for example when the detector is going to be restarted after a long shutdown, i.e. fast filling mode).

Gas distribution The distribution of the gas mixture to each single detector is done in several steps. Once the gas mixture is prepared by the MFCs, it is sent to several pre-distribution modules located in the US. Each pre-distribution module relates to a specific detector sector of the experiment. Several gas parameters (as pressure, gas flow, etc.) can still be modified via online software during LHC runs. Afterwards, the gas is sent in the UX where the final distribution modules are located. Here pre-distribution lines are split into several smaller lines, which finally supply each individual module of the complete detector system. Depending on the design granularity, a module can be made of one or more individual detectors. Since the distribution modules are located on the experiment, they are subject to background radiation and intense magnetic fields. Therefore they are designed with simplified electronic or manual systems, which do not require access during operation. The supplied and return flows to each module are monitored with basic flowmeters developed at CERN. Manual valves allow to adjust the flow to desired values. Typical gas distribution systems are equipped with several hundreds of these flowmeters, depending on the detector granularity.

Gas system operation modes In the simplest gas system, the mixture is exhausted to atmosphere after being passed through the detector (open mode system). In case of large detector volumes or use of expensive gases, the mixture can be collected after being used in the detector and continuously re-injected into the supply lines (recirculation system, closed loop mode). Gas recirculation systems allow to reduce operational costs by 90% or more. However gas recirculation is a complex process where flows and pressures need to be constantly regulated on the return lines of the detectors. Moreover since the renewal period of the gas volume is longer, the accumulation of impurities becomes a typical issue. The gas mixture coming out from the detectors is sent, by means of a pump module, to the SG building, where a purifier system based on cleaning agents allows purification of the gas mixture from possible pollutants. Then a small percentage of gas, which depends on detector and system constraints, is sent to the exhaust line while most fraction is dispatched to the pre-distribution modules. The fraction of gas mixture sent to the exhaust is automatically replaced with fresh mixture coming from the mixer module. The range of this fraction is typically between almost 0% and 10%.

Purifier module In the recirculation process several impurities can accumulate because of leaks, gas supply quality, detector permeability to air, etc. The typical impurities are N_2, O_2 and H_2O. Other specific impurities can be created and then accumulated in the closed loop (CL) under the combined action of electric field, charge multiplication and high radiation background. For safe operation of detectors, it is mandatory to filter as much as possible the impurities accumulated. This can be afforded installing cartridges filled with suitable cleaning agents in the gas system: molecular sieves are used for wa-

ter removal, metallic catalysts for oxygen absorption and other materials can be added to filter specific impurities. Each purifier module contains two cartridges of typically 24 liters: during normal operation the gas mixture is passing through one column while the other is being regenerated or it has just completed the regeneration cycle and it is ready to be used. With this automated cycle, when a cartridge is saturated, a second one is ready to be used avoiding interruption to the gas system operation. The purifier module is one of the most complex in the gas systems both in terms of software logic and operability. Several precautions have to be taken into account (details in Section 5.4).

Gas analysis module Each LHC experiment is provided with at least one gas analysis module, which is used to continuously monitor critical mixture components or impurities through automated cycles. The gas analysis module is equipped with O_2 and H_2O sensors as well as Infrared (IR) analyzers to monitor the concentration of flammable gases. All analysis modules are completely automated: they can be programmed to sample all gas streams including references or calibration gases. Expert operators can trigger remotely the analysis of specific lines at any moment. The software control is configured to generate alarms and to exchange data with the specific detector DCS[3]. Two analysis modules, one in CMS and one in LHCb, are instrumented also with Gas Chromatograph (GC) allowing for more specific studies. In particular, GCs are used to monitor the mixture composition and the presence of more complex impurities (Section 5.2).

Gas recuperation module Gas recuperation plants are used to recuperate expensive gases during emptying of detector volumes (mainly during technical and long shut-downs) for containing operational costs or they are used to reduce the level of impurities without increasing the fresh mixture injection. Several recuperation plants have been built for the LHC gas systems. In particular, they are used to recuperate Xe, C_4F_{10}, nC_5H_{12} and CF_4. Unlike the building block modules, in this case all gas recuperation systems are different from each other. A common point is the recuperation method: the mixture returning from the detector is cooled down until the liquefaction point of the gas, then the liquid is recuperated and stored either in liquid or in gas phase. A different method has been developed for the CF_4 recuperation plant of the CMS CSC, as it is described in Section 5.6.

Each gas system is controlled by a PLC, which is located in a control rack with the crates corresponding to all functional modules. These crates collect the module Input/Output (I/O) informations that are then sent to the PLC through Profibus[4], where the control software is implemented. All measured values (pressure, flows, mixing ratios, temperatures, etc.) are processed in the PLC and used to control the process as well as to generate alarms or interlocks to the gas system operation. A user interface has been developed using standard PVSS[5]. It allows to monitor the status of each gas system device, control active components, transfer to

[3]The Detector Control System (DCS) is a software tool used to supervise the individual detector components as well as the common experimental infrastructure.

[4]PROFIBUS (Process Field Bus) is a standard for field bus communication in automation technology and was first promoted in 1989 by BMBF (German department of education and research) and then used by Siemens.

[5]PVSS (http://www.pvss.com) is a control system suited for a wide variety of applications. It meets the highest standards of all sectors, from traffic solutions to distribution networks for energy, water and gas.

the PLC regulation set points and alarm thresholds. All relevant parameters are also published using Data Interchange Protocol (DIP)[6] allowing easy integration with specific DCS.

The gas systems construction started around 2000 with the first systems being in operation in 2006. During the LHC Run 1, the gas systems were operated continuously until the start of LS1. The LHC gas systems reliability during the last three years is greater than 99.95%, corresponding to less than 1.5 hours of down-time per year per system (power-cuts and not-related external failures excluded). The relatively long duration of LS1 has given a great opportunity to review the existing detectors and related infrastructures. The consolidation program elaborated for the gas systems is articulated around three main points: reduction of down time due to periodic maintenance, required upgrade in functionalities needed to cope with the increase of LHC performance and reduction of operational costs as well as impact on environment. For example, circulation modules have been equipped with spare pumps allowing to perform periodic maintenance without interrupting operation. Extensive leak search campaigns have been also performed on primary supplies, distributions and detectors. This activity is complemented by the conversion of open mode gas systems to recirculation.

5.2 Gas mixture monitoring

A crucial point of the gas system operability is the delivery of the correct gas mixture to the detectors that can be affected by several factors, as, for example, the not correct functioning of the MFCs or purifiers as well as contamination coming from the detectors themselves or the supply bottles. These factors are controlled by specific instruments and human interventions until a certain level. Indeed, the task becomes complex when many gas systems run continuously. The faults cannot be always suddenly spotted, especially when they are related to "non-standard cases", and the consequences can be visible in detector operation and performance.

The gas analysis module present in each experiment is controlled through the general Gas Control System (GCS) of the experiment. All gas sampling points from the different detectors are connected to this rack and the software control is regularly scanning the selected gas lines allowing the measurements of O_2 and H_2O concentrations [58].

The exact concentration of each gas component can be measured through dedicated analysis instruments that it is not convenient to install in each system. A typical solution is the use of a common gas chromatograph (GC) for all detector systems in a given experiment since the GC can be installed in the gas analysis module allowing the measurements of the gas composition for all gas analysis streams. CMS and LHCb are already equipped with permanent gas chromatography stations where the Agilent microGC3000 is connected to the selection manifold of the standard analysis rack.

The GCs can have different columns that allow the separation and identification of several components. The GCs used at LHC experiments are equipped with the following columns:

OV-1 Polar column, which separates hydrocarbons from C_4 to C_{12}, BTEX[7], VOC[8].

[6] DIP is a communication system which allows relatively small amounts of soft real-time data to be exchanged between very loosely coupled heterogeneous systems.

[7] BTEX stands for benzene, toluene, ethylbenzene, and xylenes.

[8] Volatile organic compounds

PPlotU Porous Layer Open Tubular column, which separates C_1 to C_4 hydrocarbons, CO_2, CH_4, H_2O, H_2S, SO_2, N_2O.

MolSieve 5 Å zeolite molecular sieve column, which separates permanent and noble gases: Ne, H_2, O_2, Ar, N_2, CH_2, CO.

The regular monitoring of the gas mixture using gas chromatography stations allows identifying the origin of potential problems like low quality of gas supply, outgassing material, drift in the calibration of the MFCs or faults in some gas system components (pressure regulator, valves, etc). Indeed, the GC sensitivity can reach the order of ppm for all types of gases analyzed. Figure 5.2 shows an example of gas chromatograms for the CMS CSC detectors using two different GC columns: the PPU (Figure 5.2(a)) can separate the three components of the CSC gas mixture (Ar, CO_2, CF_4) while the MolSieve (Figure 5.2(b)) allows the identification of O_2 and N_2.

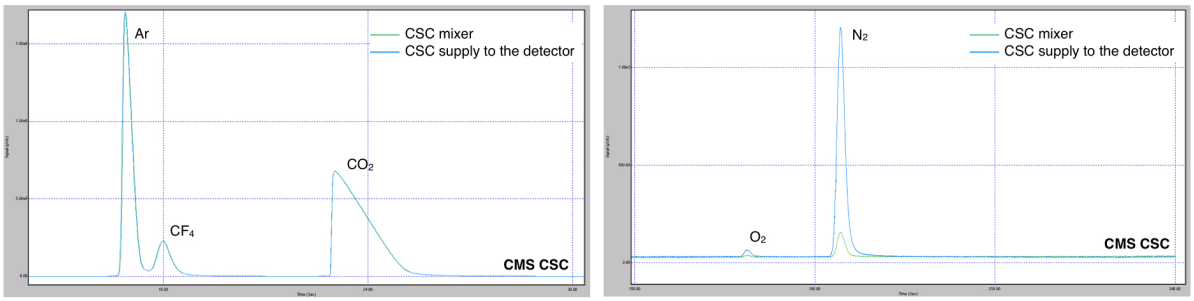

(a) (b)

Figure 5.2: (a)Gas chromatograms of the CMS CSC gas mixture in two analysis points. "CSC mixer" is the GC analysis of the gas mixture after the mixer while "CSC supply to the detector" is the GC analysis of the gas mixture sent to the detector after purification and the addition of a small percentage of fresh gas. (b) The "CSC supply to the detector" contains a higher quantity of both components coming from the CSC permeability to Air.

However, in some situations, GC analysis does not reveal complete information about gas mixture composition, especially in relation with gaseous detector performance. Indeed GCs are limited to concentration of the order of 1 ppm while negative effects on detectors can be produced by much lower concentrations or by the main gases present in the mixture. Moreover, GC analysis remains a quite complex and time consuming task: despite the availability of software tools allowing automated integration, the human intervention is often required. Since the promptness in detecting possible issues as well as the monitoring of real detector performance are of vital importance, an alternative solution has been investigated.

A good candidate is Single Wire Proportional Counter (SWPC) detector [59], which can be very sensitive to changes in gas mixture composition or to the presence of pollutants. These detectors can be considered as a good complement in the use of the GC since they can be continuously operated allowing the prompt detection of any gas variation, as it will be discussed in detail in Section 6.1.

5.3 Correlation between gas mixture quality and detector performance

MFCs are key devices for the gas mixture preparation (Section 5.1). The gas flow passing through the MFCs is regulated via software to provide each gas in the correct ratio. This process is based on the correct MFC calibration. However, MFC calibration may degrade during operation and checks have to be foreseen every one-two years. Periodic GC analysis of the gas mixture can spot the occurrence of these faults. Figure 5.3(a) shows the trend of the SF_6 concentration in the RPC gas mixture: a big deviation (from 0.30% to 0.45%) was detected in April 2011, causing a change in the RPC performance (decrease of detector efficiency as shown in Figure 5.3(b)) and a temporary increase of the HV working point of about 120 V to recover the standard operation conditions [60]. Similar problems have been observed also in few other systems.

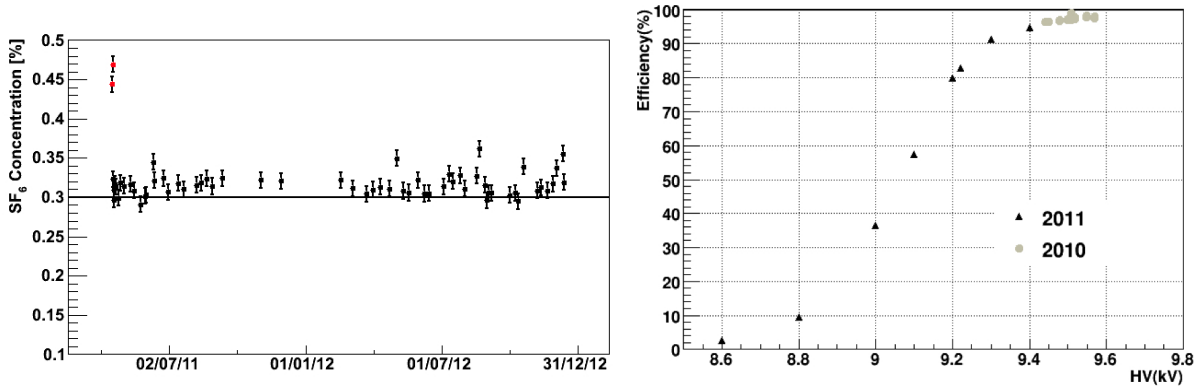

(a) (b)

Figure 5.3: (a) SF_6 concentration in the CMS RPC fresh mixture. The red dots are the data of April 2011 when a drift in the MFC flow was detected. (b) Mean efficiency of some CMS RPC detectors as a function of the applied voltage in 2010 and 2011. The 2011 data correspond to an increase of SF_6 (from 0.30% to 0.45%): an increase of about 120 V is necessary to operate at the same operation conditions.

This example shows the importance of periodic calibration campaigns for the MFCs. During LS1 most of the MFCs have been controlled and, in case of a deviation greater than 1% with respect to the foreseen value, a new calibration has been performed. Figure 5.4 shows the results obtained for several MFCs: important discrepancies were found especially for the high flow MFCs used during the detectors filling phase. Furthermore even if MFCs are extremely stable devices, they can suffer from the presence of impurities in the gas.

The low quality of the primary gas supplies is a critical issue: it happens very rarely but it can have a serious impact on detector operation [61]. The typical example is Air contamination, which can be present in all types of supplies. Usually the acceptable Air level is in the order of 100 ppm, however it can reach 7500 ppm in presence of faulty supplies. An abnormal presence of Air is undesired since it causes an increase of detector dark current (RPC) and it has an impact on gas gain and drift velocity (wire chambers). These changes affect detector calibration parameters and eventually time and spatial resolutions.

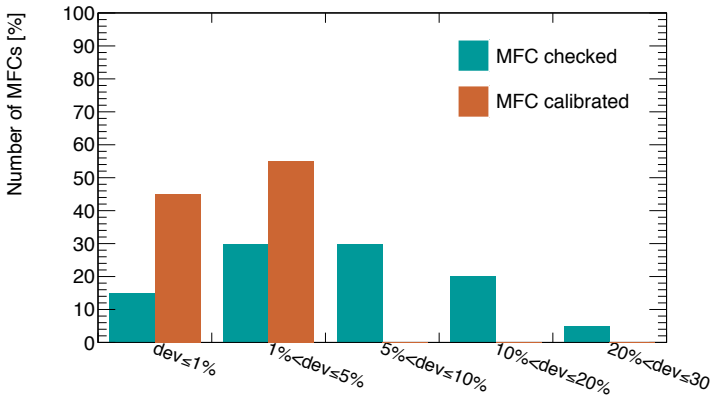

Figure 5.4: Deviation in percentage of the actual delivered flow with respect to the calibration before (blue) and after (red) the adjustment.

A more difficult case happened in LHCb for the GEM detector system, which works in open mode using an $Ar/CO_2/CF_4$ (45/15/40) gas mixture with a flow equivalent to about 7 chamber volumes per hour [62]. Figure 5.5 shows the correlation between the changeover of CF_4 cylinders and the gas gain fluctuation observed in the GEM detector. The gain fluctuations are in coincidence with changes in the CF_4 gas supplies even if not all changes affect the detector performance. The gain fluctuations are correlated with quality composition of the CF_4 gas supplies despite GC analysis have not revealed any presence of impurities at the level of about 10 ppm.

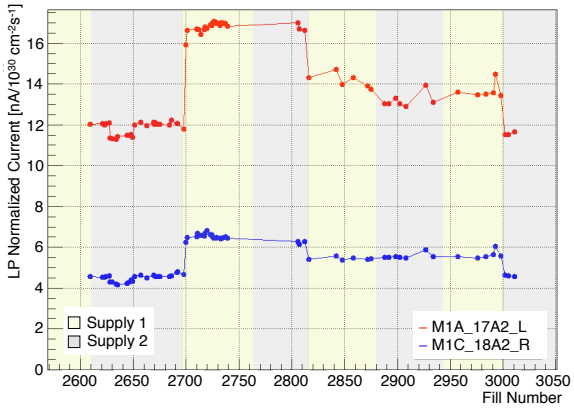

Figure 5.5: Luminosity-normalised average fill currents on two triple-GEM detectors during LHC fills in 2012. A current fluctuation of +40% is present in fill 2700 and of -20% in fills 2805 and 3000 [62]. The changeovers between the two CF_4 gas supply sides are indicated with the "Supply 1" and "Supply 2" bars. The current variations seem to be correlated with CF_4 bottle changes.

Several tests were performed on the LHCb GEM system to quantify the detector sensitivity to variations in the gas mixture composition. The effects of changes in the mixture composition have been verified by decreasing of 1% the CF_4 concentration and increasing of 1% the Ar and CO_2 concentration respectively. A gain variation of about $\pm 4.5\%$ is visible in Figure 5.6, which shows the current normalized to the luminosity for one GEM detector. Similar results

have been obtained for other GEM detectors, with a maximum gain variation of the order of 7%. A 1% variation in the gas mixture composition was also easily detected with the GC. A

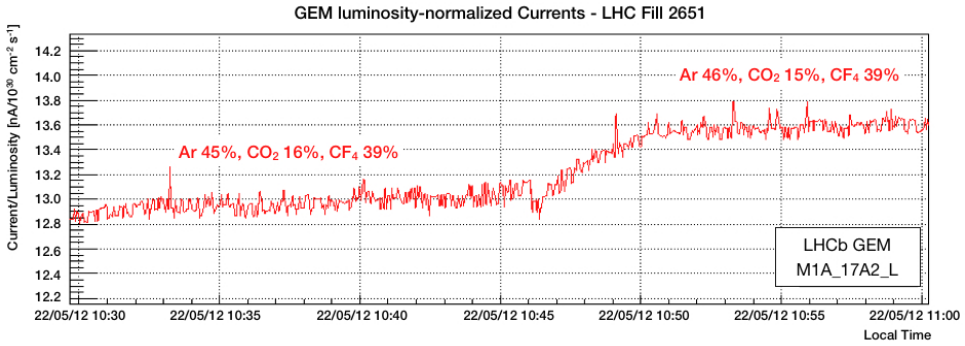

(a)

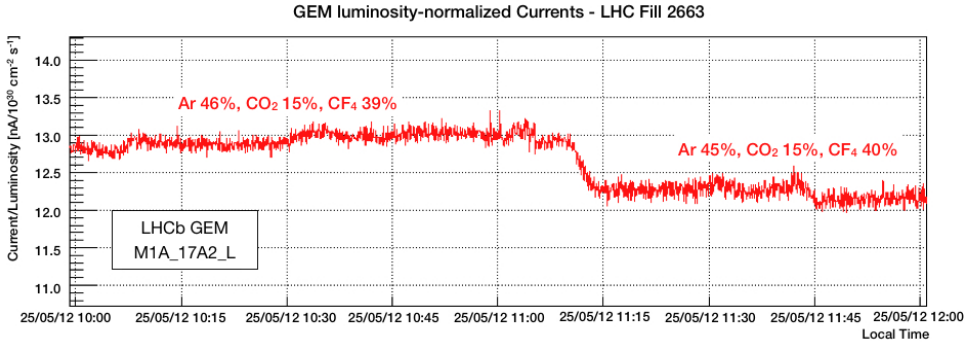

(b)

Figure 5.6: Gas gain variation during LHC run for a LHCb GEM detector related to a $\pm 1\%$ variation in the three gas mixture components [62].

second test was carried out to verify the overall quality of the supply cylinders: a modification on the GEM supply line allowed to operate one or both sides of the GEM system with premixed gas (leaving the other side on the standard gas system). In few occasions, both during technical stops and LHC run, half detector system was flushed with premixed gas mixture (with nominal composition). In the first case, no changes in the detector current were observed for both sides while during one LHC fill a sudden increase of gain of about 20% was detected in the half of the detector flushed with gas from standard supplies. GC analysis did not reveal any changes of the order of 100 ppm in the gas mixture composition. However the test demonstrated that the supply cylinders contained some impurities, which produced a change in the detector gain, without being visible with the standard chemical analysis. In these conditions, only monitoring systems based on detectors (for example SWPC) can allow to detect changes in the mixture with enough precision (Section 6.1).

5.4 Accumulation of impurities in gas recirculation systems

About 50% LHC gas systems are operated in gas recirculation mode, being mandatory in case of large gas volumes or expensive gas mixtures. The quality of the gas mixture can deteriorate in a closed loop system, especially impurities can accumulate because of radiation (inducing

high detector counting rate), leaks or gas contaminations coming from the gas system or the detectors themselves. Two methods can be used to reduce the presence of these impurities: the injection of fresh mixture in the CL and the use of gas purifiers.

The fraction of fresh mixture in a CL should be as small as possible. It is usually needed to compensate for leaks or to control the concentration of impurities that cannot be filtered (for example N_2). An example is the RPC systems where leaks are present at the detector level and new fresh gas has to be injected to compensate Air accumulating in the detector.

Systematic studies have been conducted on the impurities that can be created inside the RPC detector volume under the effects of high electric field and radiation [63], [64]. In these conditions, complex molecules can break creating ions and then new molecules accumulate in the CL. Figure 5.7(a) shows an example of the impurities created in a RPC detector under a gamma irradiation producing counting rate of about 100 Hz/cm^2. The addition of purifiers with different cleaning agents helps to reduce these impurities to a minimum level (Figure 5.7(b)).

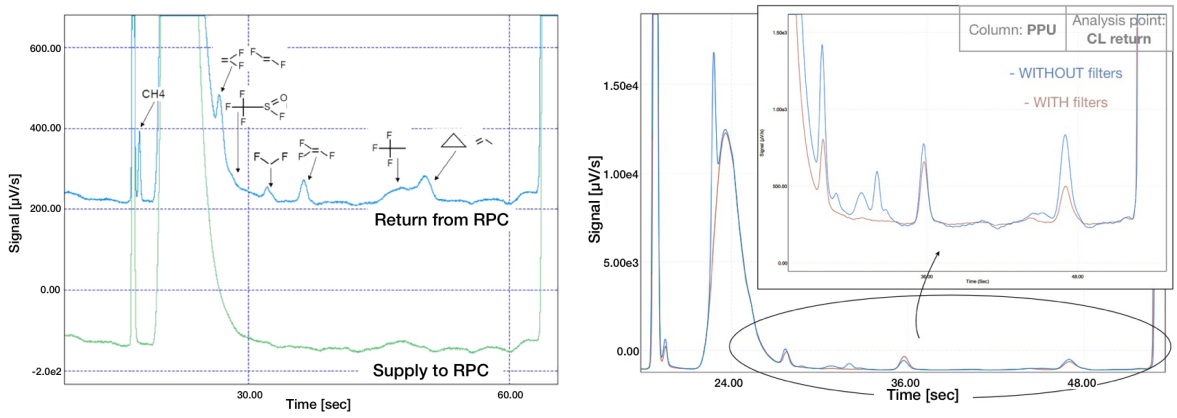

(a) (b)

Figure 5.7: Superimposed gas chromatograms of the RPC gas mixture in different analysis points: (a) the fresh mixture and the return gas from irradiated RPC or (b) the gas mixture in the CL with and without the use of purifiers. Several impurities are visible and have been identified with a Mass Spectrometer. Without purifiers the impurities concentration is higher and even new signals appear [64].

A different mechanism is responsible for the accumulation of O_2 and N_2 in the CMS CSC detector. In 2008, after few months of operation, GC analysis revealed a high Air concentration (greater than 2%) in the return gas mixture from the detectors. An extensive leak search campaign was performed confirming that both detectors and gas system were gas tight. Indeed, the source of contamination was eventually identified as due to diffusion through components used for the construction of the detector. GC analysis performed on all return lines allowed to identify the typology of detectors affected by the problem and finally the flow rate was adjusted in the system to maintain O_2 and N_2 concentration below required limits. O_2 is currently removed from the gas stream using a purifier module filled with Ni-Al_2O_3 catalyst while N_2 cannot be filtered and therefore it accumulates up to concentration of about 1% (in case of 90% gas recirculation). In this respect, the fresh mixture flow determines the N_2 concentration in the gas mixtures supplied to the detector that cannot be decreased to the leak level. The strategy adopted for reducing operational costs and gas emission (CSC mixture contains 10% of

CF_4, which is expensive and a greenhouse gas) is to recover the CF_4 from the exhaust of the recirculation system, as it will be discussed in Section 5.6.

Even if the use of purifiers is needed in a CL system, the cleaning agents can have collateral effects during operation as, for example, the absorption of one or more main components of the detector gas mixture. Figure 5.8(a) shows a typical problem at the beginning of the purifier cycle in a system flushed with Ar/CO_2/CF_4 (40/50/10) gas mixture: the CO_2 is almost completely absorbed for about one hour, destabilizing the mixture composition for that time. Cleaning agents can also release gases that are used during the regeneration. Figure 5.8(b) shows the release of Ar by several types of molecular sieves at the beginning of their operation. Moreover, in general, much gas is absorbed at the beginning of each run cycle producing a fast decrease of the pressure in the high pressure storage buffer and therefore destabilizing the full gas system. These problems can be overtaken modifying the standard operational sequence of the purifier module by adding two preparation phases at the beginning of the purifier cycle. The first preparation phase slowly brings the column pressure to the same level of the high pressure buffer in the gas system while the second preparation phase pre-saturates the cleaning agents in the column with respect to the mixture components. In total 21 purifier modules have been implemented in the gas systems of the LHC experiments and they perform according to expectations.

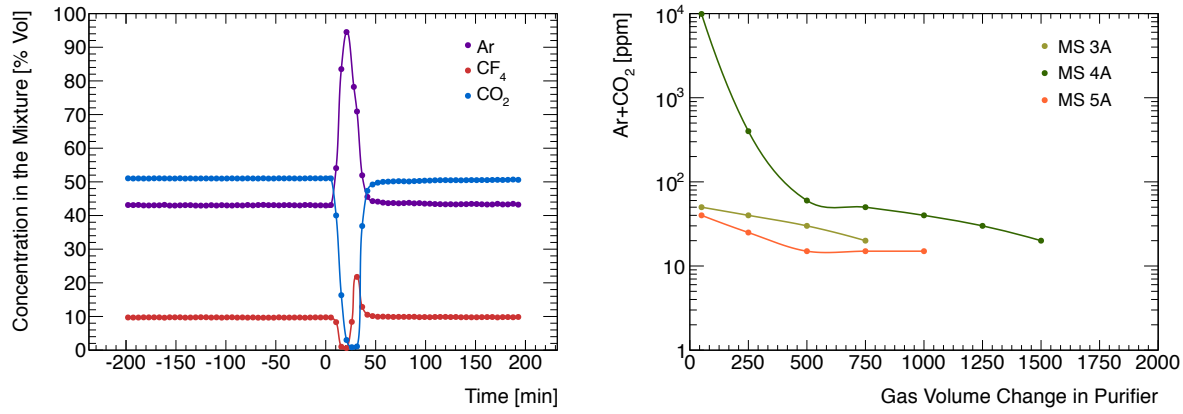

(a) (b)

Figure 5.8: (a) CO_2 absorption at the beginning of a purifier cycle. It is evident how the gas mixture ratios are completely destabilized during this phase. (b) Ar release during the first operation phase of a purifier. Ar is present in the material since it is used during the regeneration process.

5.5 The use of greenhouse gases for particle detection at LHC

The use of some greenhouse gases is necessary to achieve the required detector performance at the LHC experiments. Figure 5.9(a) shows their total fraction with respect to the total CO_2 equivalent: the main contributions are due to $C_2H_2F_4$, CF_4 and SF_6 having a GWP equal to 1430, 6500 and 23900 respectively. The reduction of emissions and operational costs is obtained operating the detectors in recirculation mode. However the recirculation efficiency depends on

the amount of leaks in the systems and on specific operation conditions. Figure 5.9(b) shows the fraction with respect to the total of the equivalent CO_2 emission for the gaseous detectors operated with different recirculation efficiencies. The main contribution is obviously coming from a recirculation lower than 90%. The gas emissions of recirculation systems account for 85% of the total CO_2 equivalent emission at LHC since these systems have the largest gas volumes.

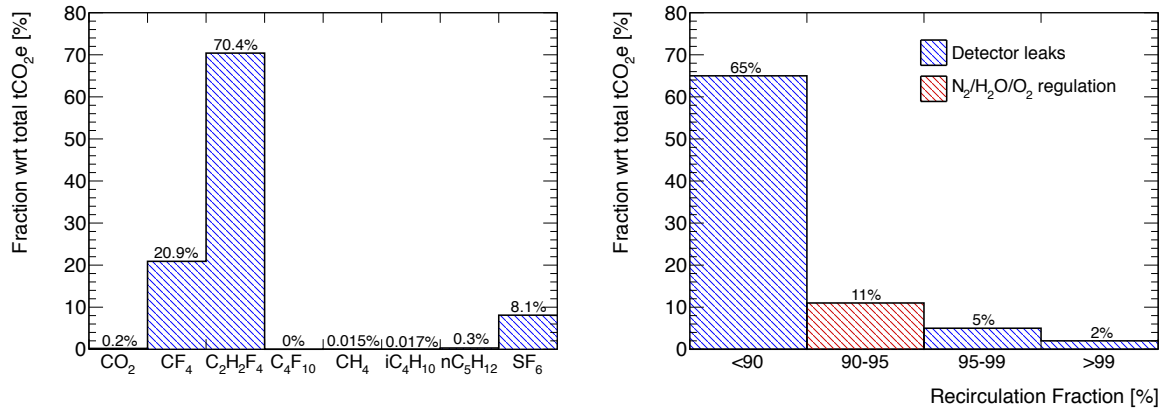

(a) (b)

Figure 5.9: (a) Relative contribution in terms of CO_2 equivalent from different gases used for particle physics detection at CERN. The dominant contribution is due to the $C_2H_2F_4$ used by the large ATLAS and CMS RPC systems. (b) Fraction with respect to the total of the equivalent CO_2 emission for the gaseous detectors operated with different recirculation efficiencies. Only a low contribution is due to the need to adjust the N_2 concentration in the gas mixture (in red).

Figure 5.10 shows an overview of the CO_2 equivalent emission for the most concerned LHC detectors and the expected reduction at the end of LS1. These detectors account for about 98% of the total emission where the main contribution comes from RPC ($C_2H_2F_4$, SF_6), followed by CSC (CF_4) and GEM (CF_4). The ATLAS and CMS RPC contribute to a large amount despite they are already operated in gas recirculation at the maximum possible level because of leaks present in the detectors. During LS1 several actions have been taken to reduce the consumption of greenhouse gases:

- An intense leak test campaign have been performed reducing the RPC leak rate by about 40%.
- The ALICE Muon Trigger (MTR) gas system has been upgraded from open to closed loop.
- The CMS CSC system has been complemented with a complex CF_4 recuperation plant, which allows to recuperate about 80% of the CF_4 present in the gas mixture that is sent to the exhaust line.

Beyond these improvements, several R&D projects have recently started to find less impactive gases in terms of cost and environmental effects. LHCb contributes to greenhouse emission with the use of CF_4 from GEM detectors, which use 45% of CF_4 in their gas mixture.

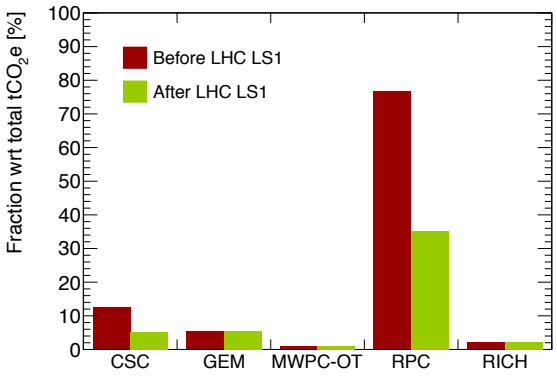

Figure 5.10: Overview of the greenhouse gas emission from the most concerned gaseous detectors at the LHC experiments. These emissions accounts for about 98% of the total detector emission at CERN. In green the expected reduction after the interventions scheduled during LS1.

LHCb GEMs are currently operated in open mode because they were considered a small system. Upgrade to gas recirculation is under evaluation (Section 6.2) and implementation will be done in the near future. A second example of strategy to reduce greenhouse emission concerns the R134a used in the RPC gas mixture as it will be discussed in Section 6.3. The procedure necessary for replacing a gas component in a particle detector is known to be a long and delicate process that may last for many years. Indeed, similar issues were already addressed in the past by the RPC community when it was needed to substitute R13B1, banned for its contribution to the depletion of Earth's atmospheric ozone layer. In this occasion, the validation process of the new gas mixture lasted for about 10 years [65]. While R&D activities are progressing, several mitigation actions can already be undertaken. In particular, the quantity of gas lost should be reduced by repairing as many as possible leaks. Also the research for advanced gas recuperation plants should be supported to build and operate such systems even if the initial capital investment is important (Section 5.6).

5.6 Example of gas recuperation: the CMS CSC CF_4 recuperation plant

The CMS CSCs are operated with a three component gas mixture: 50% CO_2, 40% Ar and 10% CF_4. The CF_4 prevents aging effects, such as the deterioration of the gas gain due to the formation of deposits on the anode wires produced by polymerization of impurities present in the gas mixture. Considering the very large detector volume (66 m^3) and the use of an expensive gas (CF_4), the CSC gas system is operated in recirculation mode. Nowadays the percentage of fresh mixture injected is set to 10% to cope with the detector permeability to Air (Section 5.4). CF_4 accounts for more than 90% of the total gas operational cost and therefore there is an obvious interest in recuperating this component from the gas exhausted.

The concept of a recuperation plant based on CF_4 warm separation has been considered as a first option with respect to CF_4 liquefaction for economical reasons. Extensive tests were per-

formed over few years on single elements and, finally, on a small scale prototype to validate the working principle [66]. During the years 2011-2012 the real plant was built and commissioned. It comprises five modules with specific functions. The first four modules are for the CF_4 recuperation, while the last one is used for the injection of the recuperated CF_4 in the gas mixture at the CSC mixer level. It was estimated that the plant cost should be paid back in 2-3 years of operation.

The CF_4 recuperation process is divided into four steps (Figure 5.13):

Phase 1: Membrane module for CO_2 bulk separation. The first step is to reduce the CO_2 concentration (50%) to a very low value (about 1%). This is achieved using a gas separation membrane, which consists of many thin straw tubes where the CO_2 can diffuse through the straw wall while the CF_4 pass through without interacting (Figure 5.11).

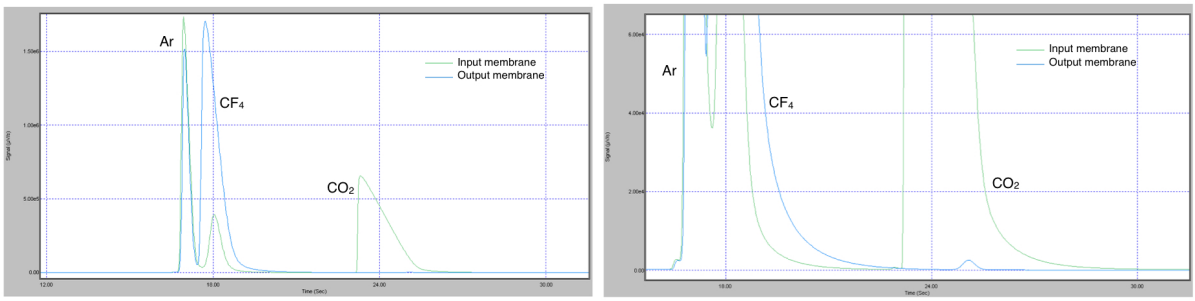

(a) (b)

Figure 5.11: (a) Comparison of the gas chromatograms at the input (green line) and output (blue line) of the membrane module. Most of the CO_2 has been absorbed. The mixture composition changes from CO_2/Ar/CF_4 (50/40/10) to CO_2/Ar/CF_4 (<1/60/40). (b) A zoomed view of the CO_2 peak: a small concentration of CO_2 is still present (< 1%).

Phase 2: Molecular Sieve 4 Å for CO_2 residual separation. The CO_2 has to be completely removed from the gas mixture to ensure a pure recuperated CF_4. A Molecular Sieve 4 Å cleaning agent[9] is used to absorb CO_2 efficiently without affecting the CF_4 component (Figure 5.12).

Phase 3a: Molecular Sieve 13X for CF_4 adsorption and recuperation. The gas exiting the MS 4 Å column is a mixture of Ar (65%) and CF_4 (35%), with some ppm of N_2. The mixture is sent to a second absorber module, filled with Molecular Sieve 13X (i.e. pore size is about 10 Å), which absorbs only CF_4 while Ar and N_2 remain volatile and are vented from the cartridge. The CF_4 is therefore absorbed and then extracted from the Molecular Sieve 13X pores.

Phase 3b: CF_4 compression and storage. After the CF_4 has been extracted from the cartridge, it is compressed and stored into a battery of 12 cylinders suitable for pressurized gas.

[9]Molecular sieves are micro-porous alumina-silicate used as commercial absorbers. The electrical charge interaction between the surface and the gas phase produces a Van der Waals force that retains some types of gas molecules. The Molecular Sieve 4 Å is expected to adsorb CO_2 efficiently without affecting the CF_4 component.

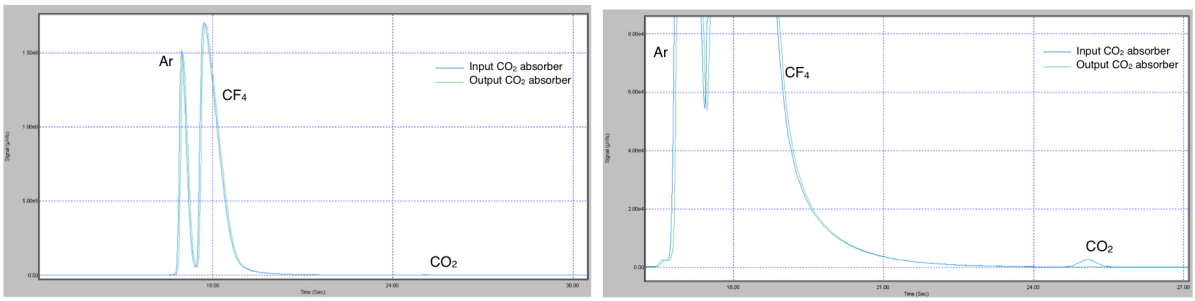

(a) (b)

Figure 5.12: (a) Comparison of the gas chromatograms at the input (blue line) and output (green line) of the CO_2 absorber module. The Molecular Sieve 4 Å does not absorb Ar and CF_4. (b) A zoomed view near the CO_2 peak: the CO_2 is completely absorbed by the purifier.

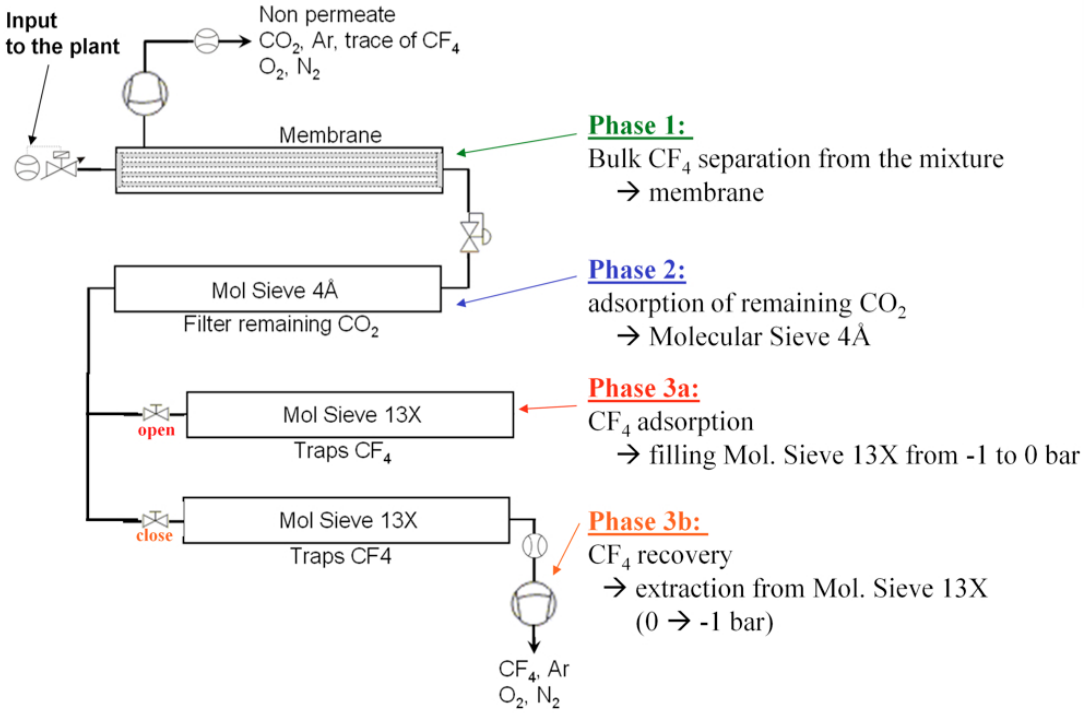

Figure 5.13: Overview of the different phases necessaries to separate the CF_4 from the CMS CSC gas mixture.

The end of the run cycle is set when the relative pressure inside the Molecular Sieve 13X cartridge is equal to zero or to the pressure in the supply line to the module. In this method the molecular sieve is not yet fully saturated and therefore CF_4 continues to be adsorbed until the end of the cycle, leaving only Ar in the empty space. Figure 5.14 shows the trend of the recovered gas during Phase 3a: at the start-up of the recuperation the CF_4 concentration is zero and rapidly increases only when the pressure in the cartridge is below -800 mbar. The main impurity contained in the recuperated CF_4 is N_2 with a concentration of about 0.5%, which results in 0.05% in the final gas mixture concentration.

The CF_4 recuperation plant is operational since June 2012. A total of about 100 m^3, which corresponds to a recuperation efficiency of about 70%, has been recuperated during LHC Run1

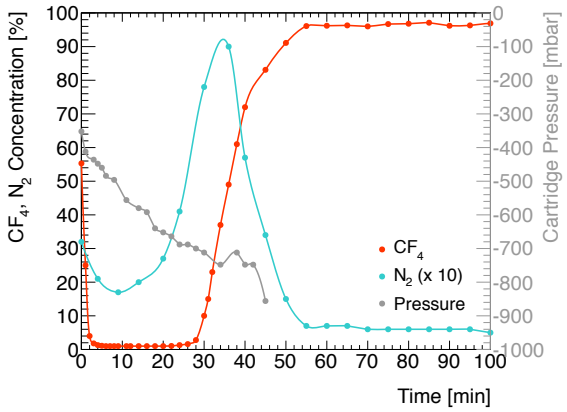

Figure 5.14: Composition of the recovered gas during the recuperation process of Phase 3a. At the beginning of the phase, the CF_4 concentration is equal to zero (only Ar is extracted from the empty spaces present in the molecular sieve) while after some time it reaches almost 100%. The N_2 concentration shows a peak after about 30 min and after it decreases to about 0.5%.

and at the beginning of LS1. The quality of the recuperated CF_4 has been analyzed with the GC: the CF_4 is pure at 90% with about 10% of Ar and few ppm of N_2. An additional MFC has been installed in the CSC mixer to allow the re-injection of the recuperated CF_4 in the gas system taking into account the Ar concentration [67]. During most of LS1 the CSC detectors have been operated with reduced CF_4 concentration to diminish the operational costs. Starting from October 2014, the CF_4 recuperated has been injected into the CSC gas system in a percentage of 5% and no change in the CSC performance has been observed, as it will be described in detail in Section 6.1.5.

5.7 Strategies for consolidation of gas systems and detectors working conditions at LHC

Gas mixtures and gas systems are key components for a successful operation of all gaseous detectors. This is particularly important at the LHC experiments where muon systems are expected to work for many decades with an always increasing particle rate. In this context, the monitoring of mixture composition and quality of gas supply are of primary importance, especially when gas recirculation or gas recuperation systems are used to contain operation costs and gas emissions. These implementations represent the current strategy to optimize the present systems ensuring reliable operation during Run 2 and future HL-LHC phase. However since greenhouse gases with GWP greater than 1500 will be banned in the near future, more drastic solutions are needed. Two R&D programs exploring new possibilities will be discussed in next chapter.

Gas recirculation and recuperation systems might lead to the accumulation of certain impurities, which require the presence of purifier modules together with the establishment of complex cycle parameters relying on gas monitoring tools for their measurements (Section 5.2). The use of several available analysis tools (O_2, H_2O analyzers and GC) has been discussed in this chapter together with their advantages and limitations. Only by merging the information

coming from different devices, a good understanding can be achieved. The present monitoring techniques show two main critical points:

- the sampling mechanism introduces a delay to the moment in which the information is available and therefore the potential problem can have already affected the detector gas volume;
- the gas mixture chemical composition is not always the best indicator. It is possible to have pollutants present in very low concentrations (< 1 ppm) that cannot be detected by standard techniques and can nevertheless dramatically affect the detector performance (i.e. impurities causing aging).

A complementary method, which overcomes these limitations, will be discussed in the next chapter. It consists of adding a monitoring Single Wire Proportional Chamber that allows to detect very low concentrations of impurities in a short time.

Chapter 6

Optimization of gas systems and gaseous detectors operation for the HL-LHC phase

As of today, the LHC muon system upgrades foreseen for the HL-LHC phase concern mainly the read-out systems and the addition of new detector stations. Therefore it is of crucial importance to maintain the existing detectors in good operation conditions and to avoid any possible source of damaging. As already discussed, one of the most crucial parameters is the gas mixture composition. In the previous chapter, advantages and limitations of gas monitoring tools used for the LHC gas systems have been discussed. A complementary solution, based on Single Wire Proportional Chamber sensitivity to gas mixture variations and presence of pollutants will be discussed in this chapter together with its applications at LHC experiments and R&D studies.

Beyond the gas mixture quality, the LHC gaseous detectors have to handle with the use of greenhouse gases. New detector technologies, which have been selected for the future upgrades, need to be validated for operation with gas recirculation. R&D studies addressing this topic for the specific case of large GEM detector systems will be discussed in this chapter.

The RPC community is facing a different issue: the R134a, which is the main component ($\sim$95%) of the RPC gas mixture, will be soon banned. The evaluation of detector performance with a new environmental friendly Freon will be here presented.

6.1 An online gas monitoring system for the LHC gas detectors

The monitoring of the gas mixture at LHC is usually performed with O_2 and H_2O analyzers as well as gas chromatograph when necessary. The GC cannot work continuously on one gas stream, i.e. each gas line is analyzed every few days for practical reasons. However for many gaseous detectors, a minimum variation in the gas mixture composition can cause a sudden degradation of their performance. The present study is motivated by the need of developing a system for continuos monitoring of the most critical gas streams. Single Wire Proportional Chambers (SWPCs) are used since they revealed to be extremely sensitive to standard impurities (O_2, H_2O, N_2, etc.) as well as specific chemical components not detected by usual analysis tools because of extremely low concentration (<1 ppm) and complexity [68], [69].

6.1.1 Principle of signal formation and gas mixture composition

In this section the working principles of SWPC and the guideline for the definition of the gas mixture will be briefly introduced [70], [71], [72]. In a SWPC primary electrons, created by the passage of ionizing particles, drift towards the anode wire under the effect of the electric field. Only when the electrons reach the region close to the anode where the electric field is very high they can gain enough energy to produce secondary ionization (charge multiplication process). The multiplication region is a very small volume close to the wire. For a cylindrical geometry, the electric field is given by

$$E\left(r\right) = \frac{V}{\ln\left(\frac{b}{a}\right)}\frac{1}{r} \tag{6.1}$$

where V is the applied potential, a is the anode wire radius and b is the cathode inner radius. The minimum electric field required to support avalanche formation is of the order of 10^5-10^6 V/m. Therefore, for a typical SWPC (V$\sim$2000 V, a$\sim$30 μm, b$\sim$30 cm), the multiplication region is less than 10 wire radii, i.e. only 0.1% of the total detector volume.

Single wire chambers are proportional counters. The signal collected is proportional to the primary ionization. The multiplication process is described by the first Townsend coefficient α, which is the number of electrons produced by a single electron traveling 1 cm along a uniform electric field. Conversely, α^{-1} is the electron mean free path for ionization in the gas. The ionization cross section has a maximum for electron energies around 100 eV for most gases. This energy is reached very close to the wire (tens of μm from the anode wire for anode voltages in the kV range) where the avalanche can start. Electron attachment typically starts at electron energies of 2-7 eV that occurs at about 1-2 mm from the wire.

The Townsend coefficient summarizes the effect of excitation and ionization cross-sections for electrons that have acquired sufficient energy in the field. It depends on the electric field E. For intense electric fields, like close to the anode region, it is possible to assume α directly proportional to E. Under this assumption the charge multiplication factor G can be written as

$$\ln G = \frac{\ln 2}{\ln\frac{b}{a}}\frac{V}{\Delta V}\ln\frac{V}{\ln\frac{b}{a}aE_{min}\left(\rho_o\right)\frac{\rho}{\rho_o}} \tag{6.2}$$

Since very often detectors are operated at atmospheric pressure and without temperature control, it is of particular interest the effect on the gas multiplication factor induced by small changes in the gas density. From 6.2 the following relation can be obtained

$$\frac{dG}{G} = -\frac{\lambda \ln 2}{\Delta V\, 2\pi\varepsilon_0}\frac{d\rho}{\rho} \tag{6.3}$$

which contains a linear dependency between G and T/p

$$G = A\frac{T_i}{P_i} + B \tag{6.4}$$

Equation 6.4 will be used in the following for temperature and pressure variation correction.

Charge multiplication is not only related to electric field, but also to the gas mixture used

to operate the detector. Indeed the gas mixture is the medium in which ionization, drift and amplification processes develop. Many gas mixtures are successfully used for wire chambers where it is often possible to find a noble gas (typically Ar) mixed with a quench gas (inorganic like CO_2 or organic like hydrocarbons). These mixtures fulfill the basic requirement of having the electron lifetime sufficiently long and to allow stable amplification process. Quench gases are needed because excited noble gases can only return to the ground state through emission of a photon. The minimum energy of the emitted photon is 11.6 eV for Ar which is well above the ionization potential for any metal constituting the cathode. Photoelectrons can therefore be extracted from the cathode and initiate a new avalanche. Moreover, ions of noble atoms will drift to the cathode and are neutralized by extracting an electron. The balance of energy is either radiated as a photon resulting in photoelectrons or by extraction of another electron from the cathode. All these processes result in delayed spurious avalanches. Even for moderate gains, the probability of these processes is high enough to create a permanent discharge. Weakly bound polyatomic molecules can absorb photons over a wide range of energies through excitations of rotational and vibrational levels. In conclusion, the addition of a quencher will allow the absorption of the photons, which is essential for high gain and stable operation. When possible organic quench gases are avoided since they are likely to produce long term worsening of the detector performance (aging).

Another important choice for the gas mixture concerns the drift velocity and its dependence on the electric field. For many applications is preferable to have high drift velocity (it improves time resolution) and stability regardless the electric field. Ar/CF_4 based mixtures fulfill these requirements. The high electron drift velocity in CF_4-based mixtures, which could also contain a large fraction of a gas without dipole or quadrupole moments (like Ar, Xe, CH_4, etc), is a result of two effects.

The electron drift velocity is a function of the electric field, the concentration and the momentum transfer cross section σ_m. The momentum transfer cross section for CF_4 has a very deep minimum of 1.1×10^{-17} cm^2 at electron energies of about 0.13 eV [73] as shown in Figure 6.1 (Ramsauer effect). Furthermore, the CF_4 rotational excitation cross section is small because of the absence of dipole and quadrupole momentums [74]. The large vibrational excitation cross section, which increases rapidly in the energy region around 0.15 eV [75], [76] leads to high energy losses of the electron. Moreover, the very strong inelastic scattering peaking at 0.25 eV keeps the electron energy low, slightly above the gas thermal energy. Therefore, the electron drift velocity is high only if electron energy is at the Ramsauer minimum. This effect exists also in other gases. However, it is not so pronounced because the inelastic scattering cross sections increase not so rapidly as in CF_4 when increasing the electron energy (see, for example, [78] and [79] for CH_4 and C_2H_6, respectively).

An addition of CF_4 to Ar results in cooling down the free electrons to energies near the Ramsauer minimum leading to a strong increase in the electron drift velocity [80].

CO_2, often used as a quench gas, has a large momentum transfer cross section (Table 6.2). Thus, an addition of this gas to a fast gas can result in a considerable change of the electron drift velocity. Furthermore, contaminants like N_2 and O_2 would only slightly change the drift velocity; while the presence of water vapor in a concentration of one part per thousand could result in a loss of the electron drift velocity by several percent.

Gases containing electronegative species (for example fluorine) are responsible of capturing

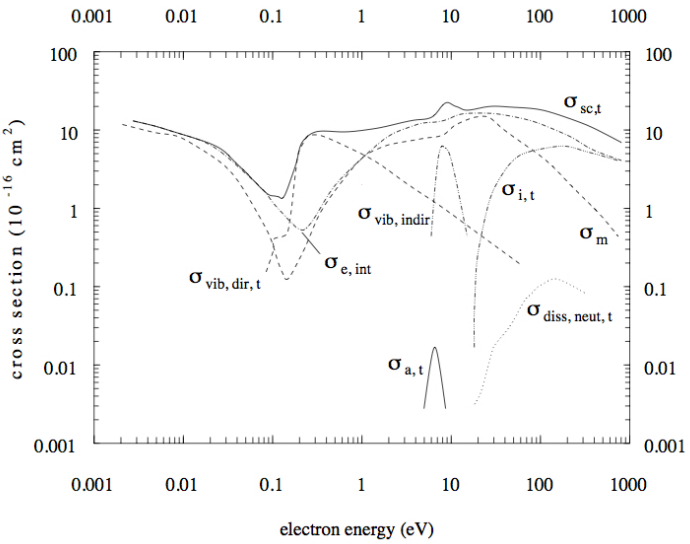

Figure 6.1: Electron impact cross sections for CF_4 [77] where $\sigma_{sc,t}$ is the total scattering cross section, σ_m is the momentum transfer cross section, $\sigma_{e,int}$ is the total elastic scattering cross section, $\sigma_{vib,dir,t}$ is the total cross section for vibrational excitation, $\sigma_{vib,indir}$ is the indirect electron scattering cross section through the negative ion resonances, $\sigma_{i,t}$ is the total ionization cross section, $\sigma_{a,t}$ is the total electron attachment cross section, $\sigma_{diss,neut,t}$ is the total cross section for production of neutral species.

Gas	$\sigma_{m,min}$ ($\times 10^{-17}$ cm^2)	ϵ (eV)
CF_4	1.1	0.13
Ar	1.5	0.3
Kr	6	0.6
Xe	15	0.7
CH_4	10	0.2
C_2H_6	10	0.13

Table 6.1: Momentum transfer cross section and electron energy corresponding to the Ramsauer minima in different gases. Gases H_2O and CO_2 are not presented here since the Ramsauer effect is not pronounced in them (the Ramsauer effect occurs when the molecules have zero dipole and quadrupole moments) [77].

Gas	Ar	CF_4	CO_2	CH_4	N_2	O_2	H_2O
$\sigma_m \times 10^{-17}$ cm^2	2	1.3	400	12	70	50	1700

Table 6.2: Momentum transfer cross sections of different gases measured at the electron-impact energy of 0.13 eV, the mean electron energy in the counting gas Ar/CO_2/CF_4 (65/5/30) at a distance of 2.5 mm form the wire [77].

free electrons, limiting the avalanche growth. This effect can be described by an effective ionization coefficient α_N = α-η, where η is the probability of attachment per unit length.

6.1.2 Experimental set-up

Single Wire Proportional Counter (SWPC) is the simplest gaseous detector geometry: a radial electric field created by a wire under voltage ensures the conditions for the avalanche process to start in presence of ionization from a particle passing in the gas volume. The SWPC geometry as well as the electronics to acquire the signal are usually very simple. The relatively simple design and their high sensitivity to any type of pollutants make SWPCs very attractive for mixture monitoring purpose.

The detector chosen for this study is shown in Figure 6.2. The main body and the detector's windows are made in stainless steel 316L. The configuration of the electric field and the large active volume are optimized for studying break-up and polymerization processes. Indeed the detector's geometry offers a large drift region where pollutants can effectively act through electron attachment, dissociative processes or catalytic behavior, giving a very sensitive detector to impurities. The wire material and diameter can be freely chosen. During the present study a 30 μm diameter Tungsten Au-plated wire is used since the Au layer ensure a good chemical stability with respect to most chemical reactions. Two 25 μm thick stainless windows are used to seal the chamber allowing radiation to pass through. The high voltage feedthrough needed to ensure the electrical insulation between the wire and the main body of the detector are specifically designed for the geometry used. They are glass caps with inside a Kovar[1] tube where the wire passes through and it is fixed by clamping the two pins at the extremities. The gas tightness of the detector is assured by custom-made "helicoflex" gasket inserted between the main body and the windows as well as by glue deposition around the pin where the wire is clamped. The use of glue represents the most critical step. Indeed glues can potentially outgas organic chemical components that are then in direct contact with the gas mixture. Since the outgassing components are often responsible for worsening the detector performance, the selection of the glue is of vital importance. In this specific case, an epoxy glue (AW106+HV953U) has been selected from literature [81] and re-validated in the present set-up. A dedicated box allows to supply the high voltage (HV) and to read the electrical signal from the wire.

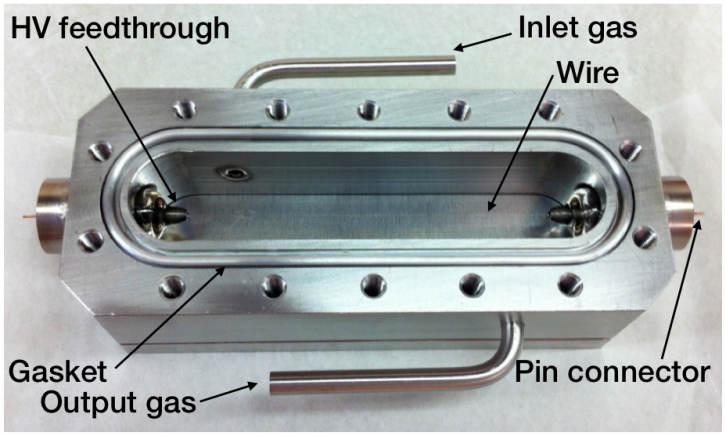

Figure 6.2: Photography of the SWPC used for the gas monitoring with highlight on the main components.

[1]Kovar is a Nickel-Cobalt ferrous alloy designed to be compatible with the thermal expansion characteristics of borosilicate glass. It allows direct mechanical connections over a large temperature ranges.

The SWPC is irradiated with a ^{55}Fe radioactive source having an activity of about 1 MBq and a round shape of 2 cm diameter. The radioactive source can be placed along the SWPC in five different positions (Figure 6.3) allowing to irradiate different areas of the wire. ^{55}Fe decays in ^{55}Mn emitting 5.9 keV photons. The ^{55}Fe pulse height spectra, as well as the anode current, are recorded every hour.

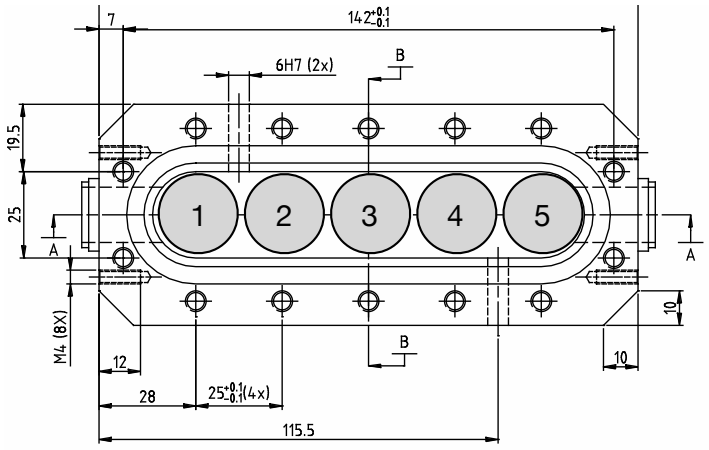

Figure 6.3: SWPC sketch with the possible position of the ^{55}Fe source along the wire length.

The signal produced by the SWPC is amplified into two different stages and it is digitalized using a multichannel analyzer (CAEN Waveform Desktop Digitizer DT5724[2]). A C++ based software has been developed for the data acquisition and analysis. The DAQ system records also environmental parameters (temperature and atmospheric pressure) as well as several gas parameters: detector operation pressure, mixture composition, gas flow, O_2 and H_2O concentrations.

Several gas mixtures have been used to characterize the SWPC. The basic gas mixture is 70% Ar and 30% CO_2. CF_4 has been added in several concentration to test the feasibility of using SWPC as gas monitoring tool for gas mixtures containing CF_4.

Preliminarily to any study about detector aging, it is mandatory to build a test set-up demonstrating stable detector performance. This step can be achieved selecting only extremely clean components. The gas system has been built with certified clean gas components[3]. A premixed bottle has been used to minimize the complexity of the gas system limiting the number of components used. Ar/CO_2/CF_4 (45/15/40) gas mixture has been chosen because it is the standard for operation of GEM detectors, which offered the possibility of an immediate application of the present study (Section 6.2). SWPC has been irradiated using a ^{55}Fe radioactive source with an activity of about 1 MBq for about 10 mC/cm of integrated charge[4], recording the pulse-charge

[2]The DT5724 is a 4 Channel 14 bit 100 MS/s Desktop Waveform Digitizer with 2.25 Vpp single ended input dynamics on MCX coaxial connectors.

[3]The pressure reducer and the rotamer have been O_2 degreased while stainless steel pipes and connectors have been washed in an ultrasonic bath and then rinsed with demineralized water.

[4]The expected accumulated charge for detector operated at LHC depends on their position in the experiment. For example in barrel detectors the integrated charge over 10 LHC years is between 50 and 500 mC/cm while in endcap detectors is in general at least a factor 10 higher. The present test is aiming in identifying detectors able to

spectrum and all the parameters that can affect the detector behavior. The pulse-charge spectrum remains stable overall the working period (Figure 6.4) demonstrating that the detector and the gas system do not contain components that could affect its performance.

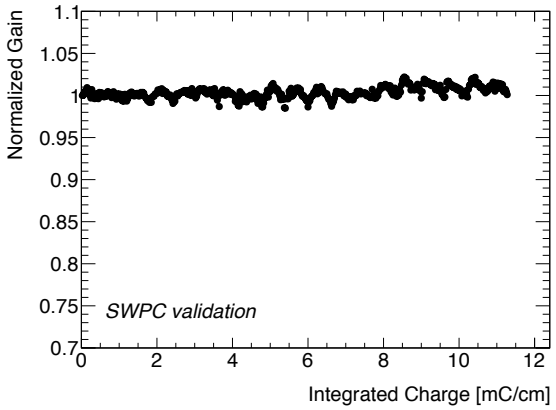

Figure 6.4: Normalized gain as a function of integrated charge for a SWPC working with a gas mixture of Ar/CO_2/CF_4 (45/15/40).

6.1.3 SWPC behavior with variations in gas mixture concentration

SWPCs have been tested with different gas mixtures and in presence of standard pollutants, as O_2 and H_2O, to quantify their sensitivity. The basic gas components for many detector systems at LHC are based on a noble gas and CO_2, with the exception of RPC and Cherenkov detectors. Two Ar/CO_2 mixtures as well as mixtures with the addition of CF_4 have been studied. The efficiency curves as a function of the high voltage are shown in Figure 6.5(a). A 15% increase of CO_2 in Ar/CO_2 mixtures produces an increase of about 300 V in the working point; indeed CO_2, being a quench gas (Section 6.1.1), absorbs photons limiting secondary avalanches. The addition of CF_4 to the mixture leads to a further increase in the HV working point since the electron impact inelastic cross section in CF_4 is higher than in Ar (this is due to the high electronegativity of fluorine atoms, which capture electrons limiting the avalanche growth). Figure 6.5(b) shows the gas multiplication factor obtained using different gas mixtures. The full efficiency is usually achieved at a gas gain of about 10^4.

The SWPC charge-pulse spectrum is used to verify and quantify the detector performance. Figure 6.6(a) shows an example of a charge-pulse spectrum of a SWPC operated with an Ar/CO_2 (70/30) gas mixture. The main peak is given by the 5.9 keV photons while the smaller one is the Ar escape peak[5], located at an energy of about 3 keV. The mean of the spectrum's main peak, which is proportional to the SWPC effective gain, moves depending on temperature and pressure variations (equation 6.4) as it is visible in Figure 6.6(b). For the following experimental

spot aging effects due to the presence of tiny concentration of impurities (below 1 ppm) and not to validate detector operation for LHC conditions.

[5]If the energy of the incoming X-rays is greater than the absorption edge of the detector gas, it can produce characteristic X-rays from the gas and produce what is termed an escape peak. For example, E_c for Ar is 3.2 keV and any X-rays with higher energy can excite Ar-Ka X-rays (E = 2.95 keV). The production of characteristic X-rays from the gas decreases the apparent energy of the incident X-ray and yields a separate peak offset towards lower energy by 3.2 keV.

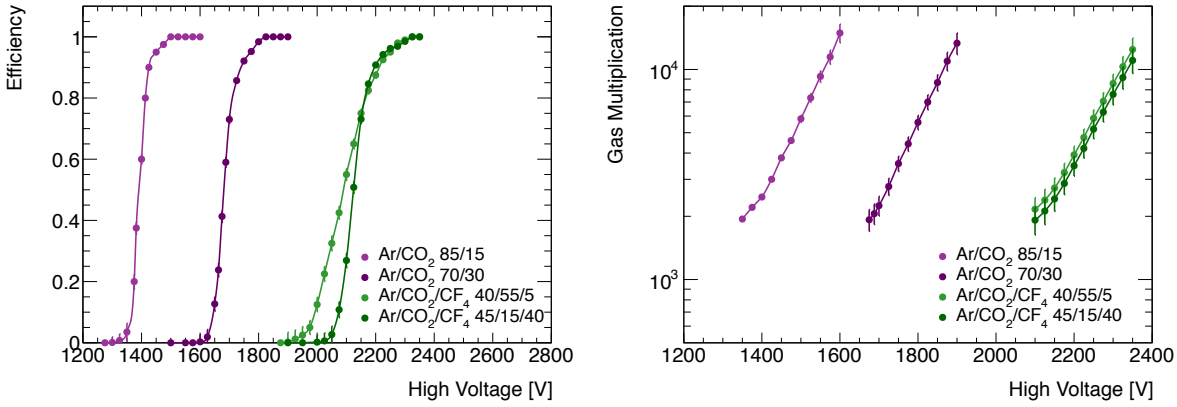

(a) (b)

Figure 6.5: SWPC (a) efficiency and (b) gas multiplication factor for two gas mixtures.

results, the mean peak value and the gain are always corrected by temperature and pressure fluctuations.

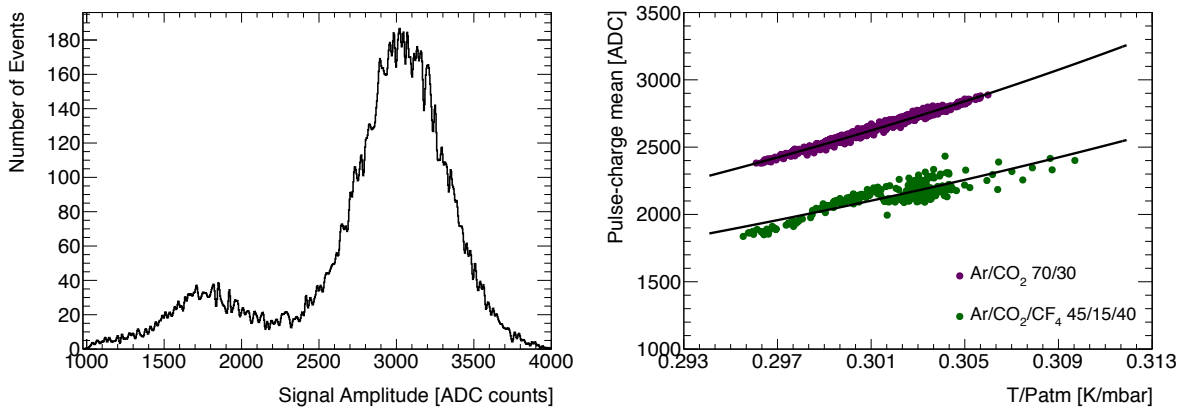

(a) (b)

Figure 6.6: (a) Charge-height spectrum of a SWPC operated with an Ar/CO_2 (70/30) gas mixture. (b) Means of the pulse-height spectrum for a SWPC as a function of T/P for two gas mixtures.

The sensitivity of SWPC to small changes in the gas composition has been studied for $Ar/CO_2/CF_4$ (45/15/40) gas mixture, varying the CF_4 concentration and maintaining constant the Ar/CO_2 fraction as well as the applied HV (Figure 6.7(a)). The mean of the pulse-charge spectrum decreases with the increase of CF_4 concentration since CF_4 is an electronegative gas, which captures free electrons and reduces the number of primary electron-ion couples. The energy resolution[6] remains basically constant. The parameters of the linear fit in Figure 6.7(a) allow to quantify the SWPC sensitivity to small variation of the CF_4 concentration. A variation of $\pm 1\%$ of CF_4 implies a change of about $\pm 3\%$ in the average pulse charge. Deviations of about 0.1% of CF_4 concentration are still detectable with the present system.

[6]The energy resolution is defined as the Full Width at Half Maximum (FWHM) of the spectrum divided by the mean value.

SWPCs are also very sensitivity to the presence of O_2 and H_2O in the gas mixture. Figure 6.7(b) shows the signal variation and energy resolution as a function of the O_2 concentration for a SWPC operated with Ar/CO_2/CF_4 (55/40/5) gas mixture. Being also O_2 an electronegative gas, it partially acts as CF_4 resulting in a decrease of the pulse-charge. In addition, the higher electron impact cross section for O_2 (Table 6.2) is the cause of a higher SWPC sensitivity to this gas. A variation of 100 ppm implies a decrease of about 7.5% of the pulse-charge mean value.

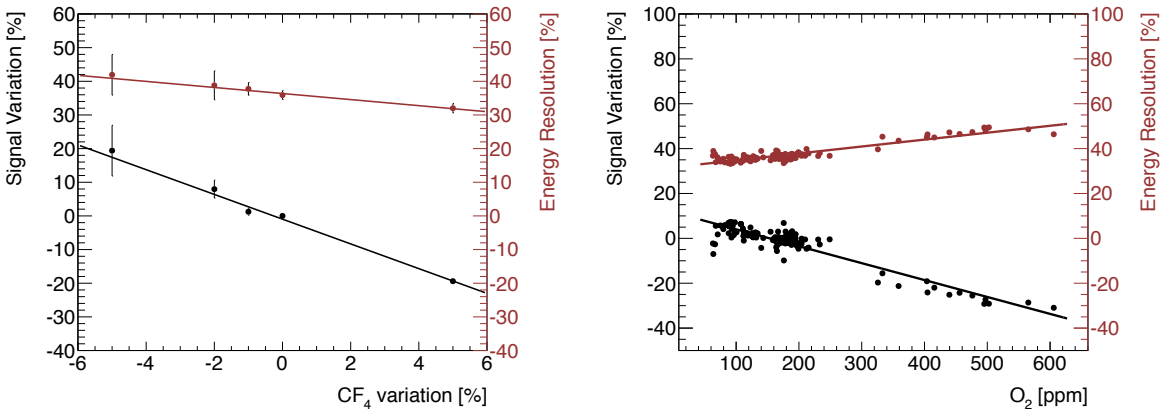

(a) (b)

Figure 6.7: (a) Pulse charge spectrum mean and energy resolution for SWPC as a function of CF_4 variation considering Ar/CO_2/CF_4 (45/15/40) as the base gas mixture (CF_4 variation equal to zero) and at constant electric field. (b) Signal variation and energy resolution of SWPC spectrum as a function of O_2 concentration for Ar/CO_2/CF_4 (55/40/5) gas mixture considering 150 ppm as the reference O_2 concentration.

6.1.4 SWPC behavior in presence of impurities

SWPCs are also very sensitive to the presence of pollutants, which can be released by external components (for example parts of the gas systems) or by the detector material itself. These pollutants can drastically affect the detector operation eventually leading to irreversible worsening of its performance. Systematic studies have been conducted to qualify gas system materials and glues used for sealing the SWPC.

Effects of detector assembly material outgassing

In the SWPC used for these studies between the pins and the internal Kovar tube of the HV feedthrough there is only a metal-metal contact that cannot ensure leak tightness (Figure 6.2). Usually an epoxy glue is applied to close these channels. Two different materials, which are already known to outgas, have been tested to quantify the aging effects and to be a reference for future studies: the epoxy glue Araldite AW103 with the hardener HY991 and a soldering paste Sn/Pb+Ag without flux. Figure 6.8 shows the trend of the normalized gas gain as a function of the integrated charge for the two materials. In the case of AW103+HY991, the gas multiplication is stable up to an integrated charge of about 0.5 mC/cm. After, the gain decreases suddenly by about 20% and then it stabilizes. The gain drop is caused by the outgassing of epoxy glue,

which releases pollutants inside the detector gas volume. The SWPC is left under irradiation for a period equivalent to 3 mC/cm integrated charge. The radioactive source is then moved to a different position along the wire (position 4 in Figure 6.3). As it happened before, after an integrated charge of 0.5 mC/cm, the gain starts to decrease until a stable normalized gain of 0.9 is reached. The lower gain drop can be explained with the decrease of the epoxy glue's outgassing. The movement of the radioactive source to two different wire positions demonstrates that radiation is needed to accelerate aging phenomena (in this case an accumulated charge of 0.5 mC is enough to see the aging effects). A similar test has been performed for the soldering paste (Figure 6.8(b)). The gas gain starts to decrease after an integrated charge of about 1 mC/cm until a stability is reached at a normalized gain of 0.8. In this case, the radioactive source is moved to the bottom of the SWPC[7] and the normalized gain does not restore demonstrating that the radioactive source position with respect to the wire sides does not have an influence.

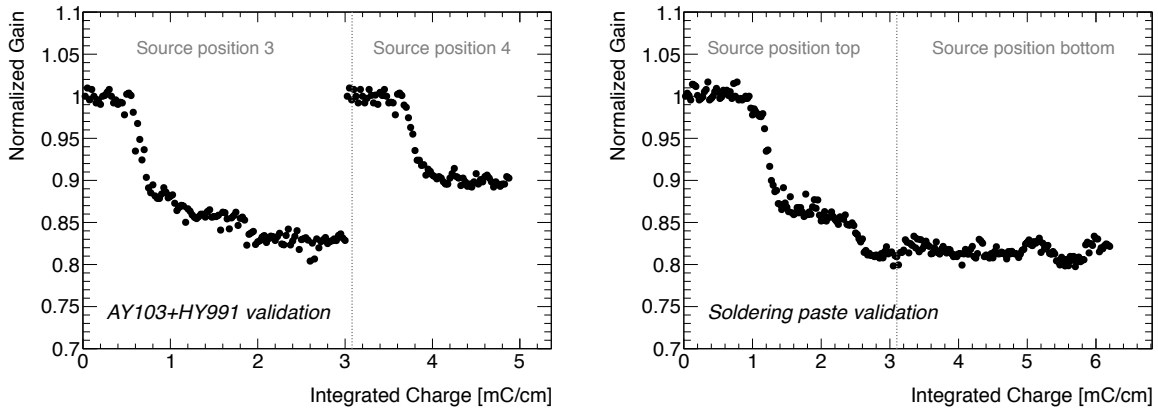

(a) (b)

Figure 6.8: Normalized gain as a function of integrated charge when the (a) glue Araldite AW103-1 with the hardener HY991 and the (b) soldering paste Sn/Pb+Ag without flux are used in the SWPC.

Figure 6.9 shows the pulse-charge spectra respectively at the beginning of operation, during the gain decrease phase and when a normalized gain of 0.8 is reached. The first pulse-charge spectrum has the well-known Gaussian distribution shape while the second spectrum shows a first indication of aging effect with the deterioration of the resolution as well as the shift of the main peak to lower values. When the aging process carries on, an asymmetry in the pulse-charge distribution appears due to the development of a second peak at lower charge with respect to the initial main peak. The charge difference between the two peaks could also increase with further irradiation. When the radioactive source is moved in a different position along the wire, the pulse-charge distribution is restored to the gaussian shape.

As expected, the aging effect is localized to the portion of wire irradiated. It is easy to argue that the gain drop is induced by a change of the wire diameter through deposition of pollutants. The presence of a second peak in the pulse-charge distribution is caused by a non uniform covering of the anode wire surface. Furthermore, the contaminant layer could affect the gas gain through an increase in the surface resistivity of both anode wire and cathode (Malter effect).

[7]The SWPC has two windows, allowing radiation on both side of the detector.

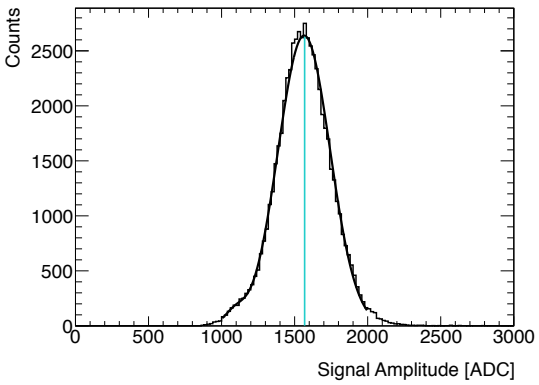

(a)

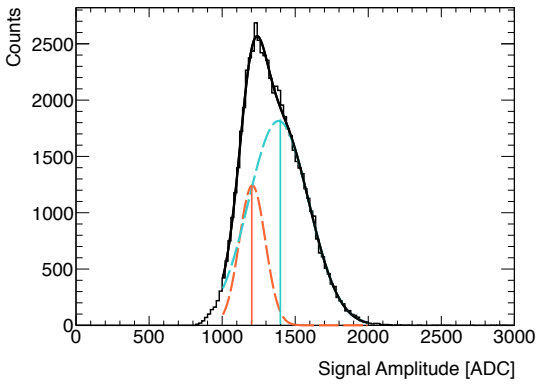

(b)

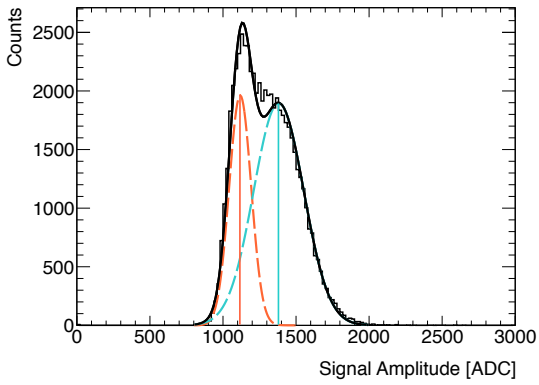

(c)

Figure 6.9: Evolution of the pulse-charge spectrum during aging process.

The aging tests with the Araldite AW103 and the soldering paste demonstrate the sensitivity of the SWPC to the minor presence of pollutants and allowed to quantify the effects. Aging appears only after a couple of days of operation when an integrated charge of about 0.5-1 mC/cm has been accumulated. The gas gain loss observed is about 20-25%, after which a stable operation is achieved. The effects of the movement of the source along the wire denote how the aging process in the SWPC affects only the irradiated area.

After the aging validation test, a two component epoxy paste adhesive, namely AW 106 with the hardener HV 953U (also known as Araldite 2011), has been tested for the application around the pin connector since it is known to not produce outgassing from previous studies [81]. The SWPC does not show any sign of aging after an accumulated charge of 20 mC/cm demonstrating the high reliability of this component for gaseous detector construction.

Qualitative analysis with scanning electron microscope (SEM) and energy-dispersive X-ray spectroscopy (EDS) detector have been performed on the wire and cathode window of the SWPC tested with the Araldite AW103+HY991. A new clean wire has been used as reference. A detailed observation at high magnification has been performed along the entire wire length. In the two sites exposed to the ^{55}Fe radiation (source positions 3 and 4 in Figure 6.3) several areas with a different surface tomography with respect to the overall wire surface were found (Figure 6.10).

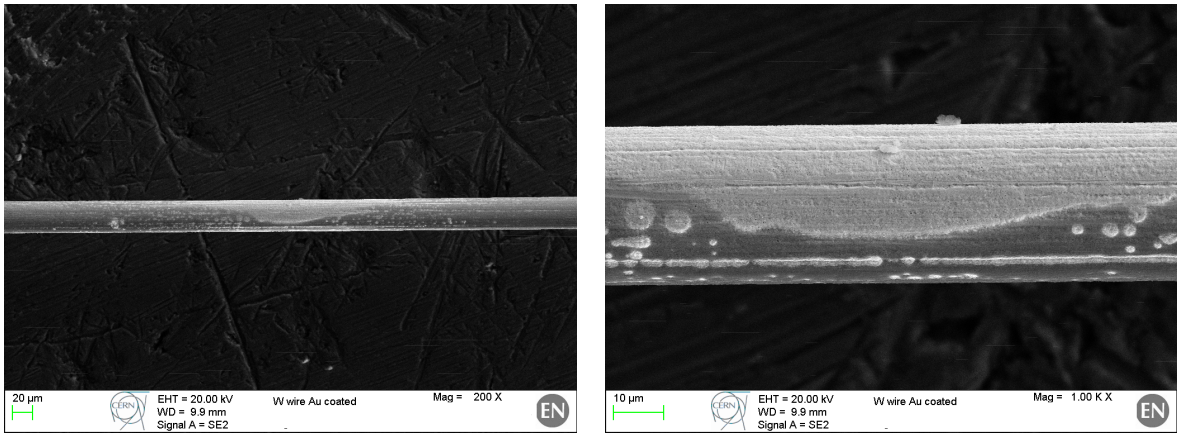

(a) (b)

Figure 6.10: SEM images at (a) 200 x and (b) 1000 x for a zone of the wire located in position 3. The bright area is mainly Au while the dark area is a carbon layer. The bright area spot has a dimension of about 100 μm and it corresponds to the irradiated area [82].

The SEM and EDS analysis on the SWPC wire revealed the presence of a uniformly distributed pollution of carbon with presence of fluorine along all wire except in the irradiated areas where the EDS analysis is very similar to the one performed on the clean reference wire (Au coated W wire). The SWPC wire diameter has been estimated to be about 31 μm where the carbon deposit is present and 30 μm in the irradiated area (the diameter of the reference clean wire is 30 μm). The pollution along the wire has been created by the outgassing of the epoxy glue as it was already found in [83]. On the contrary, in presence of radiation, the CF_4 acts as an etching additive removing the deposition of contaminants.

The inner part of the SWPC cathode window presented white areas, as shown in Figure 6.11. The chemical composition has been studied by EDS analysis and compared with a reference analysis of a clean region. EDS analysis on clean region matches the expected composition (stainless steel 316L) while the EDS analysis in the polluted area shows traces of Potassium and Zinc, probably due to the presence of these materials in the cleaning bath used to wash the detector components after machining.

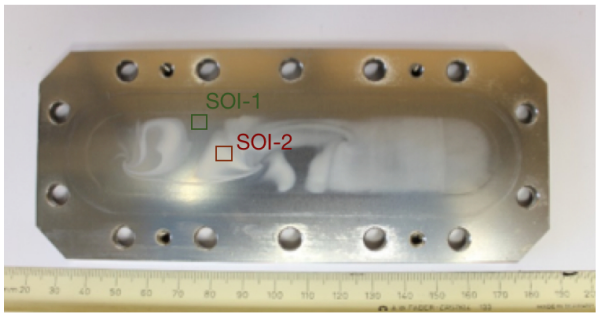

Figure 6.11: Visual appearance of the SWPC window surface and location of the sites of interest (SOI) where EDS analysis have been performed.

The deposits found on both anode and cathode of SWPC have been created during the avalanche process. Indeed, the aging phenomena are very complex physical and chemical

processes involving a huge variety of variables as the cross-section, the electron and photon energies, the electrostatic forces, the dipole moments, the chemical reactivity of atoms and molecules, etc. The plasma chemistry is usually considered as a starting point to explain aging processes. However, similarity between plasma chemistry and avalanche process are most often qualitative.

Effects of gas system components

The detector materials are not the only elements that could affect the detector operation. The gas system plays an important role since it could deliver a wrong gas mixture as well as release different types of pollutants. The clean gas system used for the previous tests has been modified inserting a not-degreased flowmeter in the gas stream line going to the detector. In these conditions, the SWPC has been irradiated with the source in position 3 (Figure 6.12). The gas gain starts to decrease after an integrated charge of 0.5 mC/cm until a stable normalized gain is reached at 0.7. The gain drop is caused by the insertion of the not-degreased flowmeter that releases impurities. If this flowmeter is substituted with one degreased and the source is moved to a different position along the wire not affected by the aging, the gas gain stays stable at its initial value. The test is useful to demonstrate the importance of having a clean gas system and it can be reproduced to evaluate each gas system component that has to be installed in the LHC experiments.

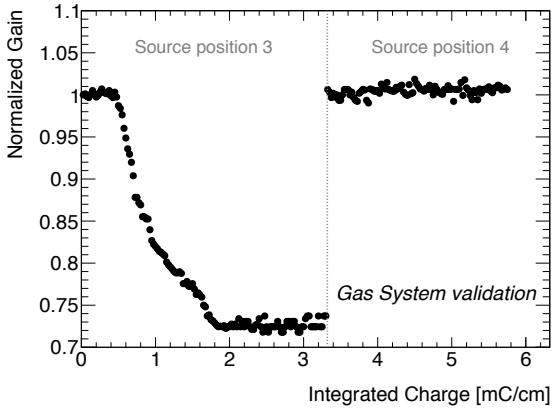

Figure 6.12: Normalized gain as a function of integrated charge during the test of a gas system component (a not-degreased flowmeter). The SWPC has a gain drop due to pollutants released by the flowmeter. The test has been stopped and the not-degreased flowmeter has been replaced with a degreased one. The source was then moved to position 4 and no gain loss is observed.

Summary of processes leading to aging phenomena

The typical physical processes that play an important role in the aging phenomena are [77]:

Production of photons Photons are responsible for the secondary electron emission processes. The typical processes responsible for the photon production are electron-atom collisions in the avalanches ($e^- + A \rightarrow e^- + A^* \rightarrow e^- + A + \gamma$), positive ion-electron recombination at the cathode ($A^+ + cathode\,(e^-) \rightarrow A + \gamma$) and positive ion-electron recombination in the avalanches ($e^- + A^+ \rightarrow A^* + \gamma$).

Secondary electron emission The secondary electron emission processes are responsible for the creation of positive feedback mechanisms and avalanche growth. Their typical examples are photons producing secondary electrons through photoelectric effect, avalanche photons interacting with the gas as well as the Malter effect [84].

These two mechanisms can cause several processes in the gas volume:

Dissociation Dissociation refers to the formation of molecular fragments under the impact of electron, photon or heat. In a typical avalanche process, electrons and photons have enough energy to break the typical molecular bonds.

Polymerization Plasma polymerization refers to the formation and deposition of polymeric material under the influence of a plasma. The reactive species formed by dissociation propagate into the volume where monomers are added to a growing polymer chain and then two radicals combine. The radicals do not carry net electric charge, they often have large dipole moment, are attracted by electrodes and they are chemically very active. The polymers are usually resistant to most chemicals and have excellent adhesion to surfaces.

Etching Etching refers to a complex set of chemical process in which gas-phase species react with a substrate to form volatile products [85], [86].

Considering the gas mixture used for the SWPC, some qualitative information on the possible reactions occurred during operation can be extracted. Ar and CO_2 do not produce polymerization unless a hydrocarbon contamination is present. On the contrary CF_4 can play an important role both in the polymerization and etching starting from the dissociative attachment via the following processes

$$CF_4 + e \rightarrow CF_3 + F^- \tag{6.5}$$

$$CF_4 + e \rightarrow CF_3^- + F \tag{6.6}$$

occurring with approximately equal probability and from dissociative ionization:

$$e + CF_4 \rightarrow 2e + CF_4^+ \rightarrow 2e + CF_3^+ + F \tag{6.7}$$

Other processes can occur in presence of CF_4 as the reaction of HF when water or hydrocarbons are present or resistive metal fluorides on nearby electrodes, making a very complicated chemistry. Nevertheless, according to plasma chemistry, CF_4 is an excellent etching additive and therefore it should help to remove possible polymerization deposits. Also O_2 can produce etching through formation of O_3.

O_2 and H_2O, which are usually present in the gas mixture as contaminant (with concentration of hundreds ppm), can start new processes. The attachment of electrons to free molecular oxygen, which is a high electro-negative gas, is described by two processes: two-body and three-body attachment. In the first case, the reaction is

$$e^- + O_2 \rightarrow O_2^{-*} \rightarrow O + O^- \tag{6.8}$$

having an electron threshold energy of 3.6 eV. In case of lower electron energies other mechanisms are available where the excited oxygen molecule can de-excite by exciting a third body or transfer the release energy kinetically. O_2 usually reacts with hydrocarbons and end products can be CO, CO_2, H_2O, H_2, which being stable and volatile are not responsible for polymeric layer formation. In presence of CF_n components (n=1, 2, 3), the O_2 can increase the fluorine production as [87]:

$$CF_n + O_2 \rightarrow \left\{ \begin{array}{c} COF_2 \\ CO \\ CO_2 \end{array} \right\} + F,\ F_2 \tag{6.9}$$

where, for example, CO and CO_2 are removed by gas flow. H_2O can limit the Malter effect by increasing the cathode surface conductivity. H_2O does not polymerize and its large dipole moment cools electrons with less than 1 eV. However, in presence of fluorine, the following reaction can occur

$$H_2O + F \rightarrow HF + OH \tag{6.10}$$

and even if hydrofluoric acid (HF) itself is not very reactive when reacting with H_2O, it is responsible in general for etching, in particular towards glass material (if present in the detector).

The present study allowed to reproduce and quantify aging processes due to known problematic components as well as to build a clean and sensitive[8] set-up for real gas monitoring application, particularly for the LHC experiments.

6.1.5 Monitoring of CMS CSC gas mixture

The first application of the SWPC as monitoring tool has been implemented in the CMS experiment for the Cathode Strip Chamber (CSC) operated with Ar/CO_2/CF_4 (40/50/10). The monitoring of CSC gas mixture is particularly important because gas recirculation and recuperation systems are used. Indeed:

- gas recirculation requires mixture purification and therefore the necessity to control functionality and effectiveness of the purifier modules;
- the quality of recuperated CF_4 (Section 5.6) must be granted for a safe and long-term detector operation.

Two SWPCs have been installed: after the mixer and on the supply line to the detector (i.e. after purifier module and injection of the small fraction of fresh mixture, Figure 6.13). This configuration allows to monitor the fresh gas mixture injected and the one sent to the detectors. The new monitoring system is used in parallel with standard analysis tools (O_2 and H_2O analyzers and GC).

The two SWPCs are irradiated with a 3 MBq ^{109}Cd radioactive source emitting gammas of 22 keV (83%). The counting rate observed for each SWPC is about 400 Hz. Figure 6.14(a)

[8]The sensitivity to gas mixture variations depends on the gas type varying from 100 ppm (O_2) and 0.1% (CF_4). In presence of pollutants causing aging the set-up sensitivity is below 1 ppm for all tested materials.

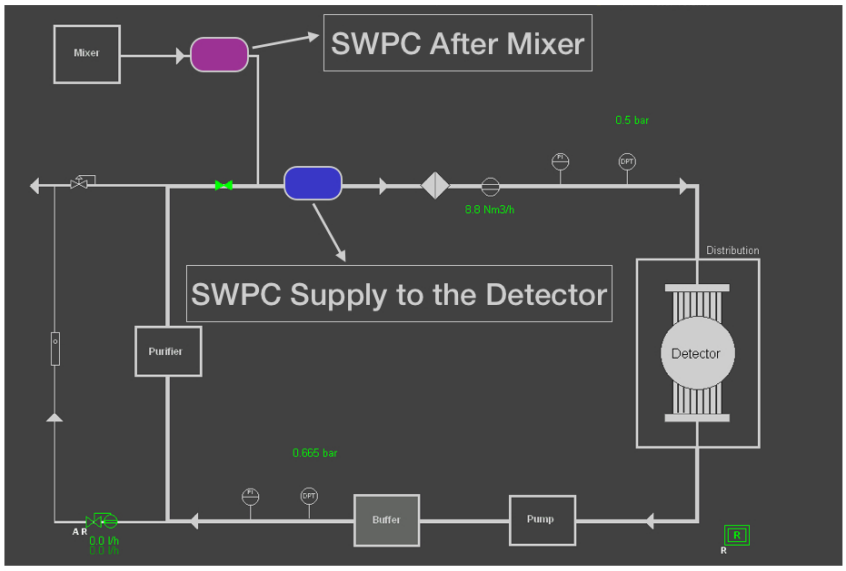

Figure 6.13: Schematic view of the CSC gas system. The position of the two SWPCs is indicated in the schematic. SWPC "After Mixer" is located right after the mixer to analyze the fresh gas mixture injected into the gas system while SWPC "Supply to the Detector" is located after the purifier and the fresh mixture line to analyze the gas that is directly injected into the detector.

shows the pulse-charge spectrum obtained at the efficiency plateau. A clear signal is visible and the mean value can be used for monitoring the detector performance.

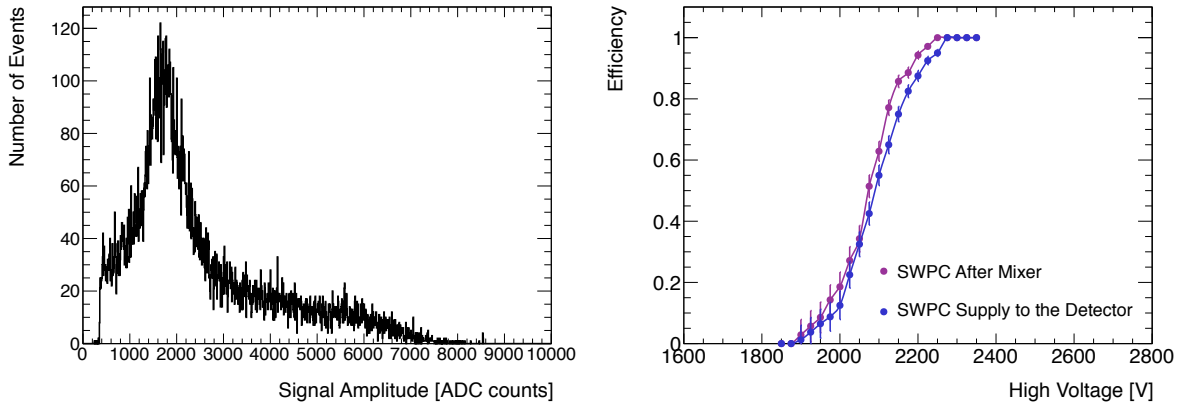

(a) (b)

Figure 6.14: (a) Pulse-height spectrum of a SWPC irradiated with a ^{109}Cd radioactive source. The 22 eV gamma peak is clearly visible. (b) Efficiency of the two SWPCs used for the gas monitoring in the CMS CSC gas system. The names "After mixer" and "Supply to the Detector" refer to their position in the gas system.

After the installation of the new fourth CSC endcap layer (ME4), the SWPCs set-up has been employed to re-tune and monitor the purifier module. Figure 6.15(a) shows the normalized gain of the two monitoring chambers. The SWPC "After Mixer" has a stable gain while fluctuations between 0.65 and 1.15 are visible for the SWPC "Supply to the Detector". This behavior can

be easily correlated to instability in the O_2 concentration[9] produced by a malfunctioning of the purifier module (Figure 6.15(b)).

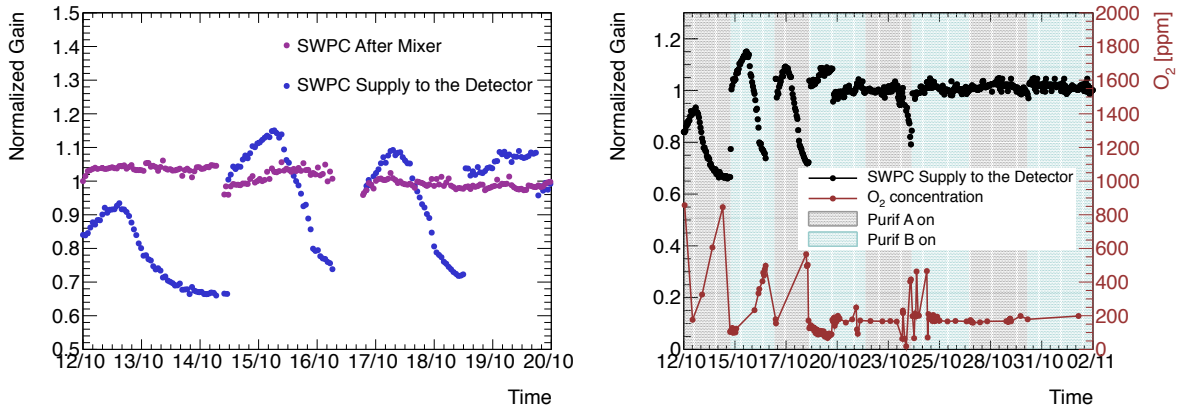

(a) (b)

Figure 6.15: (a) Normalized gas gain as a function of time for the two SWPCs installed in the CMS CSC gas lines ("After Mixer" and "Supply to the Detector"). The SWPC "Supply to the Detector" has fluctuations in the gas gain. (b) Trend of SWPC normalized gain and O_2 concentration in the gas mixture "Supply to the Detector" where the purifier cycles are also indicated.

Detailed tests have been conducted to find the new best settings for optimizing the purifier functionalities. Figure 6.16 shows a schematic view of the purifier module with the main parameters highlighted. The CSC purifier hosts two 24 l cartridges filled with Ni-Al_2O_3 catalyst, mainly devoted to O_2 absorption. This type of cleaning agent is usually regenerated at high temperature by flushing H_2. It has been found that a temperature of 240°C combined with an increase of about 30% in H_2 flow and in regeneration time allowed to restore good performance. Also the amount of gas mixture, which is passing through the purifier, has been increased by 20%.

The stability of the normalized gain during the first period of Figure 6.17 confirms the effectiveness of the new settings. Starting from these conditions, the use of recuperated CF_4 is possible. The two SWPCs show stable performance all along the period in which recuperated CF_4 is used (Figure 6.17). Nevertheless a minor increase in the gas gain for the SWPC "Supply to the Detector" is visible and it can be explained with the presence of a small concentration of Ar in the recuperated CF_4 (Figure 6.18(a)). An adjustment of the main Ar flow injected from the mixer will be needed at the LHC restart after LS1 to balance for this Ar contamination in the recuperated CF_4 (Figure 6.18(b)).

The quantity of recuperated CF_4 was about 100 m^3 and it was injected into the system for about two months. A 70% reduction of the operational costs and a 99.7% reduction of the CO_2 equivalent emission have been achieved. The CSC muon system as well as the monitoring SWPCs showed stable behavior all along this test period, which represents the first attempt of using recuperated CF_4 for CSC detectors.

[9]The level of fluctuations observed for the normalized gain is in agreement with the SWPC gas gain sensitivity to O_2 as discussed in Section 6.1.3.

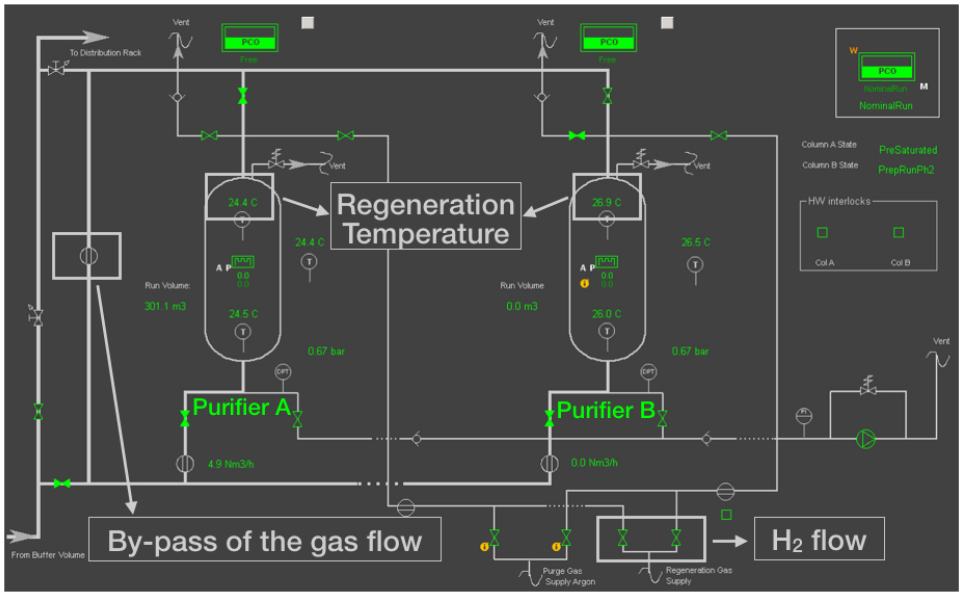

Figure 6.16: Schematic view of the CSC purifier module. The parameters modified for a better purifier cycle are indicated.

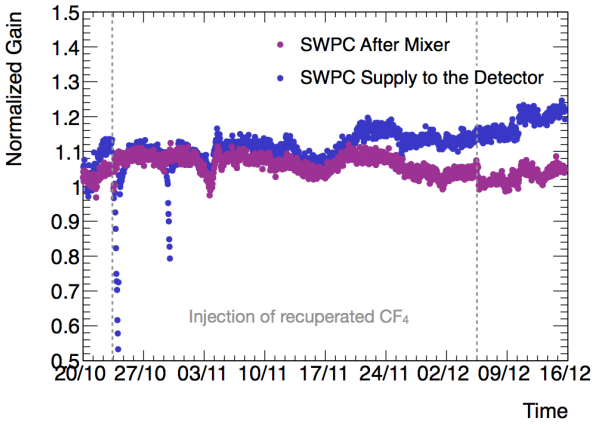

Figure 6.17: Normalized gas gain as a function of time for the two SWPCs installed in the CMS CSC gas lines ("After Mixer" and "Supply to the Detector") during the periods "before injection of recuperated CF_4", "during injection of recuperated CF_4" and "after recuperated CF_4".

6.2 Studies of GEM detector operated in gas recirculation system

Gas Electron Multiplier (GEM) [88] detectors are operational in the LHCb and TOTEM experiments as well as in the COMPASS experiment at the Super Proton Synchrotron (SPS). In the upgrade program foreseen for LHC Phase 2 (Section 2.4) large GEM systems are planned to be installed in the CMS and ALICE experiments. Also an upgrade of the existing LHCb-GEM system is scheduled. Given the increase, both in number and size, of the new GEM systems, more attention to operational costs and gas emission to the atmosphere is needed. A dedicated R&D study has been started to evaluate performance of GEM detector operated with CF_4 based gas mixtures in gas recirculation.

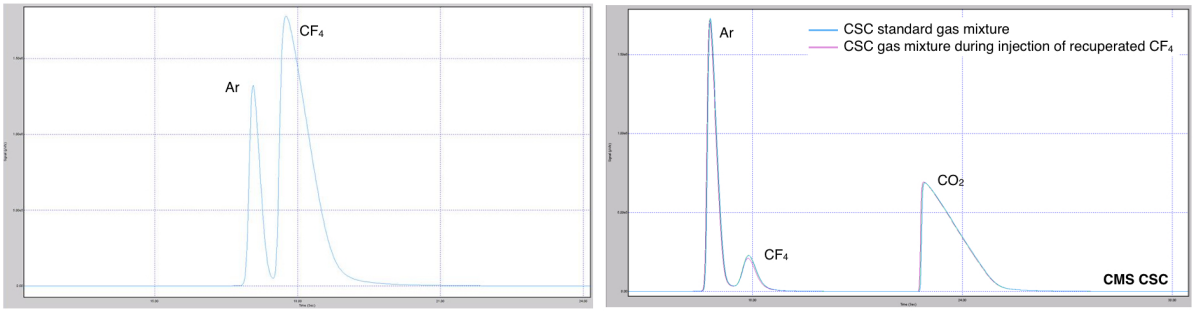

(a) (b)

Figure 6.18: (a) Gas chromatogram of the recuperated CF_4: the presence of Ar in a concentration of 12% is visible. (b) Gas chromatogram of the CSC gas mixture before and during the injection of recuperated CF_4. A clear difference in the CF_4 peak is visible.

6.2.1 GEM working principle

The GEM is a 50 μm thick insulating Kapton foil, clad on each side with a thin copper layer (5 μm) and chemically perforated with a high density of holes. The holes have usually a bi-conical structure with an external diameter of 70 μm and internal of 50 μm and a pitch of 140 μm. All the GEM foil parameters can be changed depending on the experiment purpose. A suitable voltage (300-500 V) is applied between the two metal sides to generate a high electric field inside the holes (about 100 kV/cm). Electrons and ions released by ionizing radiation in the gas mixture are guided into these holes, which act as multiplication channels where avalanches can start developing (Figure 6.19(a)). The major advantage of GEM detectors is the separation between gas amplification and readout stage, resulting in a fast readout signal. A single GEM detector is made of a GEM foil between two flat parallel electrodes (the upper electrode plays the role of cathode while the lower one is the anode). A detector with two or three piled-up GEM foils (double-GEM or triple-GEM detector respectively, Figure 6.19(b)) is more convenient for obtaining higher effective gains and low discharge probability, without requiring too high voltages applied to each single GEM foil. The gas mixture used to operate a GEM detector is usually[10] based on Ar and CO_2 with the possibility to add CF_4 if a fast drift velocity is needed. However, the addition of a strong electronegative gas requires operation at higher voltages. Furthermore the presence of fluorine, with related high reactive radicals, can produce long term aging effects that need to be evaluated. Indeed etching on the holes of GEM foil was observed with inappropriate gas flow rate conditions inside the detector [89].

6.2.2 Experimental set-up

The experimental set-up reflects as much as possible the detector operation conditions at the LHC experiments in terms of gas system. The triple-GEM detectors used at the LHCb experiment and foreseen for CMS have gap sizes, starting from the cathode, of g_d=3 mm, g_{t1}=1 mm, g_{t2}=2 mm, g_i=1 mm (Figure 6.19(b)). A 10×10 cm^2 triple-GEM has been built with the above configuration using Kapton GEM foils with holes of 70 μm and a pitch of 140 μm, each foil

[10]Special cases are present, where GEM are operated in particular conditions. For example, in the case of the upgrade of ALICE TPC the gas mixture for GEM is Ne/CO_2/N_2 (90/10/5) [28].

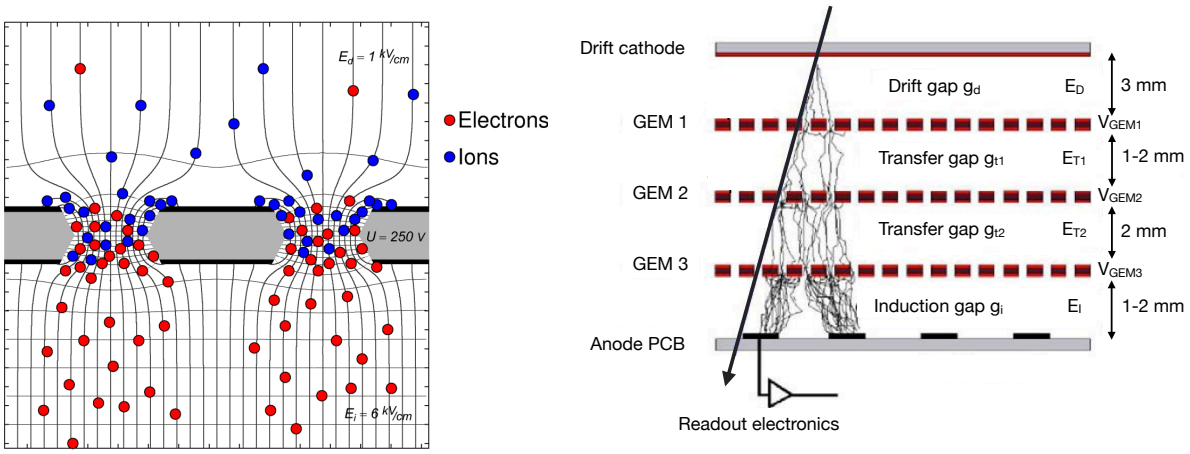

(a) (b)

Figure 6.19: (a) Qualitative scheme of a single-GEM detector operation together with the 2D map of electric field lines and equipotential lines in proximity of the GEM holes. (b) Cross section of the triple-GEM detector. E_D, E_{T1}, E_{T2} and E_I are the drift, the first and the second transfer and the induction fields respectively; g_D, g_{T1}, g_{T2} and g_I are the drift, the two transfer and the induction gaps respectively.

having a capacitance of about 5.8 nF. The read-out board is a commercial printed circuit board (PCB) electrode, finely segmented to obtain good spatial resolution in two dimension. The HV partition has been specifically chosen for the 3/1/2/1 mm configuration where the electric fields between GEM foils are about 3.5 kV/cm. A HV filter has been used to minimize possible voltage fluctuations.

Given the purpose of the test, the signal is not acquired for each single read-out strip but directly on the third GEM foil while the current is recorded on the read-out pad through a Picoamperometer Keithley 6517A. The signal acquired from the third GEM foil is amplified with a home-made preamplifier[11] and a ORTEC 572A amplifier. The signal is digitized using the CAEN Digitizer DT5724. A custom-made DAQ software has been developed to record pulse-charge spectrum, detector current, gas and environmental parameters. The gas and environmental parameters are obtained from a closed loop gas system developed in the contest of this R&D.

Triple-GEM operation in gas recirculation mode implies the use of a gas system allowing to simulate real operation conditions at the LHC. The operation principles are the same illustrated in Section 5.1 and a simplified sketch of the small CL system is visible in Figure 6.20. A mixer composed of three MFCs provides the gas mixture, which is split into two lines for detectors operating in open and closed mode, respectively. Each main gas line is divided into several sub-lines supplying well defined gas flows to several detectors by means of manual flowmeters. For closed mode operation, O_2 and H_2O sensors are installed at the output of the detectors. The O_2 sensor is the Panametrix O2x1, based on electrochemical process, and the H_2O sensor is the Vaisala Dewpoint Transmitter DMT242, based on capacitive measurements. A bubbler filled with water[12] is installed on the return line after the detectors to avoid any risk

[11] The preamplifier used does an integration and amplification of the input signal.

[12] Bubblers are usually filled with oil. In this case the choice of water is dictated by the need of avoiding all

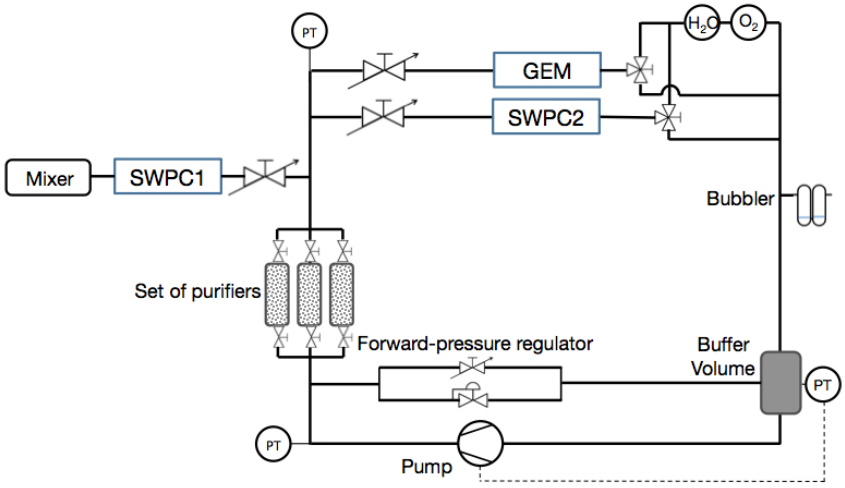

Figure 6.20: Schematic view of the small replica of a LHC closed loop gas system developed for laboratory and R&D studies.

of detector over-pressure in case of wrong manipulation or failure of components related to the pressure regulation. A buffer is used to attenuate the gas pressure fluctuations caused by the pump while a forward-pressure regulator is installed to create a by-pass flow around the pump needed to adjust the pump gas flow capacity to the flow requested in the recirculation loop. The gas mixture collected through the pump is sent to a set of cartridges, which can be filled with different cleaning agents. The purified gas is then sent back to the detector and a small fraction of fresh mixture can be re-injected. The gas system is equipped with relative and absolute pressure sensors and temperature sensors. Gas and environmental parameters are recorded using a Pico ADC-24 Precision Data Logger with a software based on C++ specifically developed for this application. The main feature of the developed software is its interfacing with the detector DAQ allowing a completely synchronized data acquisition in a single output file.

A SWPC (SWPC1) has been installed after the mixer in parallel to the the fresh gas mixture line to monitor the gas mixture composition and the presence of contaminants. The triple-GEM detector has been placed in the CL gas system as it is shown in Figure 6.20 and in a parallel gas line a second SWPC (SWPC2) has been installed. The scope of the SWPC2 is to monitor the gas mixture concentration and the presence of impurities and contaminants that can be created and accumulated during gas recirculation. As seen in Section 6.1, SWPCs are the ideal tools for detecting any type of gas problems (both on detector performance and gas system operation). The gas system developed allows to operate GEM and SWPC2 in open mode or in closed loop with the possibility to choose different recirculation rates.

The gas system is completed with the integration of specific gas analysis tools. A GC allows the analysis of the gas mixture composition after the mixer and in the gas line after the detectors operated in recirculation mode. A Mass Spectrometer (MS) is complementary used to identify pollutants, which are not easily recognized with the GC. A Ion Specific Electrode (ISE) station has been implemented to search and quantify the presence of F^- ions, which are created inside the detector gas volume (Section 6.1.4) and could accumulate during closed loop operation.

possible source of contaminants, like oil vapors.

The window of the triple-GEM detector used in the present study is permeable to Air. In order to proceed with the CL validation test, it has been decided to close the detector in a box flushed with N_2 allowing to minimize effects due to permeation of O_2 and H_2O in the detector active volume. A further reduction of O_2 and H_2O concentration can be achieved using specific cleaning agents (Section 6.2.4). During the test it has been decided to flush the triple-GEM detector with about 10 detector volume/h, similarly to LHCb.

6.2.3 Calibration of the triple-GEM detector to gas variations

The triple-GEM detector has been tested with Ar/CO_2 (70/30) and Ar/CO_2/CF_4 (45/15/40) gas mixtures before starting operation with the new gas recirculation system. The basic idea is to use the data acquired as reference for the afterwards operation. The efficiency curves as a function of the high voltage are shown in Figure 6.21(a). The use of the gas mixture containing CF_4 implies an increase of about 800 V in the total applied voltage that is also visible for the gain curves in Figure 6.21(b). The operation condition is achieved at a gas gain of about 10^4. The

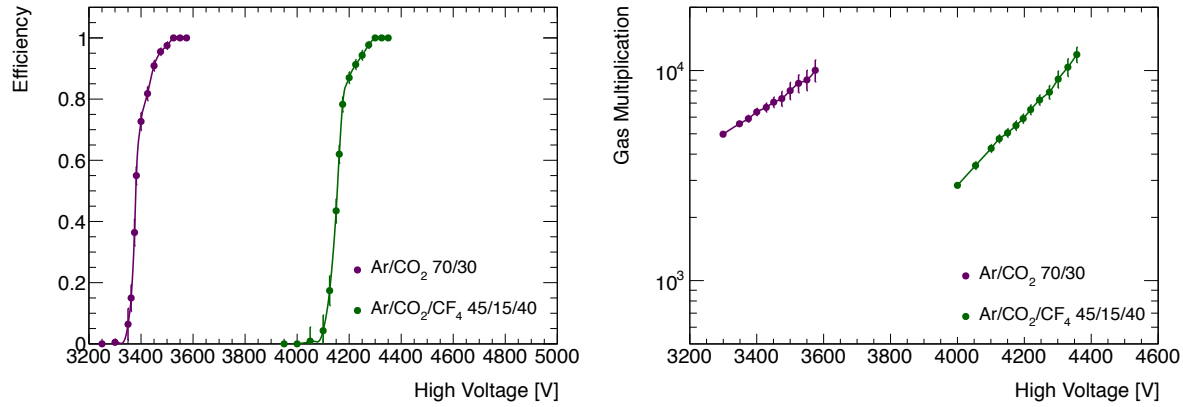

(a) (b)

Figure 6.21: Triple-GEM (a) efficiency and (b) gas multiplication factor for the two more standard gas mixture compositions.

triple-GEM signal acquired from the third GEM foil is analyzed generating the charge-pulse spectrum, which is used to monitor the detector performance, similarly to SWPC. Figure 6.22(a) shows an example of charge-pulse spectra of the triple-GEM operated with the two gas mixtures tested. The shift of the peak mean charge between the two gas mixtures is due to the presence of CF_4, as it has already been seen for the efficiency curves. The gas gain correlation for temperature and atmospheric pressure variation has been established (Figure 6.22(b)). The mean of the pulse-charge spectrum increases with the increasing of T/P_{atm} following equation 6.4. The values of the fits have been used to correct the gas gain in the following measurements.

During recirculation mode, O_2 and H_2O concentrations increase. In particular, O_2 can enter in the gas system through leaks, bad quality of supply bottles (Air contamination) and, in the case of the triple-GEM used, through the permeability of some detector components. A systematic test has been performed to quantify the triple-GEM sensitivity to the presence of O_2. Figure 6.23 shows the variation of the pulse-height spectrum mean value using as reference

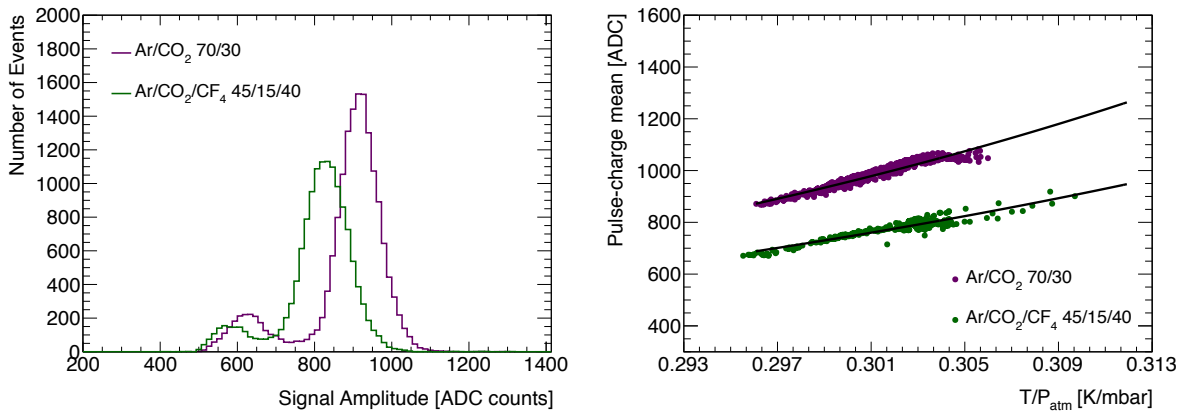

(a) (b)

Figure 6.22: (a) Pulse-charge spectra for triple-GEM detector operated with Ar/CO_2 (70/30) and $Ar/CO_2/CF_4$ (45/15/40) gas mixtures. (b) Means of the pulse-height spectrum for a triple-GEM detector as a function of T/P for two gas mixtures.

an O_2 concentration of 240 ppm. The energy resolution is also plotted. The mean value decreases almost linearly with the increase of the O_2 concentration, being O_2 an electronegative gas. On the contrary the energy resolution is not affected and it stays almost constant at about 30%. Comparing the signal variation at different O_2 concentrations for SWPC (Figure 6.7(b)) and triple-GEM (Figure 6.23), it can be easily seen that the SWPC is about seven times more sensitive than GEM (sensitivity of 7%/100 ppm and 1%/100 ppm respectively), remarking the utility of SWPC to identify the presence of pollutants. On the other hand, the triple-GEM can find a more suitable place in detector application since it is less affected by small variations in gas mixture concentrations, which can occur in complex experiments.

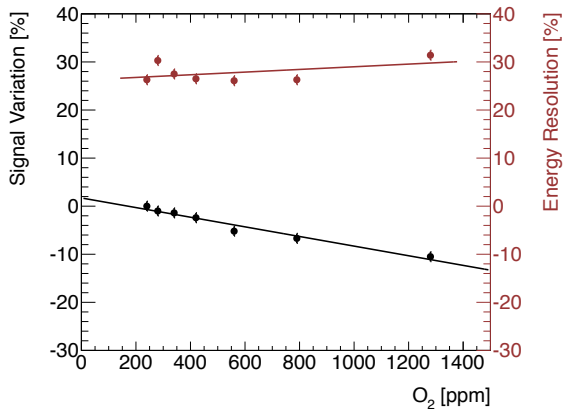

Figure 6.23: Variation of the triple-GEM pulse-height spectrum mean value and energy resolution as a function of O_2 concentration in a Ar/CO_2 (70/30) gas mixture.

6.2.4 Operation of triple-GEM detector in a closed loop gas system

The operation of gaseous detectors in recirculation mode is a critical procedure since several parameters, as detector pressure or gas pollutants, play an important role and they can drasti-

cally affect the detector performance. Before testing the triple-GEM in closed loop, longevity tests have been performed using the CL gas system operated in open mode to avoid any possible gas contamination or changes in gas parameters as well as to certify the reliability of the gas system itself. The triple-GEM stability over time has been analyzed for two different gas mixtures, recording the current and the pulse-charge spectrum. At the same time SWPC1 and SWPC2 have been used to monitor the fresh gas mixture (SWPC1) and the gas system operation (SWPC2).

Open mode operation in Ar/CO_2 gas mixture

In the first operation period, the triple-GEM and SWPCs have been operated with Ar/CO_2 (70/30) gas mixture collecting a total integrated charge of 1.3 mC/cm^2 and 2 mC/cm, respectively. Figure 6.24 shows the triple-GEM normalized gain corrected for temperature and pressure changes as a function of the integrated charge. The gain is constant over the whole operation period for the triple-GEM and SWPCs confirming that no aging or gas effects are present.

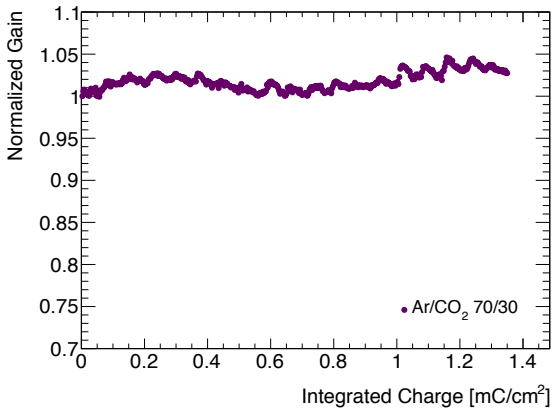

Figure 6.24: Normalized gain as a function of integrated charge for the triple-GEM detector operated with Ar/CO_2 (70/30) gas mixture. The gain has been corrected for temperature and pressure variations using the parameters of the fit obtained in Figure 6.22(b).

Open mode operation in $Ar/CO_2/CF_4$ gas mixture

Afterwards the triple-GEM and SWPCs have been operated with $Ar/CO_2/CF_4$ (45/15/40) gas mixture. Even in this case the triple-GEM normalized gain, corrected for temperature and pressure changes, is stable along the whole operation period (Figure 6.25). Only a localized drop gain of 0.5% for GEM (and SWPC2) is visible after about 1 mC/cm^2, which is due to on-going small modifications on the set-up that caused a pressure variation.

Closed loop operation in $Ar/CO_2/CF_4$ gas mixture

After a stable time in open mode with $Ar/CO_2/CF_4$ (45/15/40) gas mixture, the gas system has been turned into recirculation mode without using the purifiers. The decision to not use any cleaning agent is motivated from the need to understand the maximum level of impurities

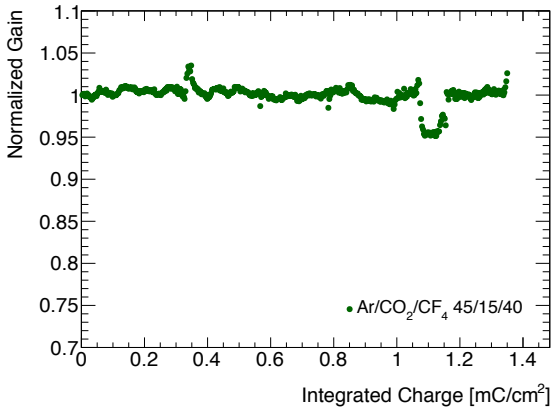

Figure 6.25: Normalized gain as a function of integrated charge for the triple-GEM detector operated with $Ar/CO_2/CF_4$ (45/15/40) gas mixture. The gain has been corrected for temperature and pressure variations using the parameters of the fit obtained in Figure 6.22(b).

that can accumulate in the CL. During the test, different fractions of gas recirculation have been tested monitoring all gas parameters as well as GEM and SWPCs performance. The different quantities of recirculated gas are handled by adjusting the fresh gas injected into the system. The bubbler assures a constant pressure inside the gas system allowing to expel the same amount of gas injected into the system. In the first operation period a recirculation of about 65% has been used since it is a percentage easily achievable with the gas system and it allows to understand how the gas parameters can change in recirculation mode. After a period of integrated charge similar to the one obtained in open mode, the recirculation fraction has been increased up to 95% in three steps (80%, 90% and 95%) and then put back to about 50% to have a term of comparison with the former results. Figure 6.26 summarizes the triple-GEM performance, expressed in term of the normalized gain, during the different recirculation mode periods (data have been corrected by temperature and atmospheric pressure variations). The increase of recirculation fraction implies a decrease in the normalized gas gain until about 0.65 for 95% of recirculated gas. This effect is not due to deterioration of the detector itself but to the changes of several gas parameters during recirculation. This statement is easily demonstrated by restoring a low level of recirculation (about 50%): the normalized gain is back to 1.

Both SWPCs have been closely monitored during the recirculation test. The SWPC1 gain is stable along the whole period confirming that the fresh mixture injected into the gas system is correct and it does not contain impurities, which would have affected the detector performance. On the contrary, the SWPC2 gain starts to constantly decrease when the system is switched to recirculation mode. Indeed SWPC is very sensitive to the gas mixture composition and the presence of contaminants (Figure 6.7) and its behavior matches with the increasing of O_2 and H_2O concentrations inside the recirculated gas mixture.

The GEM gain shift can be correlated and quantified with the variation of the O_2 and H_2O concentrations as well as presence of further impurities. Figure 6.27(a) shows the trend of gas gain and O_2 concentration as a function of the recirculation rates. The O_2 is present in a level of 100 ppm in open mode while its concentration increases in closed loop with the increase of the recirculation fraction. The O_2 accumulation is due to a reduced gas replacement. It has been shown that the triple-GEM gain changes of about 10% with an increase of 1000 ppm

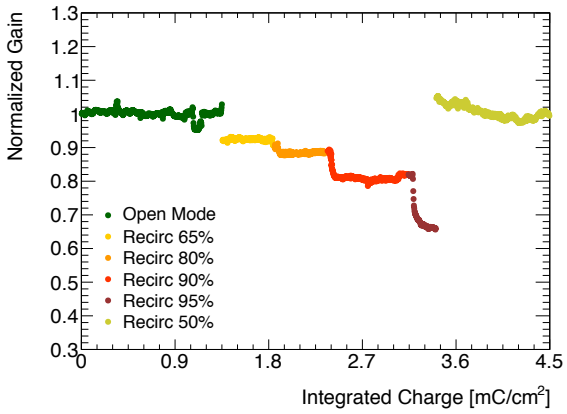

Figure 6.26: Normalized gain as a function of integrated charge for the triple-GEM detector operated with Ar/CO_2/CF_4 (45/15/40) gas mixture during different rates of recirculated gas. The gain has been corrected for temperature and pressure variations using the parameters of the fit obtained in Figure 6.22(b).

of O_2 (Figure 6.23), so other effects have to be taken into account for the gain drop under recirculation. Indeed also the H_2O concentration increases with the fraction of recirculated gas (Figure 6.27(b)) suggesting a correlation between gas gain and presence of H_2O.

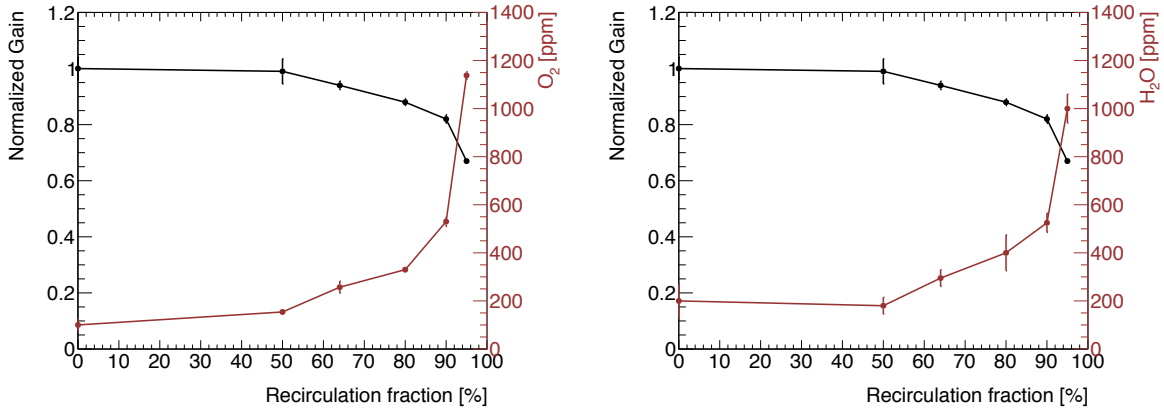

(a) (b)

Figure 6.27: On the left y-axis the normalized gain as a function of the recirculation fraction for the triple-GEM detector operated with Ar/CO_2/CF_4 (45/15/40) gas mixture while on the right y-axis the (a) O_2 and (b) H_2O concentrations obtained during the different recirculation periods.

While the O_2 and H_2O concentrations have been constantly monitored during the recirculation periods using O_2 and H_2O analyzers, the only way to monitor the N_2 concentration is through dedicated measurements with the GC. Figure 6.28 shows the trend of gas gain and N_2 concentration as a function of the recirculation rates. As for O_2 and H_2O, the N_2 concentration increases with the recirculation fraction, reaching about 4.5% with 95% of recirculated gas. Indeed N_2 enters inside the gas system from the triple-GEM detector, which is enclosed in a box flushed with N_2 since some of its materials are permeable to Air. However, the gas gain variations as a function of N_2 cannot be quantified since no dedicated studies have been performed.

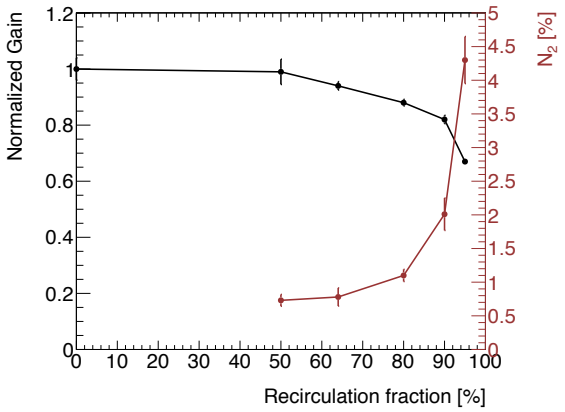

Figure 6.28: Normalized gas gain and N_2 concentration as a function of recirculation fraction for the triple-GEM detector operated with Ar/CO_2/CF_4 (45/15/40) gas mixture.

A dedicated study has been performed using the ISE station to quantify the presence of fluoride ions in the gas mixture. The ISE station measures free fluoride ions in aqueous solutions using a sensing element bounded into an epoxy body. When the sensing element is in contact with a solution containing fluoride ions, an electrode potential develops across the sensing element. This potential, which depends on the level of free fluoride ions in solution, is measured against a constant reference potential with a digital meter. The fluoride ions are created from the CF_4 in presence of radiation (Section 6.1.1) and they obviously accumulate inside the gas mixture during recirculation. The fluoride accumulation rate is about 1.8 ppm/day at 95% recirculation while it goes down to 0.75 ppm/day at 50% recirculation. As previously said, the accumulation of F^- should always be avoided since etching effects can occur modifying the GEM holes diameters.

Closed loop operation with mixture purification

It has been demonstrated that the triple-GEM detector can work well with gas recirculation. The worsening of the performance is only due to the accumulation of contaminants inside the gas system and the triple-GEM gain is back to the original value by flushing with fresh gas mixture. The use of purifiers inside the closed loop is therefore needed. The first cleaning agent used is MS4 Å , which mainly absorbs H_2O and O_2 in smaller quantities. Figure 6.29 shows the trend of the triple-GEM gas gain when the purifier is added to the gas system and the recirculation fraction is changed from 50% to 95%. The gain decreases until it stabilizes at about 0.8. This drop is due to the increase of the O_2 concentration caused by the change of the recirculation fraction and by O_2 absorption incapability of the purifier. Nevertheless the comparison between the gas gains at 95% of recirculation with and without purifier shows a good improvement: with the purifier the triple-GEM gain is back at around 0.8 instead of 0.65. Even the fluoride accumulation rate decreases to 0.31 ppm/day.

This test confirms the necessity of gas purification module for the operation of triple-GEM detector in closed loop. In real system is even more important the use of two dedicated purifiers for O_2 and H_2O removal. A good understanding of the process has been achieved, representing an important step forward for the design of the large GEM system for the future LHC upgrades.

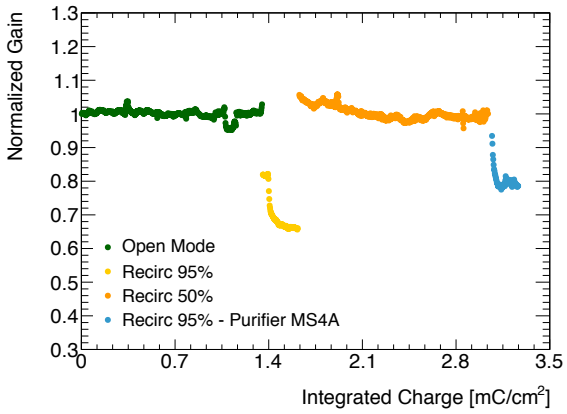

Figure 6.29: Normalized gain as a function of integrated charge for the triple-GEM detector operated with Ar/CO_2/CF_4 (45/15/40) gas mixture with different recirculation rates with and without the use of purifier in the gas system.

6.3 Studies for the replacement of the R134a in RPC systems

The Resistive Plate Chamber (RPC) detectors can contribute to the general strategy of greenhouse gas reduction by moving to gases with lower GWP. RPCs are operational at LHC in the ALICE, ATLAS and CMS experiments where they are widely used for the muon trigger systems thanks to their fast time resolution ($\sim$1 ns) and suitable space resolution ($\sim$1 cm).

A RPC is a particle gaseous detector using a constant and uniform electric field ($\sim$5 kV/mm) produced by two parallel electrodes plates. Figure 6.30 shows a schematic view of a typical double-gap RPC [90]. The detector is made of two electrodes of a high bulk resistivity material[13], which is needed to confine the charge multiplication, taking place inside the detector, in a small area. On the outside electrode surfaces a semi-conductive layer is deposited, which is transparent to the electric pulse created inside the counter because of high surface resistivity. This allows to detect the induced signals on the pick-up strips (made of conductor material) that are electrically isolated from the conducting foil by means of an insulating layer. The gap between the two electrodes is usually about 2 mm. Several gaps can be used together to assemble a RPC detector creating a multi-gap RPC. The gaps are filled with a well defined gas mixture at atmospheric pressure with a gas flow of about 0.3-1 volume changes/h, depending on the radiation level. The gas mixture is usually based on $C_2H_2F_4$ (R134a) with the addition of iC_4H_{10} (quencher gas) and SF_6 (electronegative) to control the formation of secondary avalanches.

RPC detectors can be operated in two different modes defined by the charge of the pulse signals:

avalanche where the amplification of the signal inside the gap is small and proportional following the Townsend mechanism.

streamer where a number of large nonlinear effects are added to the linear mechanism. Indeed the number of free electrons can exceed the limit of the Raether condition and new photoionization processes, due to recombination and excitation phenomena, ionize the

[13]The material used for the electrodes is usually High Pressure Laminate (HPL) with $10^{10-11}\,\Omega\,$cm bulk resistivity.

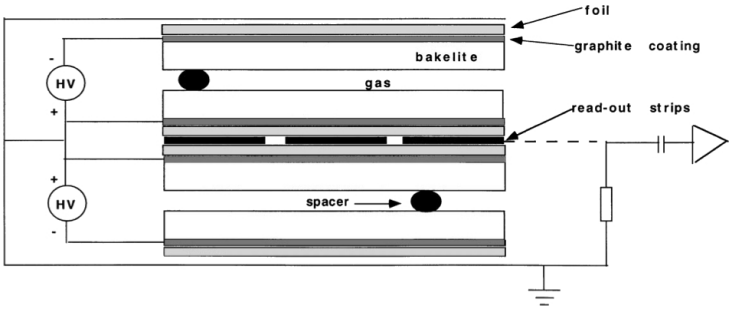

Figure 6.30: Cross-sectional view of a double gap RPC.

gas molecules around the avalanche region developing secondary avalanches along the avalanche axis. These avalanches are all close and they move forward to the electrode until the formation of one charge filament, the streamer. The streamer is not a direct evolution of the first avalanche but rather a late discharge stage.

Operation in avalanche mode is required if the detector has to sustain a high incoming particle rate (already above 100 Hz/cm^2). The voltage drop produced by ionizing particles is proportional to the pulse charge: large pulse charge produces significant voltage drop, which brings the detector out of the efficiency region. Moreover, with the use of resistive electrodes, small charge pulse produces a voltage drop that is confined in a small detector region ($\sim$mm^2) leaving the remaining surface fully efficient.

During LHC Run 1, the RPC systems performance was remarkable [91]. Table 6.3 summarizes the main features of the RPC systems installed at LHC. Both ATLAS and CMS RPC systems have a gas volume of 16 m^3 filled with $C_2H_2F_4$/iC_4H_{10}/SF_6 (95.2/4.5/0.3) gas mixture, which is recirculated for about 90% of the total flow. The ALICE experiment employs RPC for Muon Trigger (MTR) and Time Of Flight (TOF), which gas volume are 0.3 m^3 and 18 m^3 respectively. In the MTR case, the system is operated in open mode[14] while TOF RPCs are working in closed loop. The big gas volumes as well as the costs and GWP of the gas mix-

Experiment	ATLAS	CMS	ALICE (MTR)	ALICE (TOF)
Material	HPL	HPL	HPL	glass
Layout	single-gap	double-gap	single-gap	multi-gap
Surface (m^2)	4000	4000	140	170
Gas volume (m^3)	16	16	0.3	18
Gas system operation	closed-loop	closed-loop	open-mode	closed-loop

Table 6.3: Summary of the main parameters of the RPC gas systems at LHC during Run 1.

ture have made the closed loop operation mandatory. During LHC Run 1, the RPC systems in ATLAS and CMS faced the appearance of several leaks in the detector itself, mainly caused by broken gas connectors. This issue did not affect RPC operation but it implied using a larger fraction of injected fresh mixture with, consequently, an increase of costs and greenhouse emissions. During LHC LS1 an intense leak search campaign has been performed, repairing the leaks by substituting the gas connectors or gluing some broken parts.

[14]The MTR RPC system has been converted in closed loop system during LHC LS1.

However, in view of long term operation, the use of R134a will become critical. The European Union (EU) will start to phase out refrigerants with GWP higher than 150 in the near future[15]. In principle, R134a will always remain available for research applications. Once the industrial production will move on alternative gases, the R134a price will probably increase and the production capacity will be very limited. Taking into account these considerations, the only possibility for containing the RPC detector operational costs in the future is to move towards alternative gases, which are used or going to be widely used by industry as replacement of today banned gases. R1234yf and R1234ze started to be employed in the automotive air conditioning from several companies and, therefore, they are suitable candidates.

R1234yf (2,3,3,3-tetrafluoropropene) and R1234ze (1,3,3,3-tetrafluoropropene) are two structural isomers of a hydrofluorooleofin (HFO) based on the propene structure (Figure 6.31). Similarly to the R134a, the new freons contains fluorine atoms as electronegative species and therefore they are going to suppress formation of large charge pulses. Given the hydrocarbon structure, the new freons may also have some quenching capacities. However, they are certainly more reactive with respect to R134a due to the presence of a double C-bound. This is confirmed by the fact that they are currently classified as A2L, i.e. "slightly flammable" gases[16].

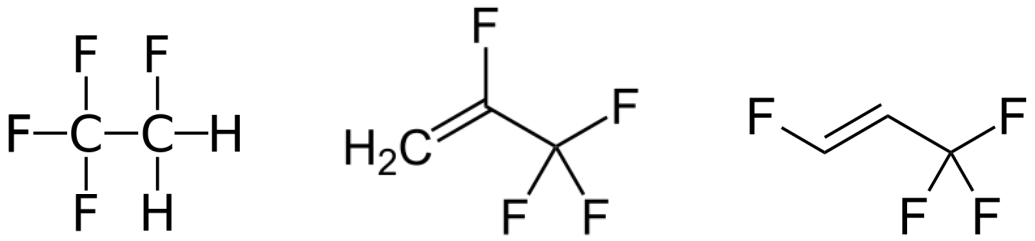

(a) (b) (c)

Figure 6.31: Chemical structure of (a) R134a (1,1,1,2-Tetrafluoroethane), (b) R1234yf (2,3,3,3-tetrafluoropropene) and (c) R1234ze (1,3,3,3-tetrafluoropropene).

The RPC communities have started to investigated the possibility of moving to alternative gases. Test results with the use of R1234yf will be discussed in the next sessions as input for further investigations on the use of different freon-based gas mixtures.

6.3.1 Experimental set-up

The performance of RPCs using different gas mixtures have been studied thanks to a dedicated set-up (Figure 6.32). Two standard HPL RPCs with a gas gap of 2 mm, a surface of about $80 \times 100\,\mathrm{cm}^2$ and read-out strips of 2.1 cm wide have been used for the tests[17]. Two scintillators, covering an area which corresponds to seven readout strips, are used for coincidence allowing detection of cosmic rays. The signal acquired from each strip is directly sent to two CAEN

[15]Outright ban of refrigerants with GWP higher than 150 was planned to start in 2011 and then postponed. Several nations in EU and USA have already banned these gases while others have started a gradual phase out.

[16]The flammability classification is based on the ANSY/ASHRAE standard 34-2007 for designation and safety classification of refrigerants.

[17]Two RPC have been used to have a term of comparison. In the following section, only results related to one RPC will be shown since the data of the second RPC were identical.

Digitizers V1720[18] for the readout of channels from both RPCs as well as the acquisition of the trigger signal from the scintillators system. The DAQ software used is the CAEN WaveDump software, which directly stores the RPC signal in ADC units as a function of time. The digitized signal is acquired for 10 μs with a 12 bit ADC resolution and ± 1.25 V range[19].

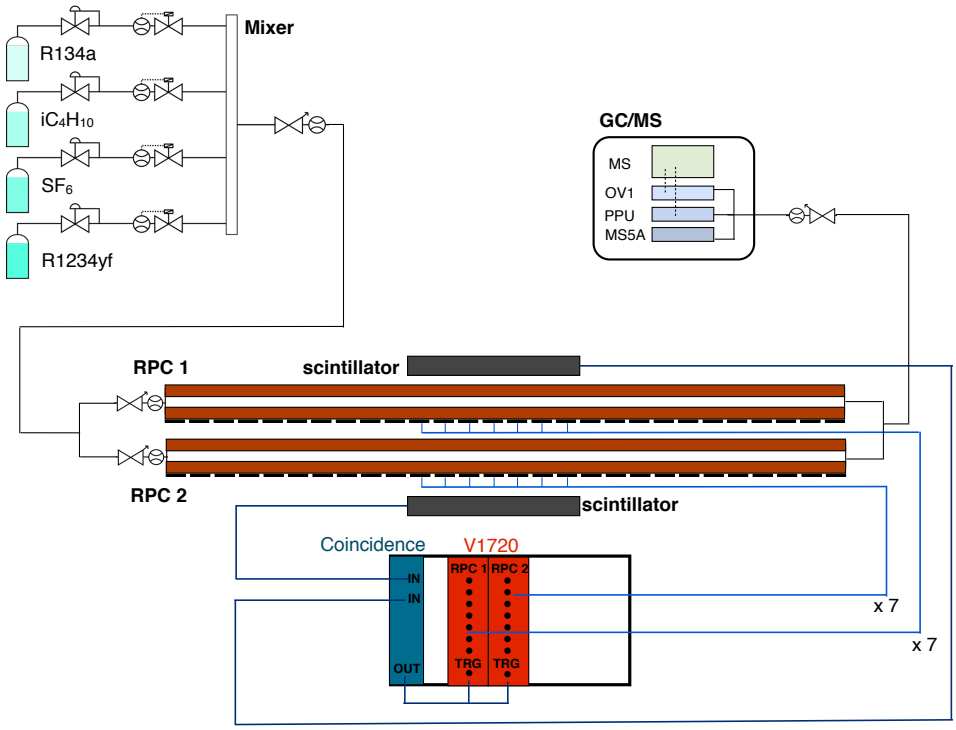

Figure 6.32: Schematic view of the set-up used to test RPCs with the new freon R12344yf. The DAQ system has been simplified showing only the two main electronics components.

The RPCs are tested in open mode flushed with about 0.3 volume/h. The gas mixture is obtained by MFCs and it can be freely changed using $C_2H_2F_4$, iC_4H_{10}, SF_6 and R1234yf (no humidification of the gas mixture is done during the test). GC analysis are regularly performed to verify the gas mixture correctness.

The measurements are taken at different voltages and various gas mixtures are tested. For each set of raw data, a "baseline analysis" is executed to remove noise fluctuations and to neglect any overshoot of the signal. The RPC signal parameters considered for the analysis are the pulse amplitude and the pulse charge. In case avalanche and streamer signals are present, the maximum pulse amplitude is taken from the streamer, otherwise from the avalanche. Therefore the maximum amplitude gives information about the presence and development of the avalanche towards streamer pulses. Usually the detector signal is studied through the pulse charge since it gives information not only on the pulse amplitude but also on the pulse duration; in this way the total charge involved in the process can be extracted. A signal is identified as avalanche if its integrated charge is below 5 pC while above it is considered a streamer. Once the RPC signal

[18]The V1720 is a 1-unit wide VME 6U module housing a 8 Channel 12 bit 250 MS/s Flash ADC Waveform Digitizer and featuring 2 Vpp single ended input dynamics.

[19]In this case 1 ADC unit corresponds to 0.5 mV.

parameters have been extracted from the data, the second analysis step computes the following informations: efficiency, average charge and event frequency for avalanche and streamer regions as well as average total charge. The efficiency is the intrinsic efficiency including the geometrical efficiency. The high voltage correction usually applied for temperature and pressure changes has not been used in this work since no significant variations have been observed during the test period. The average charge is calculated integrating the prompt signal spectrum obtained from the pulse charge distribution. The value obtained is the induced charge on the strips, which represents only a small fraction (about 5%) of the total charge created inside the gas gap.

6.3.2 RPC performance with R1234yf: a new environmental friendly Freon

The RPC performance has been studied for several gas mixtures containing different concentrations of R1234yf. The new Freon was used to substitute one of the three mixture components at the time for evaluating its quenching and electronegative capacities. RPC operation at LHC with a R1234yf based gas mixture represents the final objective of these studies.

Replacement of R134a and SF_6 with R1234yf

The first test has been performed eliminating completely the R134a and SF_6[20] since the main goal of the RPC Freon replacement is to avoid any greenhouse gases. The RPCs have been operated with R1234yf/iC_4H_{10} (95/5) and R134a/iC_4H_{10} (95/5) gas mixtures to have a direct comparison between the two freons. The use of R1234yf as main gas component requires operation at much higher applied voltages with respect to R134a. During the test the efficiency remains very low (Figure 6.33). Further studies need to be performed increasing the applied voltage to clarify if a good efficiency can be achieved. Indeed, as a fist investigation, it was decided to explore several gas mixture possibilities without taking the risk of damaging detectors and related components. In conclusion, the results of this first test show that a direct substitution between R134a and R1234yf is not possible (or at least it will require a much higher applied voltages with a direct implication on the power supplies and protection in the experiments).

Replacement of SF_6 with different concentrations of R1234yf

An approximative quantification of the R1234yf electronegativity can be performed by using it instead of SF_6 in the same concentration of the standard RPC gas mixture. Figure 6.34 shows the RPC efficiency as a function of the applied voltage using the standard gas mixture R134a/iC_4H_{10} (95.2/4.5) with the addition of 0.3% SF_6 or R1234yf. In this condition a good efficiency is reached for both gas mixtures and the required applied voltage remains at normal values. However, the fraction of streamers in the case of R1234yf is higher with respect to the standard gas mixture at equal efficiencies (Figure 6.35(a)) and, therefore, operation in pure avalanche mode cannot be established. Indeed this demonstrates that SF_6 is more electronegative than R1234yf. Pulse charges (Figure 6.35(b)) are very similar between the two gas

[20]The GWP of R134a and SF_6 is 1430 and 23900, respectively.

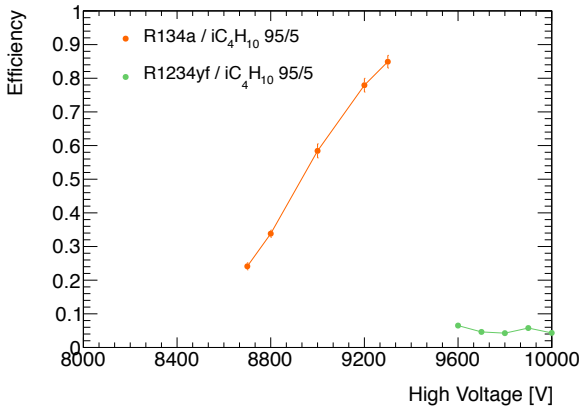

Figure 6.33: RPC efficiency as a function of the applied high voltage for the R1234yf/iC_4H_{10} (95/5) and R134a/iC_4H_{10} (95/5) gas mixtures.

mixtures for the avalanche signals while a clear separation is present for the streamers. Additionally, the cluster size has been calculated (Figure 6.36): it does not show any particular difference between the two gas mixtures (about 2 at full efficiency).

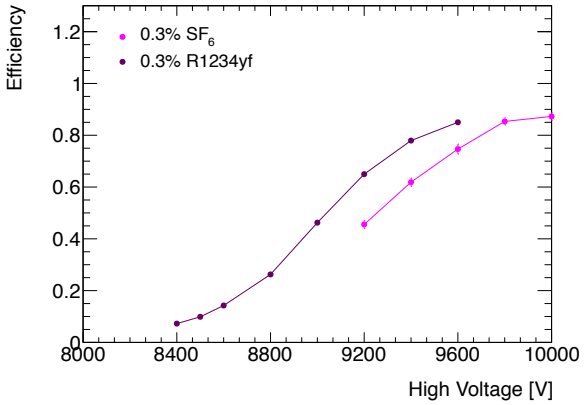

Figure 6.34: RPC efficiency as a function of the applied high voltage for the R134a/iC_4H_{10}/SF_6 (95.2/4.5/0.3) and R134a/iC_4H_{10}/R1234yf (95.2/4.5/0.3) gas mixtures.

Further tests have been performed varying R1234yf concentrations from 0% to 2.5% but no significant improvement has been observed (Figure 6.37). An applied voltage above 10000 V is always required to reach good efficiency. Increasing the concentration of R1234yf does not help in controlling the fraction of streamers, which remain very high (more than 40%) compared to the standard RPC gas mixture.

Replacement of iC_4H_{10} with R1234yf

The quenching properties of R1234yf have been investigated testing mixtures based on R134a with the addition of 5% iC_4H_{10} or 5% R1234yf. Figure 6.38 shows the efficiency curves obtained. The addition of R1234yf implies a shift towards higher applied voltages, however a good efficiency can be still achievable. Figure 6.39(a) shows the fraction of avalanche and streamer pulses versus the detector efficiency: the R134a/iC_4H_{10} mixture remains the best option for op-

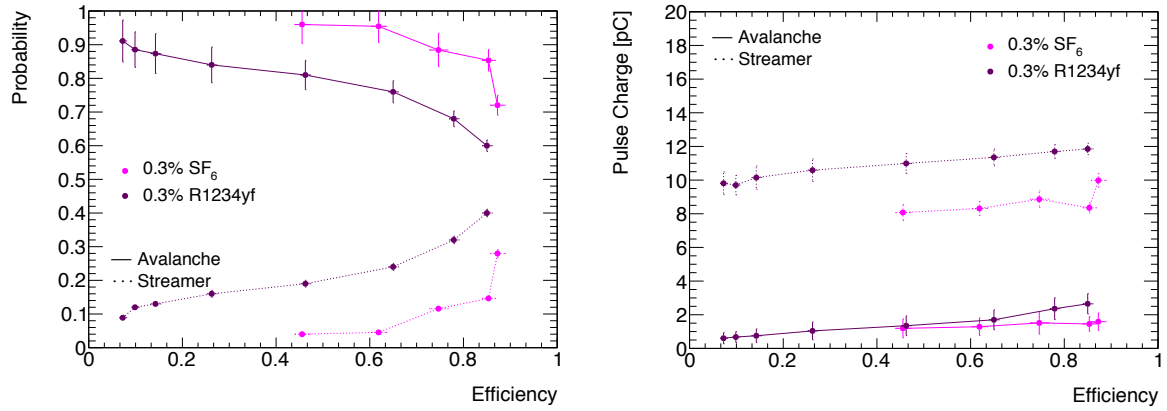

(a) (b)

Figure 6.35: Avalanche and streamer (a) probability and (b) pulse charge as a function of RPC efficiency for the R134a/iC_4H_{10}/SF_6 (94.7/5/0.3) and R134a/iC_4H_{10}/R1234yf (94.7/5/0.3) gas mixtures.

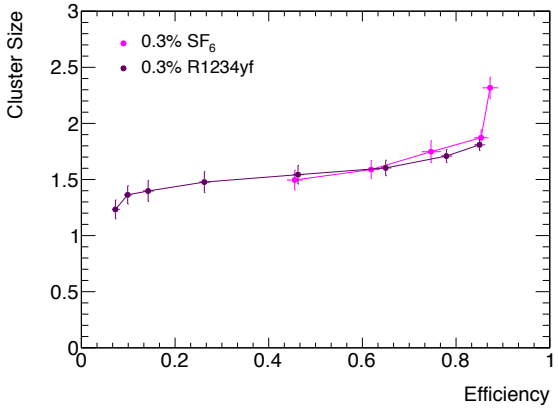

Figure 6.36: Cluster size as a function of RPC efficiency for the R134a/iC_4H_{10}/SF_6 (94.7/5/0.3) and R134a/iC_4H_{10}/R1234yf (94.7/5/0.3) gas mixtures.

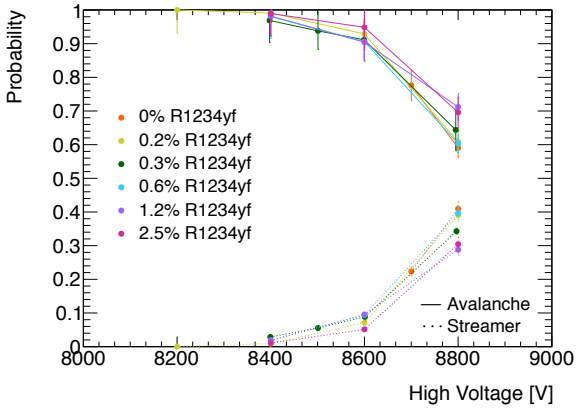

Figure 6.37: Avalanche and streamer probability as a function of RPC efficiency substituting the SF_6 with different percentages of R1234yf.

eration in avalanche regime. The use of 5% R1234yf leads to already more than 50% streamer signals at an efficiency of about 0.6. The pulse charges are very similar for both avalanche and streamer signals with a slightly increase in the case of R1234yf for streamers (Figure 6.39(b)). On the contrary the cluster size is significantly higher for the R134a/R1234yf (95/5) mixture. These effects can be an indication of lack of quenching gas. Indeed, secondary avalanches produced by photons spread around in the gas gap increasing also the pulse spatial size.

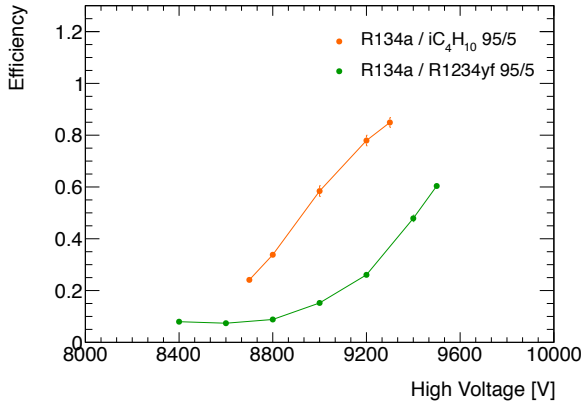

Figure 6.38: RPC efficiency as a function of the applied high voltage for the R134a/iC_4H_{10} (95/5) and R134a/R1234yf (95/5) gas mixtures.

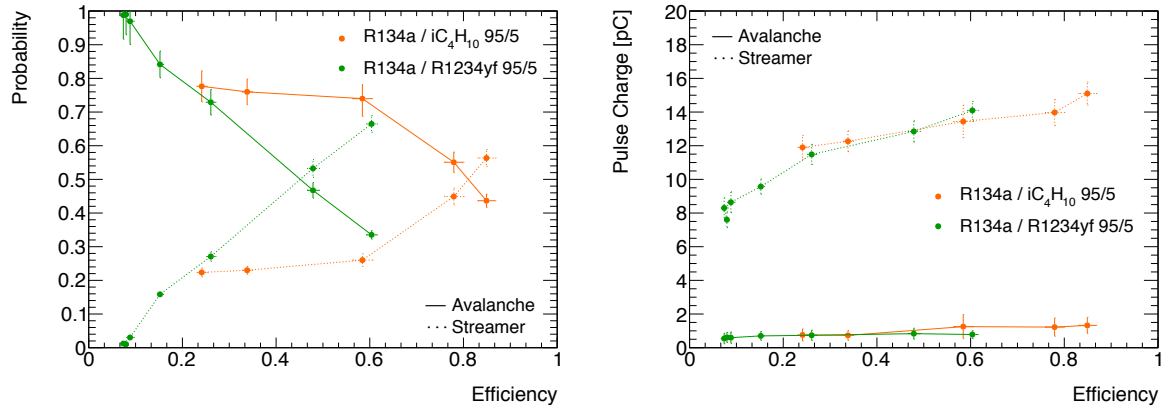

(a) (b)

Figure 6.39: Avalanche and streamer (a) probability and (b) pulse charge as a function of RPC efficiency for the R134a/iC_4H_{10} (95/5) and R134a/R1234yf (95/5) gas mixtures.

R1234yf and Ar based gas mixtures

Since a complete replacement of R134a with R1234yf is not possible and mixtures with high R1234yf concentration require very high applied voltages, the addition of Ar has been considered as an alternative solution to facilitate the charge multiplication even if it is expected to cause an increase of streamer signals[21] Three different gas mixtures have been tested using a

[21] A gas mixture based on Ar as main component is not suitable for operation at high particle rates. Indeed, the reduction of the electronegative gas leaves the possibility to the creation of large charge pulses from which the

fixed iC_4H_{10} concentration (5%) and reducing the amount of Ar (42.5%, 32% or 21%), being R1234yf the remaining part. Figure 6.40 shows the RPC efficiency as a function of the applied voltage for the three mixtures. In the case of R1234yf /Ar (74/21) the efficiency is almost zero up to very high applied voltages as it is for the R1234yf/iC_4H_{10} (95/5) mixture (Figure 6.33). With the increase of Ar concentrations, the efficiency increases, as expected, reaching the maximum value at 42.5% of Ar. However Figure 6.41(a) shows that the detector is working in

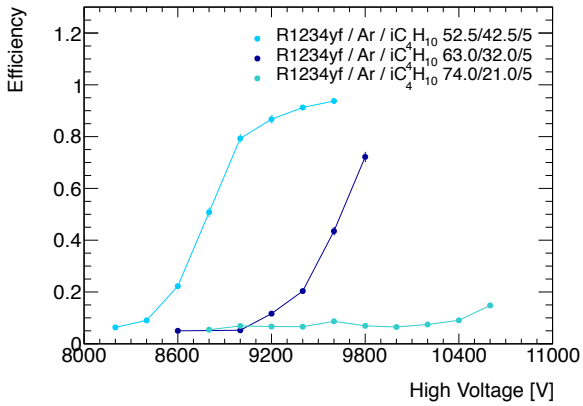

Figure 6.40: RPC efficiency as a function of the applied high voltage for three gas mixtures based on different concentrations of R1234yf and Ar and 5% of iC_4H_{10}.

streamer mode. Indeed streamer signals are predominant already at efficiencies above 0.2. The streamer pulse charges for R1234yf/Ar(52.5/42) are also a factor 2 higher with respect to the standard gas mixture (Figure 6.35(b)). Therefore the Ar based gas mixtures examined in this test are not suitable for RPC operation in avalanche mode.

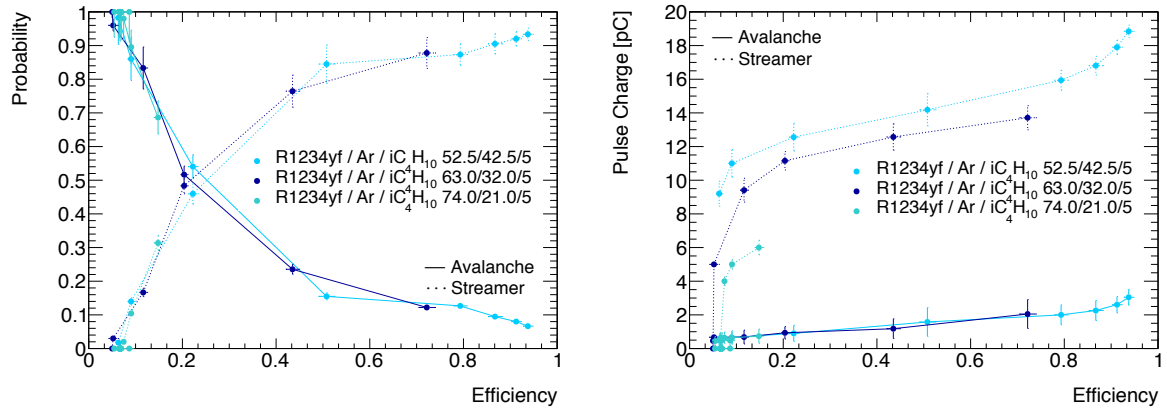

(a) (b)

Figure 6.41: Avalanche and streamer (a) probability and (b) pulse charge as a function of RPC efficiency for three gas mixtures based on different concentrations of R1234yf and Ar and 5% of iC_4H_{10}.

detector needs a relatively long time to recover.

Review of the results

The first tests performed using R1234yf confirm that the RPC gas mixture replacement is not an easy task. It has been demonstrated that the RPC detector can work with R1234yf, reaching also good operation efficiencies in some cases (for example in mixtures containing Ar). However, the sine qua non condition for LHC operation is to work in avalanche mode, given the rate capability required. This is not completely achieved with the gas mixtures tested in this work and the standard RPC gas mixture remains the best option. These tests can be considered a starting point for future investigations and as guideline for testing also different Freon gases.

6.4 Summary

Results obtained using SWPC as gas monitoring tool are very encouraging. SWPCs provide a higher and faster level of sensitivity with respect to the classical gas analyzers. The first application in the CMS CSC gas system has given outstanding results and fundamental information for the tuning of the purifier parameters adding stability and reliability to the detector operation. The SWPC monitoring system is suitable for its installation in several LHC gas systems. Indeed it can be used with different gas mixtures, it runs automatically and its results can be easily integrated in detector DCS and produce automatic warnings.

Beyond the gas mixture monitoring, muon systems will have to consider carefully the adopted gases, especially if greenhouse gases are used. Most of the gas systems are already working in gas recirculation. One of the remaining open mode systems is the LHCb-GEM, which can already benefit of the GEM R&D studies performed in view of the large GEM systems foreseen for the muon upgrades. Indeed, results show that triple-GEM detector can be operated in CL where gas purification modules are needed to control the presence of contaminants (O_2, H_2O, N_2, F^-).

Concerning the reduction of greenhouse gas emission, RPC detectors are already working in CL with a recirculation fraction of about 90-95%. The suppression of R134a production entails the search of a replacement. R&D studies have started using new Freons developed for the R134a replacement in industries. It has been demonstrated that RPC detectors can be operated with new Freons although the finding of a new gas mixture allowing stable operation in avalanche mode at LHC experiments still requires a long R&D phase.

Conclusions

The LHC Physics program and the consequent improvement of the LHC accelerator performance set important challenges to all detector systems. The increase of luminosity will lead to higher radiation doses, particle rates and pile-up limiting the performance of the current systems due to tracking inefficiency and radiation-induced effects. The present work delineates the strategies adopted to improve two different types of detectors: the replacement of precision trackers with ever increasing performing silicon detectors and the improvement of large gaseous detectors by optimizing their operating gas mixture (cost saving and reduction of greenhouse gas emissions are also important factors).

Upgrade of silicon tracking systems

The ATLAS Insertable B-layer (IBL) is the first major upgrade of a silicon tracker at LHC. The IBL makes use of new pixel and front-end electronics technologies as well as lower material budget, state-of-the art services and a novel thermal management approach. All these innovations required complex developments together with strict Quality Control (QC) and Quality Assurance (QA) protocols during construction and installation phases. After QC, bunches of 20 modules are mounted on a carbon-fibre mechanical support to form the basic element for the IBL detector assembly, i.e. the stave.

A compact setup has been designed and built for a thorough QA sequence, which has been developed and followed to characterize the 18 produced staves. The main results are:

- Each module has been fully characterized performing electrical tests, calibrations and radioactive source scans. Similarity and differences between planar and 3D sensors have been analyzed quantifying, for example, the equivalent noise charge and charge collection efficiency.

- High threshold over noise ratios have been obtained for all types of modules at warm and cold operation (22°C and -12°C respectively). These values are essential in determining the quality of IBL modules: the bigger this factor is, the less noise contamination is present during data acquisition. The fraction of noisy IBL pixels is less than 0.03% for the 1500 e^- threshold tuning while, as a comparison, in the current Pixel Detector this value is 0.06% for 3500 e^- threshold.

- A detailed classification and identification of bad pixels has been performed as major information for the stave ranking. The IBL target to have less than 0.37% of bad pixels per chip has been achieved for most of the modules. All staves are well below the target cut of 1% bad pixels and 80% are even below 0.2%.

The 18 staves qualified according to the QA criteria correspond to 216 planar and 144 3D modules for a total of 15.5 M pixels. The results obtained allowed the selection of the best 14 staves for the assembly of the IBL Detector, which has been successfully installed in the centre of the ATLAS experiment in May 2014. The QA results and the final commissioning of the full system have demonstrated that the IBL Detector performs extremely well with 99.9% of functional channels in the modules.

In parallel to the stave QA, the reliability of the IBL wire bonds has been investigated under operation conditions close to the real ones. In an intense magnetic field wire bonds oscillation and consequent breaking can occur if time varying currents pass through them at the wire's mechanical resonance frequency. The dangerous resonance frequencies have been identified experimentally and two methods for protection have been tested. The results of the resonance frequencies studies have been used for the implementation of a trigger veto for the IBL operation.

Since its installation, the IBL has been successfully operated stand-alone, together with the existing Pixel system and in ATLAS global runs that include all detectors. IBL will now join the LHC Run 2 as part of the ATLAS Pixel Detector ensuring the best possible tracking performance. The IBL project can be considered as case example for future silicon detectors at LHC experiments. Entire tracking systems will be replaced during LS2 in ALICE and LHCb, and during LS3 in ATLAS and CMS. Their common objective is to ensure higher radiation hardness, higher granularity and lower material budget to maintain and improve physics performance at very high luminosities. The IBL highlights the challenges in the design, construction and testing phases of new, very sophisticated detectors.

Upgrade of large gaseous detector systems

Muon systems at the LHC experiments are very large apparatus of the order of several thousands square meters. During the HL-LHC phase, the present detectors will be pushed close to their limits and a strategy to recover good operation conditions consists in:

- adding redundancy, i.e. more detector planes with improved performance, where particle rate becomes unmanageable;
- ensuring good operation conditions for the long-term conservation.

Concerning the latter point, infrastructures as the gas systems play a fundamental role. The gas mixture is the active medium where charge multiplication and signal formation take place. Quality and composition of gas mixtures are therefore essential for avoiding unrecoverable degradation of detector performance, i.e. aging phenomena. Several aspects of gas systems operation that are central for HL-LHC have been studied:

- The importance of robust gas quality monitoring tools has been established, studying systematically real life examples of LHC detectors that have suffered a temporary loss of performance due to bad gas quality. It has also been demonstrated that gas quality monitoring is even more crucial in detector systems where gas recirculation and recuperation plants are used. Gas recirculation and recuperation may add complexity to operation, however they will need to be part of the overall muon systems strategy for HL-LHC in order to contain operational costs and gas emissions.

- A complementary method, based on Single Wire Proportional Counters (SWPCs), has been established for real-time monitoring of gas mixture quality and detector performance of large gaseous detector systems at LHC. This system overcomes the main limitations of standard gas analysis techniques, i.e. the delay between the moment in which the problem occurs in the gas and the relevant information is available, as well as the sensitivity to gas impurity concentrations. Thanks to the large drift volume and to the use of intense radioactive sources, which accelerate plasma chemistry processes, the SWPCs reveal to be very sensitive to pollutants that can affect the detector performance, even at concentrations below the ppm level. In this work, SWPCs have been employed successfully for monitoring the CMS Cathode Strip Chambers (CSCs) gas mixture composition during the use of recuperated CF_4. The performance of the CF_4 recuperation system, first ever built in HEP, has been studied in detail using the gas analysis techniques described, which demonstrated that the mixture with recuperated CF_4 meets the requirements for safe CSC operation.

- The reduction and eventual replacement of greenhouse gases is one of the important challenges for the muon systems in the near future. A change of gas mixture is a years-long process, as it requires multitude of short- and long-term studies and performance evaluations for a specific detector technology and geometry. In the case of Resistive Plate Chambers (RPCs), R134a and SF_6 (the main components of the current mixtures at LHC) will soon be completely banned. A new environmentally friendly Freon of new generation has been tested measuring key parameters for RPCs operation at LHC. Encouraging results have been obtained for operation at low particle rates.

- As for the gas reduction strategy, the particular case of CF_4 for GEM-based detectors has been analyzed. Currently all GEM detectors in HEP are operated with open mode gas systems where all gas is exhausted to atmosphere after being used. This operation mode can be rather impracticable for very large GEM systems, as they are being planned for the upgrade of the CMS muon system at HL-LHC, for instance. Successful operation of GEM detectors in gas recirculation has been achieved. GEM sensitivity to common impurities (O_2, H_2O, N_2) has been measured and the necessity of using gas purification modules has been confirmed.

List of Figures

List of Tables

Bibliography

[1] C. N. Yang and R. L. Mills, *Conservation of Isotopic Spin and Isotopic Gauge Invariance*, Phy. Rev **96** (1954) 191.

[2] L. Evans and P. Bryant, *LHC Machine*, JINST **3** (2008) S08001.

[3] ATLAS Collaboration, *The ATLAS Experiment at the CERN Large Hadron Collider*, JINST **3** (2008) S08003.

[4] CMS Collaboration, *The ATLAS Experiment at the CERN LHC*, JINST **3** (2008) S08004.

[5] ALICE Collaboration, *The ALICE experiment at the CERN LHC*, JINST **3** (2008) S08002.

[6] LHCb Collaboration, *The ATLAS Experiment at the CERN LHC*, JINST **3** (2008) S08005.

[7] ATLAS Collaboration, *Observation of a new particle in the search for the Standard Model Higgs boson with the ATLAS detector at the LHC*, Phys.Lett. B **716** (2012) 1–29.

[8] CMS Collaboration, *Observation of a new boson at a mass of 125 GeV with the CMS experiment at the LHC*, Phys.Lett. B **716** (2012) 30.

[9] G. Landsberg, *LHC: Past, Present, and Future*, Proceedings of the 25^{th} Rencontres de Blois, Particle Physics and Cosmology (2013).

[10] J. Alwall, P. Schuster, and N. Toro, *Simplified Models for a First Characterization of New Physics at the LHC*, Phys. Rev. D **79** (2009) 075020.

[11] LHCb Collaboration, *First evidence for the decay Bs -> mu+ mu-*, Phys. Rev. Lett. **110** (2013) 021801.

[12] ATLAS Collaboration, *Jet size dependence of single jet suppression in lead-lead collisions at* $\sqrt{s_{NN}}$ *= 2.76 TeV with the ATLAS detector at the LHC*, Phys. Lett. B **719** (2013) 220.

[13] CMS Collaboration, *Jet size dependence of single jet suppression in lead-lead collisions at* $\sqrt{s_{NN}}$ *= 2.76 TeV with the ATLAS detector at the LHC*, Phys. Lett. B **712** (2012) 176.

[14] D Abbaneo and others, *ECFA Report on the Physics Goals and Performance Reach of the HL-LHC*, ECFA 2013.

[15] ATLAS Collaboration, *Projections for measurements of Higgs boson signal strengths and coupling parameters with the ATLAS detector at the HL-LHC*, ATL-PHYS-PUB-2013-014 (2013).

[16] CMS Collaboration, *Projected performance of an upgraded CMS detector at the LHC and HL-LHC: Contribution to the Snowmass process*, CMS-NOTE-13-002 (2013).

[17] CMS Collaboration, *Study of the Discovery Reach in Searches for Supersymmetry at CMS with 3000 fb^{-1}*, CMS-PAS-FTR-13-014 (2013).

[18] D Abbaneo and others, *ECFA High Luminosity LHC Experiments Workshop: Physics and Technology Challanges*, ECFA 2013.

[19] L. Arnaudon et al., *Linac4 Technical Design Report*, Tech. Rep. CERN-AB-2006-084 ABP/RF, CERN, Geneva, Dec, 2006.

[20] LHCb Collaboration, *Letter of Intent for the LHCb Upgrade*, CERN-LHCC-2011-0014 (2011).

[21] ALICE Collaboration, *Letter of Intent for the Upgrade of the ALICE Experiment*, CERN-LHCC-2012-012 (2012).

[22] ATLAS Collaboration, *Letter of Intent for the Phase-I Upgrade of the ATLAS Experiment*, CERN-LHCC-2011-012 (2011).

[23] ATLAS Collaboration, *Letter of Intent for the Phase-II Upgrade of the ATLAS Experiment*, CERN-LHCC-2012-022 (2012).

[24] CMS Collaboration, *Technical proposal for the upgrade of the CMS detector through 2020*, CERN-LHCC-2011-006 (2011).

[25] ATLAS Collaboration, *ATLAS Insertable B-Layer Technical Design Report*, Tech. Rep. CERN-LHCC-2010-013. ATLAS-TDR-19, CERN, Geneva, Sep, 2010.

[26] CMS Collaboration, *CMS technical design report for the Pixel Detector Upgrade*, Tech. Rep. CERN-LHCC-2012-016. CMS-TDR-011, CERN, Geneva, Sep, 2012.

[27] ALICE Collaboration, *Technical Design Report for the Upgrade of the ALICE Inner Tracking System*, Tech. Rep. CERN-LHCC-2013-024. ALICE-TDR-017, CERN, Geneva, Nov, 2013.

[28] M. Ball et al., *Ion backflow studies for the ALICE TPC upgrade with GEMs*, JINST **9** (2014) C04025.

[29] LHCb Collaboration, *LHCb VELO Upgrade Technical Design Report*, Tech. Rep. CERN-LHCC-2013-021. LHCB-TDR-013, CERN, Geneva, Nov, 2013.

[30] A. Martelli, *Evolution of the response of the CMS ECAL and possible design options for electromagnetic calorimetry at the HL-LHC*, JINST **9** (2014) C04017.

[31] ATLAS Collaboration, *New Small Wheel Technical Design Report*, Tech. Rep. CERN-LHCC-2013-006. ATLAS-TDR-020, CERN, Geneva, Jun, 2013.

[32] GEM Collaboration, *A GEM Detector System for an Upgrade of the CMS Muon Endcaps*, Tech. Rep. CMS IN 2012/002, CERN, Geneva, 2012.

[33] ATLAS Collaboration, *ATLAS pixel detector electronics and sensors*, JINST **3** (2008) P07007. http://iopscience.iop.org/1748-0221/3/07/P07007/.

[34] J. Dopke and S. Welch, *The ATLAS Pixel nSQP Readout Chain*, ATL-INDET-PROC-2012-018 (2012).

[35] M. Cerv, *The ATLAS Diamond Beam Monitor*, JINST **9** (2014) P05006.

[36] ATLAS Collaboration, "Approved Pixel Plots." http://twiki.cern.ch/twiki/bin/view/AtlasPublic/ApprovedPlotsPixel.

[37] A. Salzburger, S. Todorova, and M. Wolter, *The ATLAS Tracking Geometry Description*, Internal Report ATL-SOFT-PUB-2007-004 (2007).

[38] A. Salzburger, S. Todorova, and M. Wolter, *Expected Performance of the ATLAS Experiment: Detector, Trigger and Physics*, CERN-OPEN-2008-020 (2009).

[39] ATLAS IBL Collaboration, *Prototype ATLAS IBL Modules using the FE-I4A Front-End Readout Chip*, JINST **7** (2012) P11010, arXiv:1209.1906 [physics.ins-det].

[40] M. Povoli et al., *Slim edges in double-sided silicon 3D detectors*, JINST **7** (2012) C01015.

[41] D. Arutinov et al., *Digital architecture and interface of the new ATLAS Pixel Front-End IC for upgraded LHC luminosity*, Nuclear Science, IEEE Transactions **56** (2009) 388–393.

[42] V. Zivkovic et al., *The FE-I4 pixel readout system-on-chip resubmission for the insertable B-Layer project*, JINST **2** (2012) C02050.

[43] FE-I4 Collaboration, *FE-I4B Integrated Circuit Guide*. v2.3.

[44] L. Gonella, F. Hugging, and N. Wermes, *Towards minimum material trackers for high energy physics experiments at upgraded luminosities*, Nucl. Instrum Meth. A **650** (2011) 202–207.

[45] ATLAS Collaboration, *ATLAS Pixel IBL: Stave Quality Assurance*, ATL-INDET-PUB-2014-006 (2014).

[46] B. Verlaat et al., *TRACI, a multipurpose CO_2 cooling system for R&D*, 10^{th} IIR Gustav Lorentzen Conference on Natural Refrigerants (2012).

[47] The ROOT team, "The ROOT Users Guide." http://root.cern.ch/drupal.

[48] A. Micelli, *3D sensors for the Insertable B-Layer of the ATLAS experiment at the CERN LHC*. PhD thesis, Udine U., Udine, 2012.

[49] M. Backhaus, *High bandwidth pixel detector modules for the ATLAS Insertable B-Layer*. PhD thesis, Bonn U., Bonn, Feb, 2014.

[50] G. Aad, *Commissioning of the ATLAS pixel detector and search of the Higgs boson in the ttH, H -> bb channel with the ATLAS experiment at the LHC*. PhD thesis, CPPM-T-2009-003, Marseile, 2009.

[51] M. Havranek, F. Hugging, H. Kruger, and N. Wermes, *Measurement of pixel sensor capacitances with sub-femtofarad precision*, Nucl. Instrum Meth. A **714** (2013) 83–89.

[52] G. Bolla et al., *Wire-bond failures induced by resonant vibrations in the CDF silicon detector*, Nucl. Instrum Meth. A **518** (2004) 277.

[53] M Garcia Sciveres, "Power supply transients in FE-I4." Private communication, Jan 2014.

[54] D Alvarez Feito, "IBL wire bonding: a method to prevent fatigue failure?." Private communication, Apr 2014.

[55] T. Barber et al., *Resonant bond wire vibrations in the ATLAS semiconductor tracker*, Nucl. Instrum Meth. A **538** (2005) 442.

[56] ATLAS Collaboration, *Wirebond Encapsulation Methods for ATLAS Pixel Modules*, ATL-INDET-2004-007 (2004).

[57] R. Guida, M. Capeans, F. Hahn, S. Haider, and B. Mandelli, *The gas systems for the LHC experiments*, Nuclear Science, IEEE Transactions (2013).

[58] R. Guida, M. Capeans, F. Hahn, S. Haider, B. Mandelli, and E. Focardi, *A common analysis station for the gas systems of the Compact Muon experiment at the CERN Large Hadron Collider*, Nuclear Science, IEEE Transactions (2011).

[59] M. Capeans, *Study of the ageing of gaseous detector and solutions for the use of MSGCs in high rate experiments*. PhD thesis, U. Santiago de Compostela, Santiago de Compostela, 1995.

[60] B. Mandelli, M. Capeans, R. Guida, and P. Vitulo, *Systematic study of RPC performances in polluted or varying gas mixture compositions: An online monitor system for the RPC gas mixture at LHC*, Nuclear Science, IEEE Transactions (2012).

[61] R. Guida, M. Capeans, F. Hahn, S. Haider, and B. Mandelli, *Development of a common gas analysis approach for the gas systems of all the experiments at the CERN Large Hadron Collider*, Nuclear Science, IEEE Transactions (2012).

[62] A. Cardini, G. Bencivenni, and P. D. Simone, *The operational experience of the triple-GEM detectors of the LHCb muon system: Summary of 2 years of data taking*, Nuclear Science, IEEE Transactions (2012).

[63] M. Capeans, R. Guida, F. Hahn, S. Haider, and B. Mandelli, *Long term validation of the optimal filters configuration for the Resistive Plate Chambers gas system at the Large Hadron Collider experiments*, Nuclear Science, IEEE Transactions (2011).

[64] M. Capeans, R. Guida, F. Hahn, S. Haider, and B. Mandelli, *RPC performances and gas quality in a closed loop gas system for the new purifiers configuration at LHC experiments*, JINST **8** (2013) T08003.

[65] V. Arena et al., *Performance of resistive plates counters operated with mixtures containing different freons*, Nucl. Instrum Meth. A **400** (1997) 156.

[66] M. Capeans, R. Guida, F. Hahn, S. Haider, and S. Rouwette, *Development of a CF_4 recuperation plant for the Cathode Strip Chambers detector at the CERN Compact Muon Solenoid experiment*, Nuclear Science, IEEE Transactions (2010).

[67] M. Capeans, R. Guida, F. Hahn, and S. Haider, *Commissioning of the CF_4 recuperation plant for the Cathode Strip Chambers detector at the CERN Compact Muon Solenoid experiment*, Nuclear Science, IEEE Transactions (2011).

[68] D. S. Levin et al., *A gas monitor for the ATLAS Muon Spectrometer precision chambers*, Nuclear Science, IEEE Transactions (2007).

[69] Z. Hajduk et al., *Proposal for gas gain monitoring in TRT gas system*, ATLAS TRT Technical note EP-ATE-ZH (1998).

[70] W. R. Leo, *Techniques for Nuclear and Particle Physics Experiments*. Springer-Verlag, 2 ed., 1993.

[71] G. F. Knoll, *Radiation Detection and Measurement*. John Wiley and Sons, Inc., 3 ed., 1999.

[72] W. Blum, W. Riegler, and L. Rolandi, *Particle Detection with Drift Chambers*. Springer-Verlag, 3 ed., 2008.

[73] A. Mann and F. Linder J. Phys., B **25** (1992) 533.

[74] C. Brundle et al. J. Chem. Phys. **53** (1970) 400.

[75] R. A. Bonham Jpn. J. Appl. Phys. **33** (1994) 400.

[76] L. Boesten et al. J. Phys., B **25** (1992) 400.

[77] A. Schreiner, *Aging Studies of Drift Chambers of the HERA-B Outer Tracker Using CF_4-based Gases*. PhD thesis, Humboldt University, Berlin, 2001.

[78] C. Duncan and I. Walker, *Collision cross-sections for electrons in ethylene and acetylene*, J. Chem. Soc. Faraday Trans., II **68** (1972) 1800.

[79] C. Duncan and I. Walker, *Collision cross-sections for low-energy electrons in some simple hydrocarbons*, J. Chem. Soc. Faraday Trans., II **70** (1974) 577.

[80] L. G. Cristophorou et al. Nucl. Instr .Meth. **163** (1979) 141.

[81] R. Bouclier, M. Capeans, C. Garabatos, F. Sauli, and K. Silander, *Effects of outgassing from some materials on gas chamber aging*, Nucl. Instr .Meth. A **350** (1994) 464.

[82] A. T. P. Fontenla, "SEM-EDS analysis of irradiated wire." Private communication, 2014.

[83] S. Bachmann et al., *Ageing Phenomena in the LHCb Outer Tracker*, LHCb-CONF-2009-019 (2009).

[84] L. Malter, *Thin film field emission*, Phys. Rev. **50** (1936) 48.

[85] M. Kushner, *A Kinetic Study of the Plasma Etching Process: A Model for the Etching of Si and SiO2 in C_nF_m/H_2 and C_nF_m/O_2 Plasmas*, J. Appl. Phys. **53** (1982) 2923.

[86] D. M. Manos et al., *Plasma Etching*. Academic Press Boston, 1989.

[87] C. J. Mogab J. Appl. Phys. **49** (1978) 3796.

[88] F. Sauli, *GEM: A new concept for electron amplification in gas detectors*, Nucl. Instrum. Methods A **386** (1997) 531.

[89] M. Alfonsi et al., *Studies of Etching Effects on Triple-GEM Detectors Operated With CF_4-Based Gas Mixtures*, Nuclear Science, IEEE Transactions **52** (2005) 2872.

[90] CMS Collaboration, *The CMS muon project : Technical Design Report*, Tech. Rep. CERN-LHCC-97-032, CERN, Geneva, 1997.

[91] CMS Collaboration, *The performance of the CMS muon detector in proton-proton collisions at sqrt(s) = 7 TeV at the LHC*, JINST **8** (2013) 11002.